Title
Engineering Magnetic Anisotropy in Nanostructured 3d and 4f Ferromagnets

Author
Hsu, Chin-Jui

Publication Date
2012

Peer reviewed|Thesis/dissertation

UNIVERSITY OF CALIFORNIA

Los Angeles

Engineering Magnetic Anisotropy in Nanostructured 3d and 4f Ferromagnets

A dissertation submitted in partial satisfaction of the

requirements for the degree Doctor of Philosophy

in Mechanical Engineering

by

Chin-Jui Hsu

2012

ABSTRACT OF THE DISSERTATION

Engineering Magnetic Anisotropy in Nanostructured 3d and 4f Ferromagnets

by

Chin-Jui Hsu

Doctor of Philosophy in Mechanical Engineering

University of California, Los Angeles, 2012

Professor Gregory P. Carman, Chair

Due to the increased demand for clean energy in recent years, there is a need for the scientific community to develop technology to harvest thermal energy which is ubiquitous but mostly wasted in our environment. However, there is still no efficient approach to harvest thermal energy to date. In this study, the theory of thermomagnetic energy harvesting is reviewed and unique applications of multiferroics (ferromagnetic plus ferroelectric) are introduced. Based on an efficiency analysis using experimentally measured magneto-thermal properties of 3d transitional and 4f rare earth ferromagnetic elements, the idea of using single domain ferromagnetic elements to obtain higher thermomagnetic conversion efficiencies is proposed. In order to fabricate a ferromagnetic single domain, the magnetic anisotropy of gadolinium (Gd) and nickel (Ni) is engineered at the nanoscale. Both thin films and nanostructures are fabricated and characterized with a focus on the change of magnetic anisotropy governed by shape, crystal structure, and strain. The fabrication processes include sputtering, e-beam lithography (writing

and evaporation), and focused ion beam milling. Characterization techniques involving atomic/magnetic force microscopy, energy dispersive X-ray spectroscopy, magneto-optical Kerr effect magnetometry, superconducting quantum interference device magnetometry, scanning/transmission electron microscopy, and X-ray diffraction will also be discussed. Experimental results show that the magnetic domain structure of nanostructured Ni can be stably controlled with geometric constraints or by strain induced via electric field. The magnetic properties of nanostructured Gd, on the other hand, is sensitive to crystal structure. These results provide critical information toward the use of ferromagnetic nanostructures in thermomagnetic energy harvesting and multiferroic applications.

The dissertation of Chin-Jui Hsu is approved.

Pei-Yu Chiou

Suneel Kodambaka

Christopher S. Lynch

Gregory P. Carman, Committee Chair

University of California, Los Angeles

2012

To my parents and Ting-Hsuan

Table of Contents

List of Figures

List of Tables

ACKNOWLEDGEMENTS

It has been four years since the first day I started my life in the US with my wife. Time flies and now I have become a father of two. I truly feel so blessed.

A lot of things to me are like just happened yesterday. I remember my very first meeting with my adviser Professor Greg. Carman and project group. It was such a great opportunity for me, as an international graduate student who just begun his PhD career, to meet with people from different places around the world. Immediately, I knew that this is the place where I want to be. So first of all, I would like to express my endless thank to Prof. Carman. Your mentorship and the environment you created for your students are invaluable to me. I must also thank the former and present AML members. You all made my learning experience at UCLA so enjoyable.

I sincerely appreciate Dr. Sergey Prikhodko, Dr. Adam Stieg, and Dr. Chiu Y. Wang. You have helped me to overcome many obstacles in my research. Without your insightful expertise, my work could not have been completed.

Thank you to my funding agency, Air Force Office of Scientific Research, and project manager, Dr. Byung-Lip "Les" Lee.

To my committee members, Prof. Chiou, Prof. Kodambaka, and Prof. Lynch, many thanks for your feedback and participation in this process.

To my LA and hometown friends, I made it. Cheers!

Lastly, my immense gratitude and love goes to my family. There is no way I can finish my degree without full support from my parents, parents in law, and my wife. Especially my beloved, Ting-Hsuan, you have always been by my side since I was a bold college student. I am no Jerry Maguire, but I definitely want to say "You complete me." My lovely daughters, Jalynn and Jamie, all you need to know is that dad will always love you.

VITA

2000-2001	Research Apprentice Micro Analysis and Failure Diagnosis Lab. National Cheng Kung University, Tainan, Taiwan
2001	B.S., Mechanical Engineering National Cheng Kung University, Tainan, Taiwan
2001-2003	Research Assistant Precision Transmission Lab. National Tsing Hua University, Hsinchu, Taiwan
2003	M.S., Power Mechanical Engineering National Tsing Hua University, Hsinchu, Taiwan
2004-2008	Assistant Researcher/Reserved Officer Chun Shang Institute of Science and Technology, Taoyuan, Taiwan
2008	MAE Departmental Fellowship UCLA, Los Angeles, California
2009-2012	Graduate Student Researcher Active Materials Lab. UCLA, Los Angeles, California
2012	Research Highlights ASME & AIAA Adaptive Structures & Material Systems Newsletter UCLA Engineering E-bulletin

Selected Publication

Journal:

Chin-Jui Hsu, Sergey V. Prikhodko, Chiu-Yen Wang, Lih-Juann Chen, and Gregory P. Carman, "*Magnetic Anisotropy in Nanostructured Gadolinium*," Virtual Journal of Nanoscale Science and Technology, 25(12), 2012. **(Selected article from JAP)**

Chin-Jui Hsu, Sergey V. Prikhodko, Chiu-Yen Wang, Lih-Juann Chen, and Gregory P. Carman, "*Magnetic Anisotropy in Nanostructured Gadolinium*," Journal of Applied Physics, 111, 053916, 2012.

Chin-Jui Hsu, Joshua L. Hockel, and Gregory P. Carman, "*Magnetoelectric manipulation of domain wall configuration in thin film Ni/*$[Pb(Mg_{1/3}Nb_{2/3})O_3]_{0.68}$*-*$[PbTiO_3]_{0.32}$ *(001) heterostructure*," Applied Physics Letters, 100, 092902, 2012.

Chin-Jui Hsu, Samuel M. Sandoval, Kyle P. Wetzlar, Gregory P. Carman, "*Thermomagnetic Conversion Efficiencies for Ferromagnetic Materials*," Journal of Applied Physics, 110, 123923, 2011.

Alexandre Bur, Tao Wu, Joshua L. Hockel, Chin-Jui Hsu, Hyungsuk K. D. Kim, Tien-Kan Chung, Kin Wong, Kang L. Wang, and Gregory P. Carman, "*Strain-induced magnetization change in patterned ferromagnetic nickel nanostructures*," Journal of Applied Physics, 109, 123903, 2011.

Tao Wu, Alexandre Bur, Kin Wong, Joshua L. Hockel, Chin-Jui Hsu, Hyungsuk K. D. Kim, Kang L. Wang, and Gregory P. Carman, "*Electric-poling-induced magnetic anisotropy and electric-field-induced magnetization reorientation in magnetoelectric Ni/(011) $[Pb(Mg_{1/3}Nb_{2/3})O_3]_{(1-x)}$-$[PbTiO_3]_x$ heterostructure*," Journal of Applied Physics, 109, 07D732, 2011.

Conference:

Chin-Jui Hsu, Joshua L. Hockel, and Gregory P. Carman, "*Electric-field-induced Domain Wall Transitions in Thin Film Ni/PMN-PT (001) Heterostructure*," IEEE International Magnetics (INTERMAG) Conference, Vancouver, Canada, 2012.

Chin-Jui Hsu, Samuel M. Sandoval, Kyle P. Wetzlar, Gregory P. Carman, "*Energy conversion efficiency analysis using thermomagnetic properties of ferromagnetic materials*," 56th Annual Conference on Magnetism and Magnetic Materials (MMM), Scottdale, Arizona, USA, 2011.

Kyle P. Wetzlar, Chin-Jui Hsu, and Gregory P. Carman, "*Order-to-order Magnetic Phase Transitions for Thermal Energy Harvesting*," 56th Annual Conference on Magnetism and Magnetic Materials (MMM), Scottdale, Arizona, USA, 2011.

Joshua L. Hockel, Tao Wu, Alexandre Bur, Kyle P. Wetzlar, Chin-Jui Hsu, and Gregory P. Carman, "*Planar Magnetization Control in Patterned Single Domain Nanostructures*," 56th Annual Conference on Magnetism and Magnetic Materials (MMM), Scottdale, Arizona, USA, 2011.

Gregory P. Carman and Chin-Jui "Ray" Hsu, "*Thermomagnetic Energy Harvesting Using Ferromagnetic Materials*," Materials Research Society (MRS) Spring Meeting, San Francisco, California, USA, 2011. **(Invited talk)**

Samuel M. Sandoval, Chin-Jui Hsu, and Gregory P. Carman, "*An Efficiency Analysis of a Novel Thermal Energy Harvesting Device*," SPIE Smart Structures/NDE 2010, San Diego, California, USA, 2010.

CHAPTER 1

INTRODUCTION

Anisotropy is a term in physics to describe a directionally dependent material property. For magnetic materials, when magnetic anisotropy exists, the magnetization has a preferred orientation along a specific axis. Magnetic anisotropy can arise from various sources such as sample geometry, crystal structure, or stress. These anisotropy terms are also referred to as shape anisotropy, magnetocrystalline anisotropy, and magnetostriction respectively. The presence of magnetic anisotropy produces a preferred magnetization direction which is called the easy direction since it is "easier" to magnetize the material along this direction. The energy associated with magnetization and its relation to the easy direction strongly dictates the magnetic properties of the material.

In ferromagnetic materials, especially at the nanoscale, magnetic anisotropy has a significant impact on the magnetic domain formation. Fundamentally speaking, a magnetic domain is a region which has a uniform magnetization. This region consists of a collection of magnetic dipoles (i.e. spins) which cooperate with each other and point in the same direction. Since the magnetization of different domains can point in different directions, the direction of each magnetic domain is dictated by minimizing the energy associated with the magnetization process of ferromagnetic materials. Due to the fact that the magnetization of each magnetic domain is directional, the magnetic anisotropy of a material naturally influences the magnetic domain formation as well as its magnetic properties. This fact implies that if one can tune the magnetic anisotropy of a sample, the magnetic property of the sample can also be modulated.

One typical example of changing magnetic anisotropy to modify magnetic property is the use of magnetic recording technology in modern hard drives [1]. In magnetic recording, the bit information is stored in a magnetic domain represented by a magnetization direction. When the magnetization direction is normal to the disk surface, it is called “perpendicular” magnetic recording. Prior to perpendicular magnetic recording, researchers relied on in-plane domain magnetizations to store data in the disk termed “longitudinal” magnetic recording. When these two recording technologies were compared (see Fig. 1-1), the perpendicular magnetic recording is deemed superior because the domain magnetizations do not directly oppose each other; therefore, the bit information can be packed more closely with sharper transition signals and thus enable higher information storage density (bits stored per area). The perpendicular type of magnetic domain structure is formed by controlling the size and shape of the grain grown in the magnetic thin film materials (i.e. engineering the magnetic anisotropy), so that out-of-plane directions become the easy direction of magnetization for each domain.

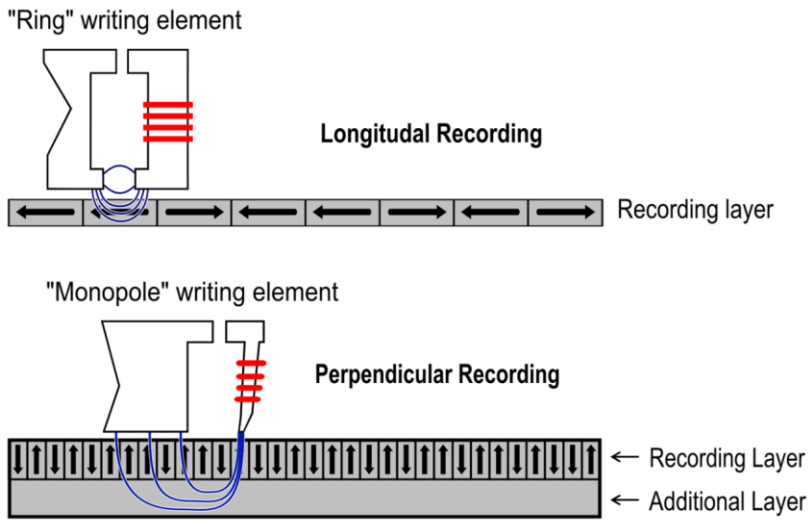

Figure 1-1: Comparison of longitudinal and perpendicular magnetic recording. The bold black arrows represent the magnetization direction of each domain as well as the bit information stored in the material. [Diagrams modified from Wikipedia/Perpendicular Recording]

In this dissertation, the idea of engineering magnetic anisotropy to control the magnetic property is applied to nanostructured ferromagnetic materials (i.e. thin films and nanostructures). The nanostructured ferromagnetic materials are used in applications including multiferroics and thermomagnetics. Multiferroic applications focus on the coupling effect between ferroelectric and ferromagnetic materials while the thermomagnetics applications focus on ferromagnetic properties change as a function of temperature and applied magnetic field. Based on the characteristics of materials and their applications, the main body of this dissertation is divided into three chapters represented by: 1. Nanostructured Nickel, 2. Nanostructured Gadolinium, and 3. Thermomagnetic Energy Harvesting.

This dissertation focuses on nickel (Ni) and gadolinium (Gd) due to their unique magnetic properties (e.g. Gd has a Curie point at room temperature) as well as some of the more well understood behavior at the nanoscale (e.g. Ni has single and multi-domain state). In Chapter 2, a thin film Ni/ferroelectrics heterostructure is introduced. By using a strain-mediated converse magnetoelectric (ME) effect, the magnetic anisotropy in the nanoscale Ni thin film is electrically controlled, and a significant out-of-plane to in-plane magnetization change is experimentally observed. This Ni thin film experiment is followed by a review of single domain theory. The characterization of patterned Ni nanostructures having a single domain is also presented. This chapter reveals that the manipulation of Ni domain structure in the nanoscale is possible.

In Chapter 3, the magnetic anisotropy of Gd in the nanoscale is discussed. Both Gd thin film and nanostructure are fabricated in an attempt to produce single domain. Since an experimental observation of Gd single domain is absent in the literature, extensive characterizations of both Gd thin film and nanostructure are performed to identify the problem. Results suggest that the spin reorientation (a phenomenon of easy axis change as a function of

temperature) can be observed when the Gd thin film is textured; however, the formation of single domain in Gd nanostructures is hindered due to oxidation and crystal structure transformation in the nanoscale.

In Chapter 4, the importance of single domain ferromagnetic nanostructure in the context of thermomagnetic energy harvesting is described. When a ferromagnetic material is thermally cycled across its Curie point, the efficiency of converting thermal energy to magnetic energy is particular important to the energy harvesting application. In this chapter, a thorough study on the thermomagnetic conversion efficiency of all ferromagnetic elements is presented. Based on the calculations using experimental data, a single domain ferromagnetic approach to increase thermomagnetic conversion efficiency is proposed. Analytical results for Gd single domains suggest efficiencies on the order of 30% are possible, representing a threefold increase from multi-domain Gd.

Chapter 4 along with the preceding two chapters provides fundamental information on using magnetic anisotropy engineering for practical applications. A brief summary as well as a description of future research is provided in Chapter 5.

CHAPTER 2

NANOSTRUCTURED NICKEL

Chapter 2 discusses the magnetic domain structures engineered in both Ni thin film and nanostructures. In the nanoscale Ni thin film, magnetization and the corresponding magnetic domain structure is extremely sensitive to film thickness and its corresponding magnetic anisotropy energy. By using a strain-mediated magnetoelectric (ME) effect (i.e. multiferroics), several studies report substantial *in-plane* magnetization changes in thin film Ni/ferroelectrics heterostructures. While the theoretical prediction shows that *out-of-plane* magnetization rotation is possible in these multiferroics systems, the changes shown in the literature are fairly trivial. In this chapter, experimental results for significant out-of-plane magnetization change with the application of a electric field in a thin film Ni/$[Pb(Mn_{1/3}Nb_{2/3})O_3]_{0.68}$-$[PbTiO_3]_{0.32}$ (PMN-PT) (001) heterostructure is presented and demonstrated. Both irreversible and reversible out-of-plane magnetization rotations are observed using a magnetic force microscope (MFM). Magnetic domain wall pinning due to ferroelectric domain texturing is also observed. The magnetization reorientation as well as the change in magnetic domain structure is dependent on Ni thin film thickness and is attributed to a transition of magnetic domain wall between Néel and Bloch wall. These findings provide useful information regarding the electrical control of magnetization using multiferroics.

In addition to thin film, the modeling, fabrication, and testing of single domain Ni nanostructures are presented in this chapter. Modeling shows a theoretical prediction on the geometry of Ni single domain for a fixed thickness. Fabrication focuses on E-beam lithography

based processes, and Ni nanostructures with different geometries were fabricated based on the modeling results. Testing was performed using a magnetic force microscope with a focus on the comparison between the modeling and actual domain configuration in the fabricated nanostructures. Experimental results suggest that the shape anisotropy change could have significant impact on the formation of single domain in Ni nanostructure. Analytical results based on a simplified model of energy balance showed a good match with the experimental results.

2.1 Thin film

The electric-field-controlled magnetization changes from out-of-plane to in-plane in a 60-nm-thick thin film Ni/PMN-PT (001) heterostructure were experimentally observed. MFM results show significant changes in the stripe magnetic domain structures (i.e. elimination of stripe domains) with the application of electric fields. Depending on the ferroelectric PMN-PT poling state, the stripe domain elimination can be either reversible or irreversible. During the poling process, prominent domain wall pinning was also observed at the ferroelectric domain boundaries. The observed domain structure changes are attributed to transition from an energy state favoring Bloch walls to one in which Néel walls become more prevalent in the Ni thin film. Furthermore, for a relatively thicker film (100 nm), a similar electric-field-induced domain structure change was not observed. A discussion on the relationship between electric-field-induced strain, magnetostriction, and domain wall transition in Ni thin film is provided in this section.

2.1.1 Background

During the past decade, the magnetic domain structure in nanoscale nickel thin film (i.e. 2 to 200 nm) has been extensively studied [2-5]. Researchers have shown that the magnetic domain structure (e.g. flux closure [3] or maze/stripe domain pattern [5]) is extremely sensitive to film thickness (t) and magnetic anisotropy energy, with dramatic changes occurring in the $t < 100$ nm region [3-4]. For example (see Fig. 2-1), stripe domains with flux closure configuration (i.e. the coexistence of the Block and Néel walls) [4] are reported in relatively thicker Ni films ($t > 25$ nm). As the thickness is decreased ($10 < t < 25$ nm), the flux closure configuration is less favorable and the stripe domains break up into bubble domain [3] patterns. As for films with a thickness of $2 < t < 10$ nm, only Block walls (i.e. no flux closure) are reported and the domain magnetization direction is exclusively out-of-plane [3-4]. Although many of these studies are for epitaxial Ni thin films, similar results are found in polycrystalline (i.e. non-textured) Ni thin film [6].

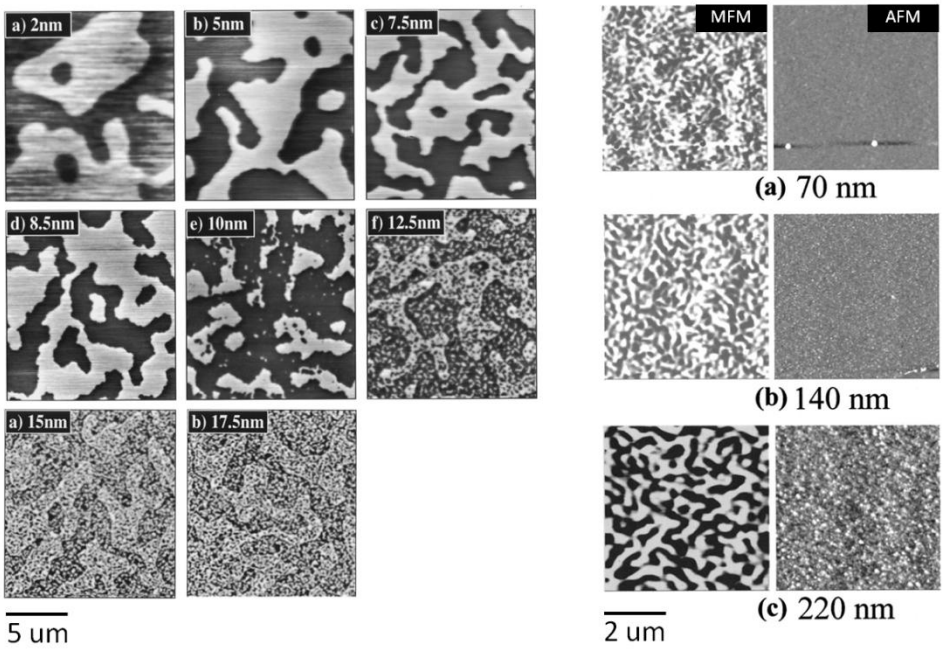

Figure 2-1: MFM magnetic domain images of epitaxial Ni thin films [3-4]. The domain configuration changes as the film thickness increases.

One approach to control the magnetic domain structure of thin films is with magnetoelectric (ME) heterostructures (e.g. multiferroics) [7-10]. Several studies report electric field induced strain produces in-plane magnetization changes in Ni/ferroelectrics ME systems, e.g. 35-nm-thick Ni on $LiNbO_3$ [11], 35-nm-thick Ni on PMN-PT [12], 100-nm-thick Ni on $BaTiO_3$ [13], and 100-nm-thick Ni on $Pb[Zr_{0.52}Ti_{0.48}]O_3$ (PZT) hybrid structure [14]. Furthermore, studies have been conducted on many other nanoscale ferromagnetic thin films (e.g. CoFe [15], $CoFe_2O_4$ [16], Fe [17], Fe_3O_4 [18], FeGaB [19], FePt [20]. and $La_{0.7}Sr_{0.3}MnO_3$ [21]) deposited on different ferroelectric substrates (e.g. $BaTiO_3$ [15, 17], $[Pb(Zn_{1/3}Nb_{2/3})O_3]_{0.94}$-$[PbTiO_3]_{0.06}$ (PZN-PT) [16, 18-20], and PMN-PT [18, 21]). While a variety of studies are present, Ni thin film is probably one of the more well understood systems in terms of thickness dependence on magnetic domain structure. Furthermore, the majority of these thin film ME studies (including Ni) focus on in-plane magnetization changes rather than the out-of-plane magnetization changes which is of particular importance to modern magnetic recording technologies [1, 10]. The main reason studies focus on in-plane magnetization changes is the relatively smaller energy barrier to reorient in-plane magnetization as compared to reorienting out-of-plane magnetization as described in theoretical analyses [22-23]. While the theoretical prediction shows that out-of-plane magnetization rotation is possible in Ni ME heterostructure, the experimental changes observed are fairly trivial [6].

2.1.2 Fabrication

The test samples consist of a 60-nm-thick Ni thin film deposited onto a 0.5-mm-thick (001) cut single crystal PMN-PT. Prior to Ni deposition, a 10 nm Ti adhesive layer and a 50 nm Pt electrode layer were deposited on the both sides of the PMN-PT. Two sets of samples were fabricated: one has Ni thin film deposited before the PMN-PT was poled (i.e. un-poled PMN-PT), and the other has Ni thin film deposited after the PMN-PT was poled along the <001> direction with an electric field of 0.8 MV/m (i.e. pre-poled PMN-PT). For the later sample, residual strains caused by the poling process are absent. Schematic diagrams of the fabricated Ni/PMN-PT sample structure and the strain state of Ni thin film during the poling process are shown in Fig. 2-2. A third sample consisting of 100-nm-thick Ni and un-poled PMN-PT (001) was also fabricated. All test results presented in this dissertation are from the 60-nm-thick Ni/PMN-PT (001) sample unless otherwise stated.

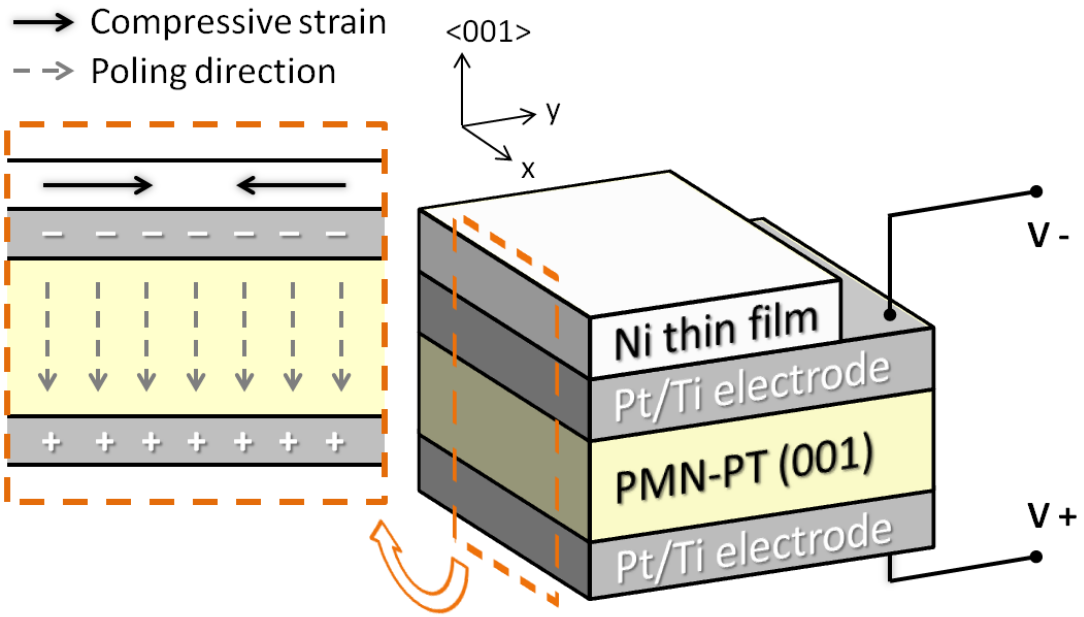

Figure 2-2: Ni/PMN-PT heterostructure. When the PMN-PT is poled along the <001> direction, the piezoresponse of PMN-PT induces compressive strains in the x-y plane of the Ni thin film.

2.1.3 Experiment

Three experiments were performed to characterize 60-nm-thick Ni/PMN-PT (001) heterostructure, and both un-poled and pre-poled samples were characterized in the same manner:

1. Piezoresponse (strain versus electric field) measurement of PMN-PT (001): the strain versus electric field (ε-E) curves were measured by mounting a biaxial strain gauge on the sample surface with a triangular electric field waveform applied at 0.01 Hz. The strain gauges were zeroed prior to recording data.
2. Domain structure observation using atomic and magnetic force microscopy: the domain pattern changes in the Ni/PMN-PT heterostructure were captured at the five electric field points (i.e. $0 \leq E \leq 0.8$ MV/m) using an atomic/magnetic force microscope (A/MFM). The AFM model is Bruker Dimension 5000. A low moment MFM probe (Nanosensors PPP-LM-MFMR) magnetized along the tip axis was used for all imaging. An illustration of the A/MFM test setup is shown in Fig. 2-3.
3. Magnetization change measurement using magneto-optical Kerr effect (MOKE): both longitudinal and polar geometries were used. The longitudinal geometry detects the magnetization change in the in-plane directions, whereas the polar geometry measures the out-of-plane magnetization change.

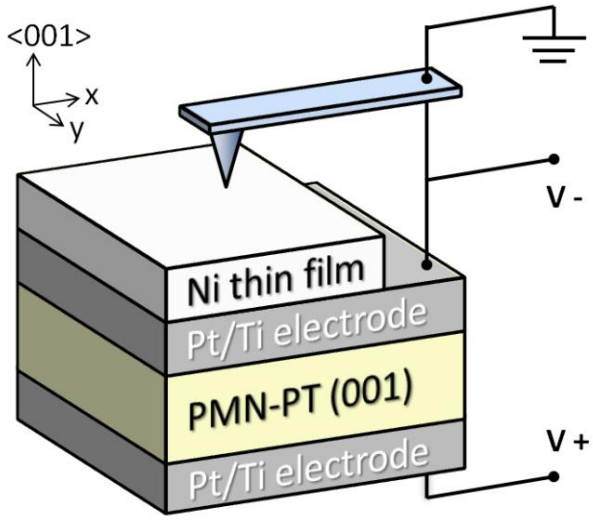

Figure 2-3: Atomic/Magnetic force microscope and Ni/PMN-PT test setup. MFM probe senses local magnetic fields mainly along the <001> direction.

2.1.3.1 Ni thin film and un-poled PMN-PT

2.1.3.1.1 Piezoresponse Curves

Fig. 2-4 shows the in-plane (i.e. both x and y directions) ε-E curves of the 60-nm-thick Ni/PMN-PT (001) un-poled sample during the poling process. As shown in Fig. 2-4, in-plane compressive strains as large as 1600 με are produced in the poling nonlinear region (i.e. points 1 to 3) when an electric field of 0.8 MV/m is applied. Upon removal of the poling electric field, remnant strains are present (see point 4). Note that the remnant strain is different for the x and y directions and this difference (Δε) is sample dependent. This strain difference is attributed to the initial ferroelectric domain distribution in the un-poled sample, and therefore, the overall resultant strain in Ni thin film is anisotropic.

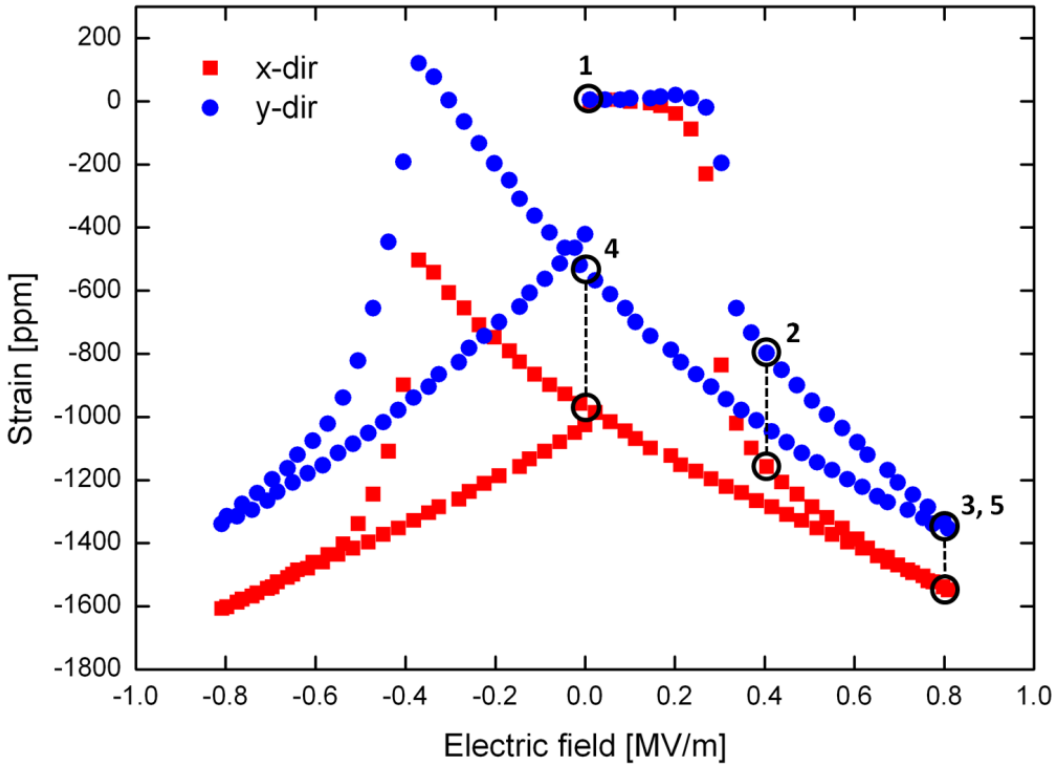

Figure 2-4: In-plane piezoelectric response of 60-nm-thick Ni/PMN-PT (001) un-poled sample: (1) Un-poled (0 MV/m), (2) 0.4 MV/m, (3) 0.8 MV/m, (4) 0 MV/m, and (5) 0.8 MV/m.

2.1.3.1.2 Atomic Force and Magnetic Force Microscopy

Fig. 2-5 shows the atomic force microscope (AFM) topographic height images (Fig. 2-5.1a to Fig. 2-5.5a) and corresponding MFM domain images (Fig. 2-5.1b to Fig. 2-5.5b) of the 60 nm Ni thin film at the five different electric field points shown in Fig. 2-4. Fig. 2-5.1c to Fig. 2-5.5c show magnified MFM images of the boxed regions shown in Fig. 2-5.1b to Fig. 2-5.5b. Based on the piezoresponse force microscope experiments previously reported for PMN-PT [24], it is believed that the AFM images in Fig. 2-5.1a to Fig. 2-5.5a show the presence of ferroelectric domains as evidenced by the alternating light and dark regions. The height difference between the neighboring ferroelectric domains (i.e. light and dark areas) is about ± 2 nm. Note that when comparing the five AFM images captured at different electric fields, one sees that the surface

texture does not change during application of electric fields (i.e. ferroelectric domains are immobile in the scan area); however, significant ferroelectric domain changes were readily observable outside the scan area with the naked eye.

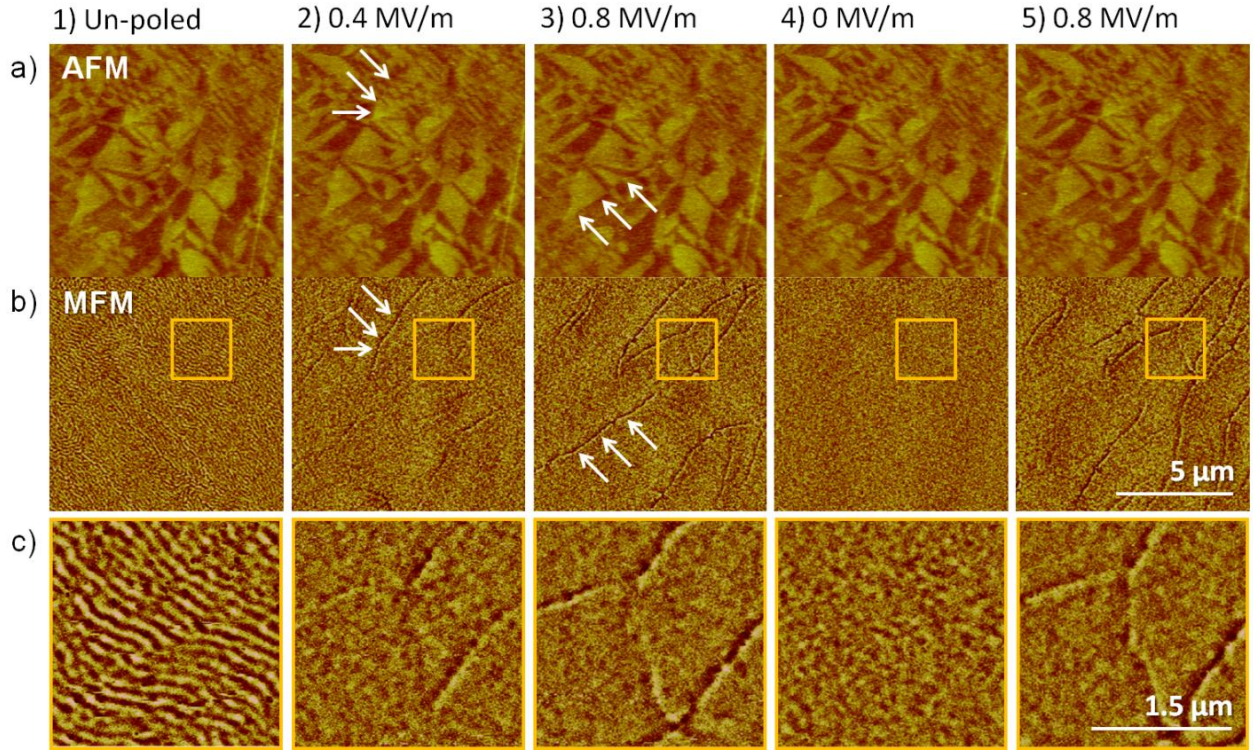

Figure 2-5: AFM (a) and MFM (b and c) images of 60-nm-thick Ni thin film on PMN-PT (001) un-poled substrate captured at five different times corresponding to points 1 to 5 in Fig. 2-4 respectively. MFM images in (c) represent the box areas shown in (b). Arrows in (a) indicate ferroelectric domain boundaries and arrows in (b) indicate domain wall pinning locations.

When reviewing the five MFM images in Fig. 2-5.1b to Fig. 2-5.5b (also see the magnified views in Fig. 2-5.1c to Fig. 2-5.5c), notable changes are observed in the magnetic domain structure. Fig. 2-5.1b and Fig. 2-5.1c in the un-poled state show a typical stripe domain pattern in the Ni thin film. As the electric field increases to 0.4 MV/m in Fig. 2-5.2b and Fig. 2-5.2c, the stripe domain pattern is eliminated and some virtual "crack-like" images begin to

emerge as indicated by the arrows. Since surface roughness is known to cause domain wall pinning [25], the texturing present in the AFM images (i.e. the immobile ferroelectric domain boundaries) is believed to pin the magnetic domain walls and produce crack-like structures in the MFM images. As the electric field increases to 0.8 MV/m (see Fig. 2-5.3b and Fig. 2-5.3c), the number of domain walls pinned (i.e. the crack-like structure) increases. These domain wall pinning locations are correlated to the ferroelectric domain boundaries as indicated by the arrows in the AFM images in Fig. 2-5.2a and Fig. 2-5.3a. Upon removal of the electric field (i.e. back to point 4 in Fig. 2-4), Fig. 2-5.4 b and Fig. 2-5.4c show that the domain wall pinning sites are eliminated (i.e. absence of crack-like structure) and the stripe domain pattern does not recover. The "mottled" domain image present in Fig. 2-5.4c is caused by the remnant strains present in the Ni thin film (see point 4 in Fig. 2-4). As an electric field of 0.8 MV/m is reapplied (see Fig. 2-5.5b and Fig. 2-5.5c), the crack-like structures once again appear. Although some of the domain wall pinning locations in Fig. 2-5.5b are different from those shown in Fig. 2-5.3b, these crack-like structures are geometrically very similar. In general, the larger area AFM and MFM images in Fig. 2-5 (a and b) provide information about the domain wall pinning while the magnified views of MFM image in Fig. 2-5c reveal more detail about the domain configuration change.

2.1.3.1.3 Magneto-optical Kerr Effect Magnetometry

Fig. 2-6 shows the normalized Kerr rotation versus magnetic field curves (M-H curves) for the 60-nm-thick Ni thin film as a function of electric field measured by MOKE magnetometry. Fig. 2-6a shows the polar geometry (i.e. out-of-plane magnetization change) and Fig. 2-6b shows the longitudinal geometry (i.e. in-plane magnetization change in both x and y directions). As shown in Fig. 2-6a inset, there are three different values of anisotropy field (H_a)

corresponding to three different poling/strain states of PMN-PT. From the initial un-poled state to a poled state with an electric field of 0.8 MV/m (refer to point 1 and point 3 in Fig. 2-4), H_a increases from ~2700 Oe to ~3500 Oe ($\Delta H_a \approx 800$ Oe). When the electric field is removed (i.e. point 4 in Fig. 2-4), H_a becomes ~3100 Oe which represents a ΔH_a of ~400 Oe. This intermediate value of H_a represents a change of anisotropy energy caused by a remnant strain at 0 MV/m (see point 4 in Fig. 2-4). Here, the presence of ΔH_a represents the increase of anisotropy energy required to magnetize/saturate the Ni thin film in the out-of-plane direction when either an electric field is applied or a remnant strain is present (i.e. the out-of-plane axis becomes "harder"). In addition, a change of coercivity, H_c, can also be observed in Fig 2-6a. H_c becomes smaller after the sample is poled/strained. This observation may also be attributed to the result of a harder out-of-plane direction. For a thin film sample, since the magnetic moment rotation between two opposite out-of-plane directions has to pass through the in-plane direction, when the in-plane direction is more energetically favorable due to strain, the out-of-plane coercivity could reduce accordingly.

Similar correspondence between the magnetization change and the poling/strain state can also be found in the longitudinal MOKE data shown in Fig. 2-6b. Fig 2-6b shows that the remanence significantly increases in both x and y directions when the PMN-PT is poled with an electric field of 0.8 MV/m (i.e. from point 1 to point 3 in Fig. 2-4). From the initial un-poled state to a poled state with an electric field of 0.8 MV/m, not only the remanence has significant change, but also the coercivity reduces by ~200 Oe. Both of these variations indicate a result of "easier" in-plane magnetization by applying an electric field to PMN-PT (i.e. inducing a compressive strain in the in-plane direction of Ni thin film). The increase in remanence represents an increase of in-plane magnetic domain structures (i.e. the in-plane direction

becomes “easier”) with the application of an electric field while the coercivity reduction may be attributed to a more coherent in-plane magnetic moment rotation during the magnetization reversal process with an electric field applied. The coherent in-plane magnetic moment rotation may be a result of a harder out-of-plane axis when the electric field is applied (i.e. spins are mainly confined to in-plane directions). Since every in-plane direction is an easy direction, a reduction of coercivity is possible and could represent an explanation of the coercivity reduction with electric field. When the electric field is removed (i.e. back to 0 MV/m as shown at point 4 in Fig. 2-4), the remanence decreases and the coercivity increases from those measured at the electric field of 0.8 MV/m. However, both remanence and coercivity are different to the values measured at the un-poled state. This is again due to the presence of remnant strain. One may notice that the remanence measured in the y direction is slightly smaller to that measured in the x direction at 0 MV/m (in both positive and negative Kerr rotation signal). This result may be attributed to different remanent strains in x and y directions as shown at point 4 in Fig. 2-4.

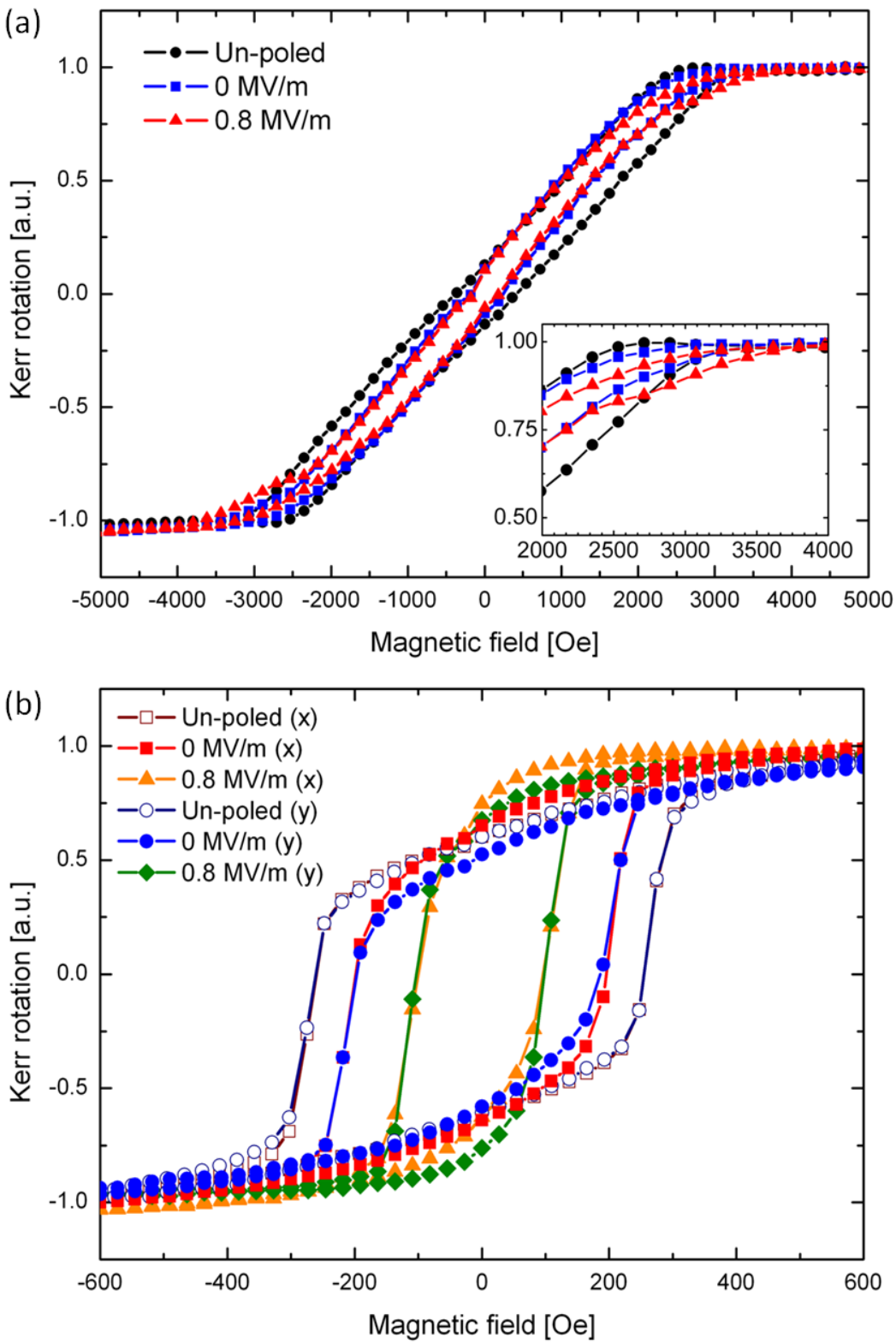

Figure 2-6: Normalized Kerr rotation hysteresis curves of 60-nm-thick Ni thin film on un-poled PMN-PT (001): (a) Polar and (b) Longitudinal geometry. Inset in (a): Approximate anisotropy field values at different poling states.

2.1.3.2 Ni thin film and pre-poled PMN-PT

2.1.3.2.1 Piezoresponse Curves

Fig. 2-7 shows the in-plane ε-E curves of the 60-nm-thick Ni/PMN-PT (001) pre-poled sample. As shown in Fig. 2-7, an isotropic in-plane compressive strain (i.e. $\varepsilon_x = \varepsilon_y$) as large as 1000 με is produced when an electric field of 0.8 MV/m is applied. As compared to the un-poled sample shown in Fig. 2-4, it is important to point out that remnant strain is absent in Fig. 2-7 when the electric field is removed. For the following MFM tests, the electric field was limited to the unipolar case of $0 \leq E \leq 0.8$ MV/m (i.e. points 1~4 in Fig. 2-7) to prevent de-poling and subsequent reversal of polarity.

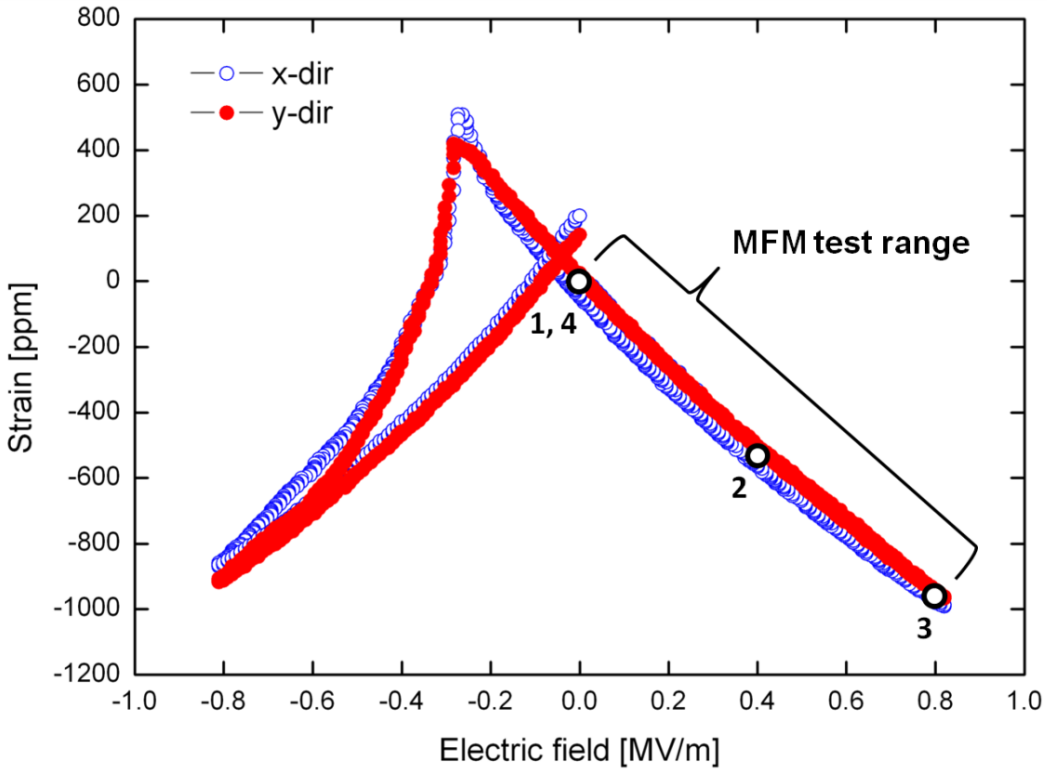

Figure 2-7: In-plane piezoelectric response of 60-nm-thick Ni/PMN-PT (001) pre-poled sample: (1) 0 MV/m, (2) 0.4 MV/m, (3) 0.8 MV/m, and (4) 0 MV/m.

2.1.3.2.2 Atomic Force and Magnetic Force Microscopy

Fig. 2-8 shows the AFM topographic height images and corresponding MFM domain images of the 60 nm Ni thin film captured at four different applied electric fields (i.e. points 1, 2, 3, and 4 in Fig. 2-7 corresponding to 0, 0.4, 0.8, and 0 MV/m respectively). As seen in Fig. 2-5a, the AFM images in Fig. 2-8 also show the presence of ferroelectric domains in the PMN-PT (with height difference between light and dark areas about ± 2 nm). When comparing the four AFM images, one sees that the surface texturing does not change during the application of electric fields (i.e. ferroelectric domains are immobile). Note that the surface topography with a more regular pattern was found in other AFM scanning areas on the PMN-PT sample surface.

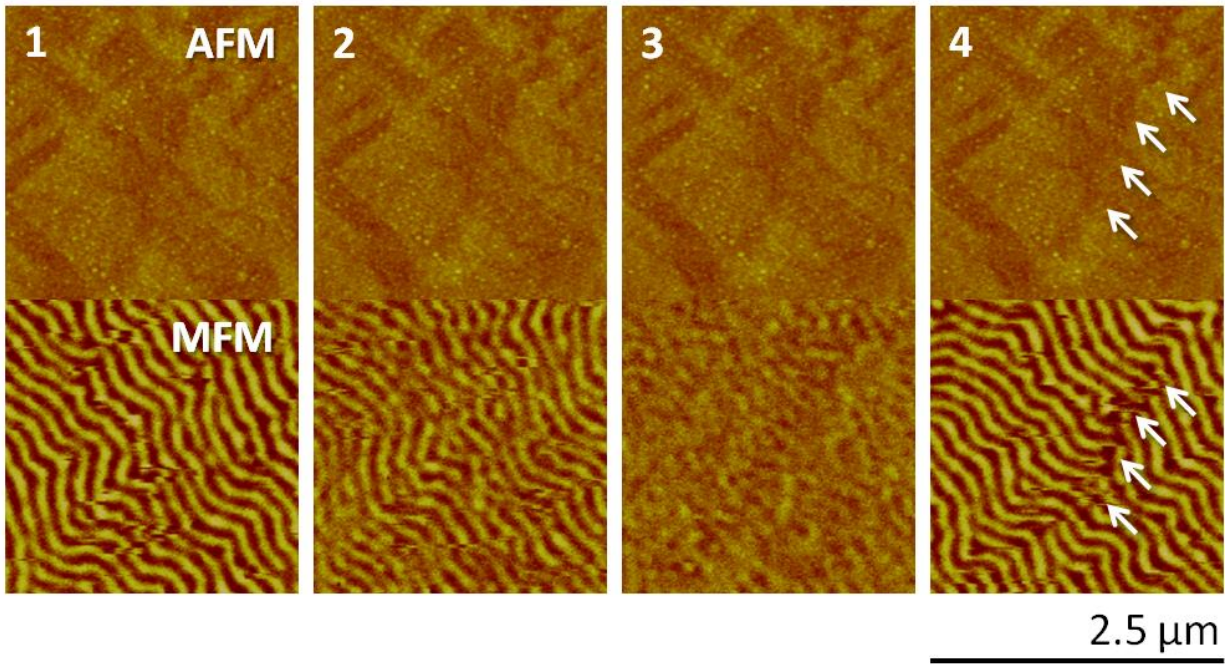

Figure 2-8: AFM and MFM images of 60-nm-thick Ni thin film on PMN-PT (001) pre-poled substrate: (1) 0 MV/m, (2) 0.4 MV/m, (3) 0.8 MV/m, and (4) 0 MV/m. Arrow signs in (4) point out the domain wall pinning locations.

When reviewing the four MFM images in Fig. 2-8, notable changes are observed in the magnetic domain structure. In Fig. 2-8.1 at 0MV/m, a typical stripe domain pattern is observed in the Ni thin film as others have reported [5-6]. As the electric field increases to 0.4 MV/m in Fig. 2-8.2, the stripe domain pattern contrast in the MFM image reduces. At an electric field of 0.8 MV/m in Fig. 2-8.3, the stripe domains in MFM image are virtually eliminated in the MFM image. The electric-field-induced isotropic compressive strains (see point 2 and 3 in Fig. 2-7) reduce the out-of-plane magnetic stray field suggesting that the magnetization is translating from out-of-plane to prominently in-plane. Upon removal of the electric field (i.e. back to zero strain at point 4 in Fig. 2-7), the stripe domain pattern in Fig. 2-8.4 is effectively recovered. However, the stripe domain distribution is slightly different from its original pattern as indicated by the white arrows in Fig. 2-8.4. Again, the texturing present in the AFM images (i.e. the immobile ferroelectric domain boundaries) is believed to pin the magnetic domain walls and produce a slightly different strip domain structure when compared to Fig. 2-8.1.

2.1.3.2.3 Magneto-optical Kerr Effect Magnetometry

Fig. 2-9 shows the M-H curves for the 60-nm-thick Ni thin film as a function of electric field measured by MOKE magnetometry. Fig. 2-9a shows the polar geometry and Fig. 2-9b shows the longitudinal geometry. In Fig. 2-9a, the polar MOKE data shows that the anisotropy field (H_a) increases from ~3700 Oe to ~4200 Oe (i.e. $\Delta H_a \cong 500$ Oe) as the electric field increases from 0 to 0.8 MV/m (see inset for a magnified view). As discussed in Section 2.1.3.1.3, this increase represents an increase of anisotropy energy required to magnetize/saturate the Ni thin film in the out-of-plane direction as an electric field is applied (i.e. the out-of-plane axis becomes "harder").

The longitudinal MOKE data in Fig. 2-9b shows that as the electric field is increased from 0 to 0.8 MV/m, the in-plane magnetic remanence increases and the magnetic coercivity decreases in both x and y directions. Again, the increase in remanence represents an increase of in-plane magnetic domain structures (i.e. the in-plane direction becomes "easier") with the application of an electric field while the coercivity reduction is attributed to a more coherent in-plane magnetic moment rotation during the magnetization reversal process with an electric field applied (also see Section 2.1.3.1.3).

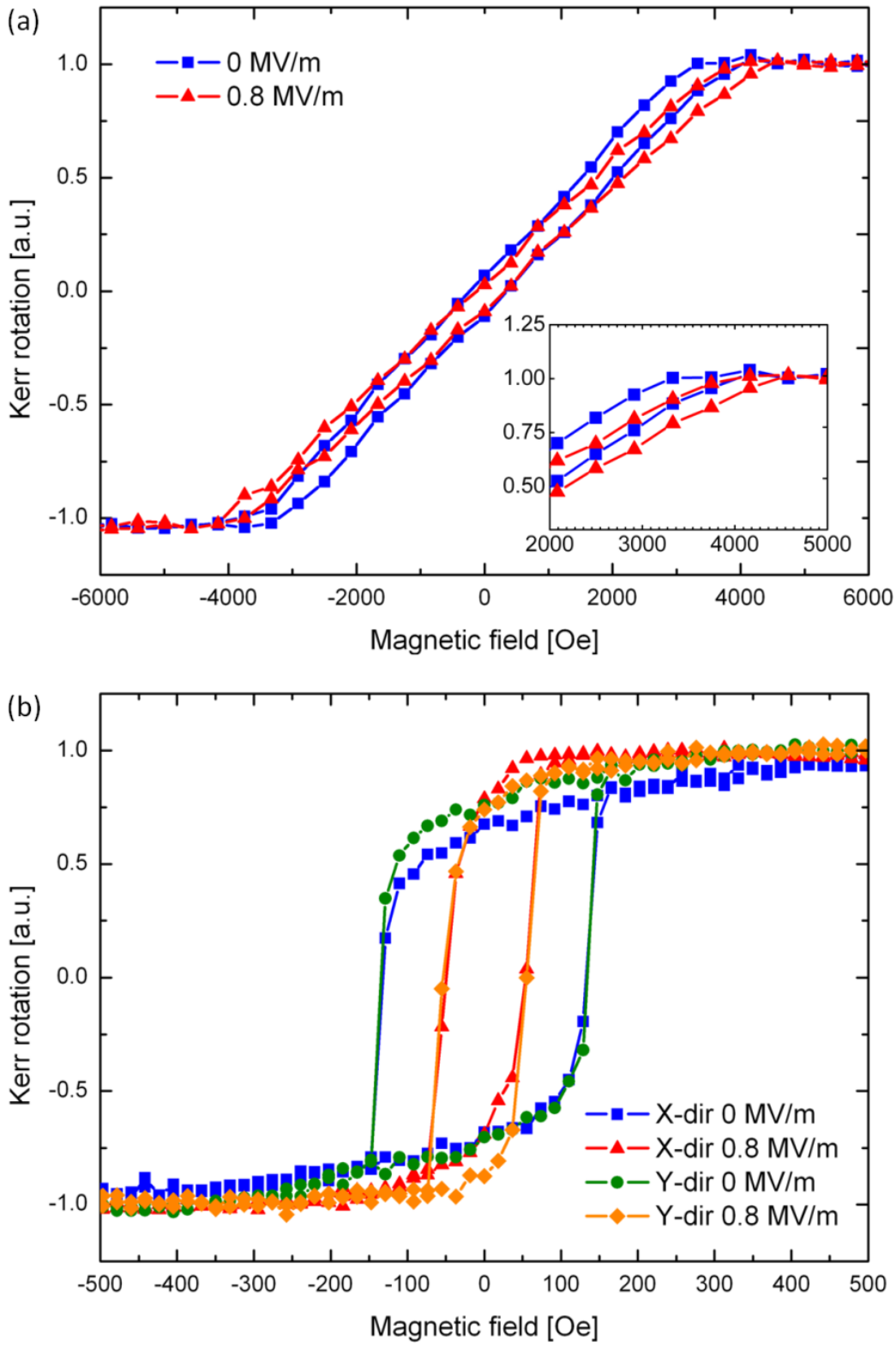

Figure 2-9: Normalized Kerr rotation hysteresis curves of 60-nm-thick Ni thin film on pre-poled PMN-PT (001): (a) Polar and (b) Longitudinal geometry. Inset in (a): Approximate anisotropy field values at different electric fields.

2.1.4 Discussion

2.1.4.1 Magnetostriction and Domain Structure

When similar MFM tests were conducted on the third sample, i.e. the 100-nm-thick Ni thin film sample, the stripe domain pattern did not change appreciably as a function of electric field (see Fig. 2-10). That is, in the boxed region of Fig. 2-10, there are some minor changes but these are fairly trivial compared to the changes observed in Fig. 2-5 or Fig. 2-8. Therefore, the reorientation of out-of-plane magnetization in Ni/PMN-PT (001) heterostructure is strongly dependent on Ni thin film thickness.

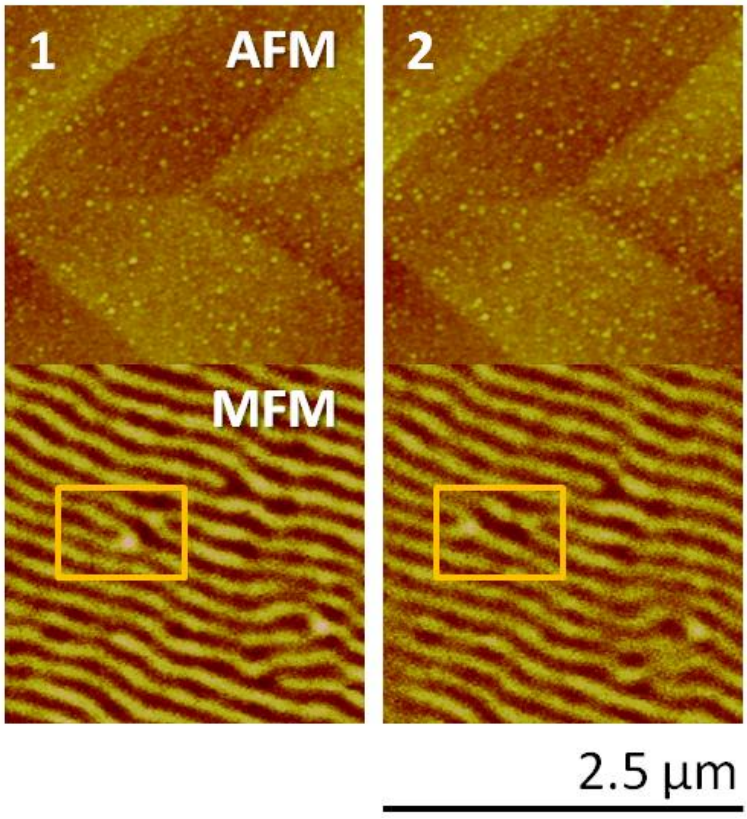

Figure 2-10: AFM and MFM images of 100-nm-thick Ni thin film on PMN-PT (001) un-poled substrate: (1) un-poled and (2) 0.8 MV/m. Distinct domain pattern change is observable only in the box areas.

Since the magnetic domain structure in Ni thin film is sensitive to thickness, it is misleading to define the easy and hard axis from simple observations of the M-H curves as pointed out by previous researchers [5]. However, the magnetoelastic change in energy produced by the application of electric-field-induced strain can be analytically calculated and compared to the magnetic anisotropy change observed in M-H curves as shown in Fig. 2-9. Since Ni is a negative magnetostriction material [25], isotropic in-plane compressive strains reorient out-of-plane magnetization to in-plane directions. For isotropic in-plane magnetostriction [25-26], the magnetoelastic energy change E_{me} can be calculated as:

$$E_{me} = (-3/2)\,\lambda_s\, E\, \varepsilon \sin^2\theta = 102 \text{ kerg/cm}^3 \tag{2.1}$$

where the magnetostriction constant $\lambda = -34$ ppm and the Young's modules E = 200 GPa for Ni [25], the strain $\varepsilon = 1000$ με at 0.8 MV/m (see point 3 in Fig. 2-7), and θ is the 90° change from out-of-plane to in-plane directions. This energy can be compared to the magnetic anisotropy energy change E_a calculated from Fig. 2-9a:

$$E_a = (1/2)\,\Delta H_a\, M_s = 109 \text{ kerg/cm}^3 \tag{2.2}$$

where $\Delta H_a = 500$ Oe and the saturation magnetization $M_s = 435$ emu/cm^3 for Ni thin film [3]. One finds that the magnetoelastic energy E_{me} input to the system is very close to the change of magnetic anisotropy energy E_a measured in the system. This correlation between E_{me} and E_a supports the described physical mechanism of domain pattern change in the MFM images of Fig. 2-8 (i.e. out-of-plane magnetization change).

However, theoretical predictions for a complete reorientation of the out-of-plane easy axis in Ni thin film [22-23] suggest substantially larger strains than the 1000 με shown in Fig. 2-7. These analytical results did not consider the actual domain structure in Ni thin film where both the Bloch wall and Néel wall coexist to form magnetic flux closures [4] and may not accurately

reflect the experimental results shown in this study. To better explain the discrepancy, illustrations of the domain structure changes (i.e. the change of magnetic flux closure before and after the thin film is strained) along with the corresponding MFM images are provided in Fig. 2-11. Fig. 2-11 shows that before the strain is induced, some magnetic flux exits the sample due to the thickness of the Ni thin film as previously reported [3-4]. The out-of-plane stray fields (i.e. N and S shown in Fig. 2-11) are sensed with the magnetic probes as shown in the adjacent MFM image (also see Fig. 2-8.1). While large out-of-plane magnetization components exist, the in-plane domain structure illustrated in Fig. 2-11a is relatively small. Fig. 2-11b shows an illustration of the domain structure following the application of electric-field-induced strain. As can be seen, the size of the in-plane domains increases and the out-of-plane decreases. The mechanism for the increase of in-plane domains is attributed to an increase of Néel wall area (i.e. solid blue lines in Fig. 2-11) while the Bloch wall area (i.e. dashed red lines in Fig. 2-11) is reduced. Furthermore, as the Néel walls expand, they begin to "cap" the out-of-plane domains (as compared to Fig. 2-11a) significantly reducing the out-of-plane stray field and thus reducing the contrast in the MFM image (also see Fig. 2-8.3). In addition, since the Bloch wall consists of spins with 180° rotation in the out-of-plane direction, it is also expected that the Bloch walls are also broadening because the spins in Bloch walls tend to stay in the in-plane direction when a strain is induced. As the thickness of the Ni thin film increases (i.e. from 60 to 100 nm), the in-plane domains become less energetically favorable and the energy required to reduce (or broaden) the Bloch walls is larger than that which is available from the PMN-PT substrate (i.e. 1000 με). Therefore, for thicker films (e.g. 100 nm), the 1000 με is insufficient to dramatically alter the out-of-plane stray fields and thus changes in MFM images were not observed in the thicker films.

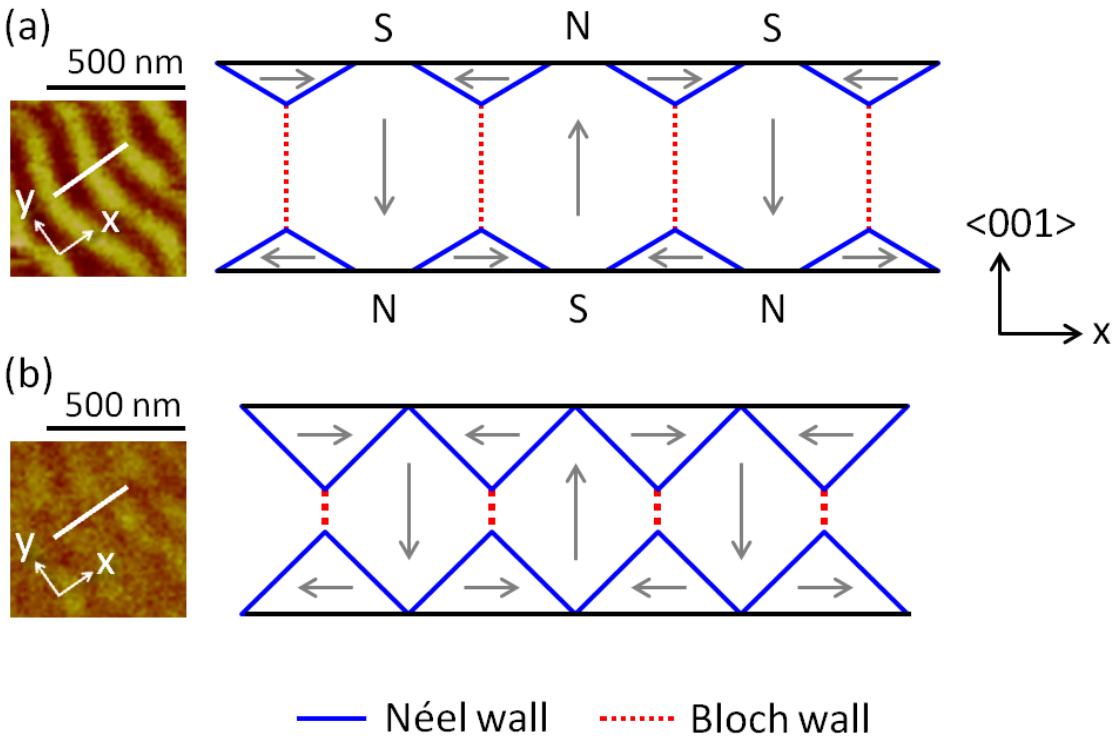

Figure 2-11: 2-D schematic diagrams of flux closure domain configuration in the cross-section of 60-nm-thick Ni thin film MFM images (refer to Fig. 2-8): (a) zero strain at 0 MV/m and (b) isotropic in-plane compressive strain at 0.8 MV/m. White lines on MFM images represent possible cross-section positions. Gray arrows represent the magnetization direction of each domain: "out-of-plane domains" have arrows pointing to the <001> directions and "in-plane domains" have arrows parallel to the x axis. N and S represent the polarity of stray fields exiting the sample surface.

One may notice that the electric field required to eliminate the stripe domains in anisotropically strained films (see Fig. 2-5.2b) is less than reported for isotropically strained films (see Fig. 2-8.3). Based on the piezoelectric response of the un-poled PMN-PT sample shown in Fig. 2.4, this difference may be attributed to a larger strain change induced in the nonlinear region during the poling process (see points 1~3 in Fig. 2-4) or the anisotropic strains that arise during poling.

2.1.4.2 Domain wall pinning

While the strain-induced domain configuration change in Ni/PMN-PT heterostructure has been discussed, the mechanism of domain wall pinning observed in this chapter is still unclear. By closely observing the out-of-plane stray field change in the MFM images (e.g. Fig. 2-5.2c and Fig. 2-5.3c), it is possible to pose a mechanism based on the flux closure domain configuration as shown in Fig. 2-12. Fig. 2-12a shows that when the sample is un-poled, some magnetic flux exits the sample surface as evidenced by the out-of-plane stray fields (i.e. N and S shown in Fig. 2-12 illustrations) observed in the MFM image (also see Fig. 2-5.1c). These distinct stripe domains suggest that the in-plane magnetization structures are much smaller than the out-of-plane magnetization structures in the un-poled state. Fig. 2-12b shows a possible configuration of the domain structure following the application of an electric-field-induced strain (800 to 1200 με at 0.4 MV/m). Here, the in-plane magnetization components are believed to generally increase as the out-of-plane components decrease with the exception of the "capping" in-plane magnetization structure at the Bloch wall pinning site. The in-plane magnetization increase as well as out-of-plane stray field decrease causes significant changes in the local magnetic anisotropy energy which results in a breakup of the stripe domain structure such that a "mottled" domain image is observed in the MFM experiments. When the electric field is increased to 0.8 MV/m (1350 to 1550 με) in Fig. 2-12c, out-of-plane stray fields (i.e. the "crack-like" structures) are observed locally in the MFM image at specific locations (i.e. the pinning sites, where the surface texture produced by ferroelectric domains is prominent, also see Fig. 2-5.2 and Fig 2-5.3) rather than uniform stripe domains as presented in Fig. 2-12a. This localization of the out-of-plane stray fields is attributed to Bloch wall pinning which causes the "capping" phenomenon described in Fig. 2-12b to vanish when sufficient magnetoelastic energy is provided.

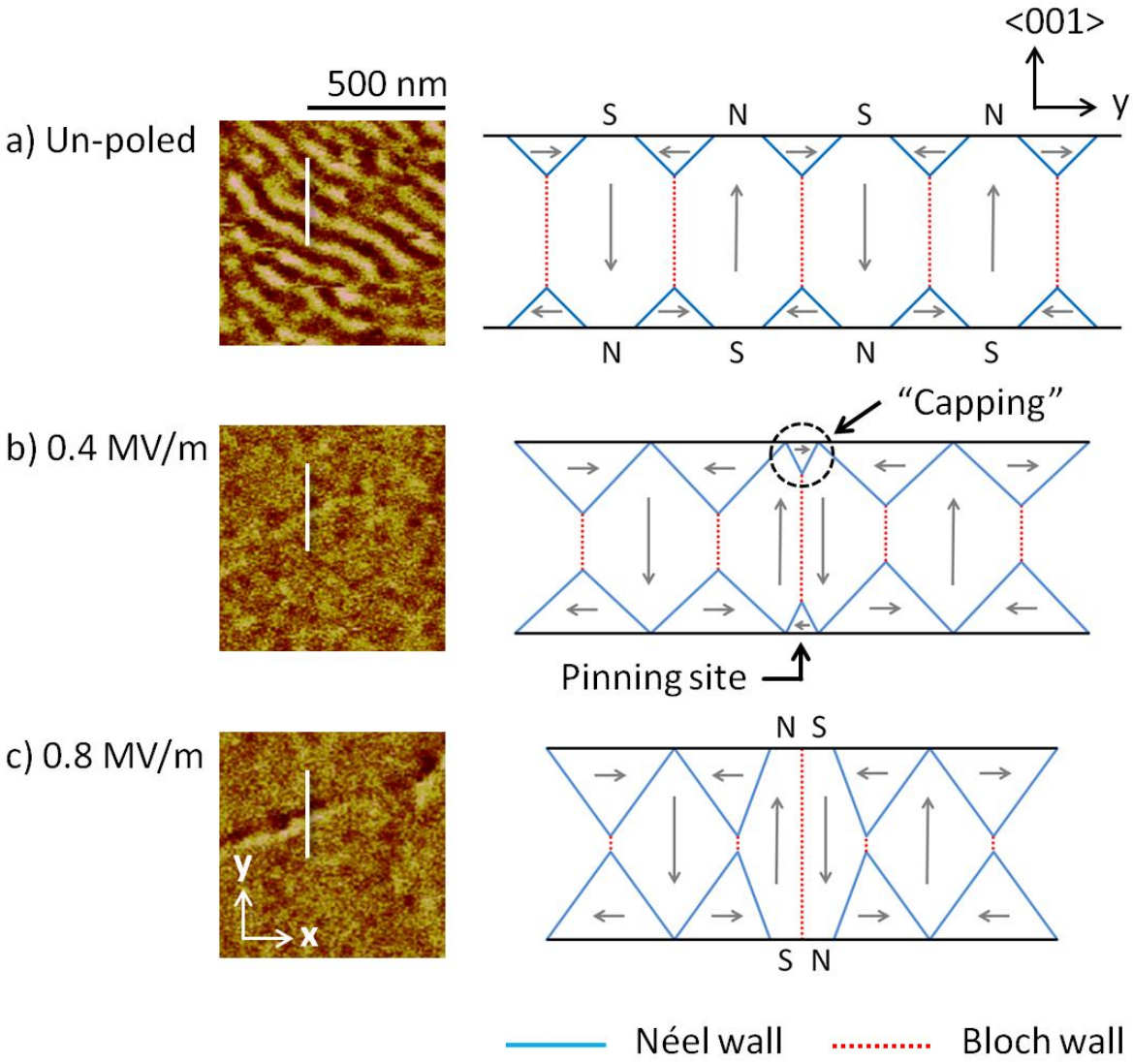

Figure 2-12: 2-D schematic diagrams of flux closure domain configuration in the cross-section of 60-nm-thick Ni thin film MFM images (refer to Fig. 2-5): (a) un-poled, (b) poled at 0.4 MV/m, and (c) poled at 0.8 MV/m. White lines on MFM images represent possible cross-section positions. Gray arrows represent the magnetization direction of each domain: arrows pointing to the <001> directions represent out-of-plane magnetizations and arrows lying along the y-axis represent in-plane magnetizations.

2.2 Nanostructure

Over the past decade, patterned nanostructure with a single domain formation [27-28] have been suggested as one approach to enhance the magnetic properties of ferromagnetic materials. By inducing shape or magnetocrystalline anisotropy in the nanoscale, researchers have been able to fabricate ferromagnetic single domains to tailor magnetic properties such as coercivity and remanence [29-30]. Typical dimensions of single domain nanostructures fabricated with 3d ferromagnetic elements (Co, Ni, and Fe) are on the order of 50 to 500 nm [27]. In this section, the theory of shape anisotropy induced single domain proposed by Charles Kittel [31] is reviewed. A typical fabrication process of single domain Ni nanostructures is also introduced. Based on the modeling and experimental results, a comparison between theoretical calculation and experimental observation of single domain dimension is shown.

2.2.1 Single Domain Theory (by Charles Kittle [31])

The total free energy of a ferromagnetic sample can be simplified as the sum

$$E = E_w + E_m + E_a \tag{2.3}$$

where E_w is domain wall energy, E_m is magnetostatic energy, and E_a is anisotropy energy which accounts for spins not aligned in the easy axis. Since the domain wall energy is a surface energy, E_w can be denoted as

$$E_w = \sigma_w S \tag{2.4}$$

where σ_w is surface energy density energy and S is the total area of domain wall. The magnetostatic energy associated with demagnetization factor N_d can be expressed as

$$E_m = (-1/2) \int (H_d M)\, dV = (-1/2)\,(-N_d M)\, M\, V = (1/2)\, N_d M^2 V \tag{2.5}$$

where H_d is demagnetization field, M is magnetization, and V is volume. The value of N_d

depends on the shape of the sample (i.e. aspect ratio), and can be calculated in closed form for rectangular prisms [32] or ellipsoidal bodies [33].

Consider a ferromagnetic sample which has dimensions that produce single domain as shown in Fig. 2-13. In Fig. 2-13a, all the spins in the sample are aligned and point along the longitudinal direction to form a single domain, and the longitudinal direction is the easy direction. In this case, E_w and E_a are zero since both domain wall and the spin lying in the hard direction do not exist, and thus Eqn. (2.3) for the single domain becomes

$$E_{sd} = E_m = (1/2)\, N_d\, M^2\, (L\ W\ T) \tag{2.6}$$

where L, W, and T are the length, width, and thickness of the sample as shown in Fig. 2-13a respectively.

Fig. 2-13b shows that when the sample size is slightly larger, more than one domain exists in the sample and the domains start to form a flux closure to minimize E_m (i.e. $E_m = 0$). In the multi-domain case of Fig. 2-13b, since only spins in small areas on the two ends of the sample point to the hard direction, E_a is assumed to be negligible. As a result, Eqn. (2.3) for the multi-domain becomes

$$E_{md} = E_w \approx \sigma_w\, (LT) \tag{2.7}$$

where L is the length and T is the thickness of sample as shown in Fig. 2-13b. By equating Eqn. (2.6) and Eqn. (2.7), the critical width W_c of single domain can be obtained

$$(1/2)\, N_d\, M^2\, W_c = \sigma_w,$$

$$W_c = 2\, \sigma_w / N_d\, M^2 \tag{2.8}$$

Note that this critical width is dependent on N_d which is a function of the aspect ratio of sample. Therefore, once W_c is obtained, L_c and T_c can also be calculated based on the aspect ratio of the sample. In general, Kittel's theory gives an approximate solution for the calculation of single

domain dimensions, especially when shape anisotropy is present.

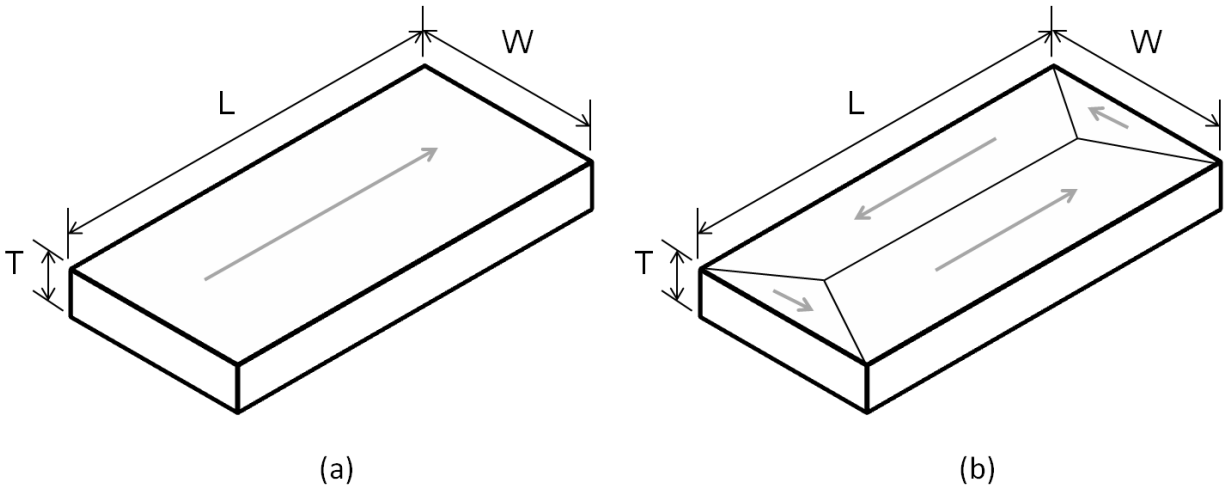

Figure 2-13: Domain configuration in a rectangle prism at the nanoscale: (a) Multi-domain with a flux closure, and (b) Single domain. Gray arrows represent the magnetization direction of domain.

2.2.2 Numerical Modeling

Kittel's theory basically elucidates that single domains can only form below a certain scale even though a larger sample may have the same N_d value (i.e. the same aspect ratio) as a smaller one. For example, a 3000 by 1000 by 350 nm^3 Ni sample has the same aspect ratio as a 300 by 100 by 35 nm^3 Ni sample (i.e. L:W:T = 60:20:7); however, only the later one has single domain. Therefore, if one tries to predict the single domain formation in a ferromagnetic nanostructure with a specific aspect ratio, Kittel's theory can be used to model the magnetic domain configuration.

From the engineering point of view, since the majority of single domain Ni nanostructures are fabricated using processes involving thin film deposition [27-28] in which the sample thickness is the first parameter to decide, the nanostructure thickness could be the first parameter to consider for modeling. Fig. 2-14 is an example result of modeling the critical

dimensions of Ni nanostructure with various aspect ratios but a fixed thickness using the Kittel's theory. Thickness T = 35 nm, M = 485 emu/cm^3, and σ_w = 0.9 erg/cm^2 are the input parameters for the modeling. Note that σ_w value used here is an average of Bloch and Néel wall energy of Ni [25]. A MATLAB code for the numerical modeling, including a subroutine of N_d calculation for rectangular prisms, is provided in Appendix 1. In Fig. 2-14, the dark region represents the possible lengths and widths of multi-domain nanostructure and the triangular-colored region represents the possible lengths and widths of single domain nanostructure. The boundary separating these two regions represents the critical dimensions of single domain. For example, a Ni nanostructure with a size of 600 by 300 by 35 nm^3 has multi-domain, but a 600 by 100 by 35 nm^3 Ni nanostructure is a single domain.

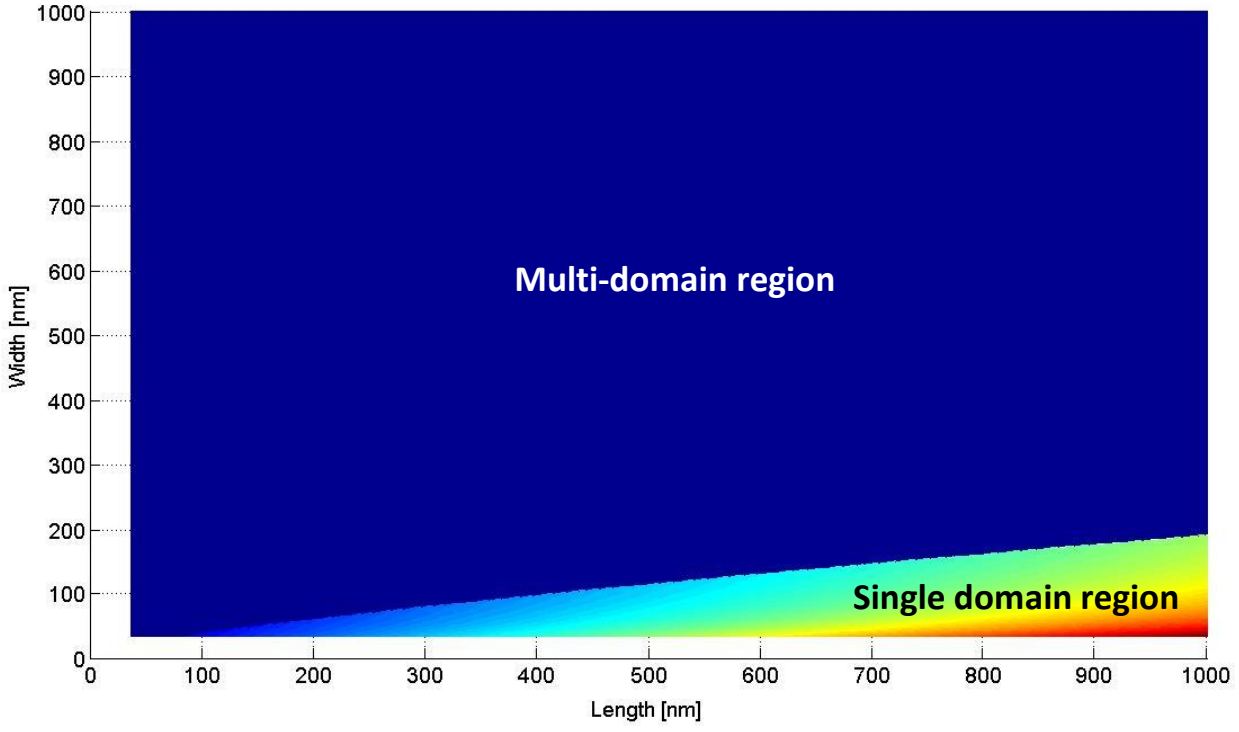

Figure 2-14: Modeling results of domain configuration as a function of Ni nanostructure dimensions. The nanostructure thickness is fixed at a T = 35 nm.

2.2.3 Fabrication

Based on the modeling results, Ni nanostructures with three different dimensions (300 by 150 by 35 nm^3, 300 by 100 by 35 nm^3, and 600 by 100 by 35 nm^3) were fabricated using E-beam lithography, E-beam evaporation, and lift-off process. A process flow chart is shown in Fig. 2-15. In Fig. 2-15a, PMMA 495 A4 E-beam resist was first spin-coated on Si wafer surface. The PMMA resist was exposed using a Vistec EBPG5000+ E-beam lithography system to form an array of nanostructures with various sizes. The patterned resist was then developed with a MIBK/IPA solvent. In Fig. 2-15b, 5-nm-thick Ti was E-beam evaporated onto the developed resist as an adhesive layer. This was followed by the evaporation of 35-nm-thick Ni thin film without breaking the vacuum. Finally, as shown in Fig. 2-15c, the PMMA sacrificial layer was removed using acetone producing an array of Ni nanostructures. An AFM image of fabricated Ni nanostructure array is shown in Fig. 2-16.

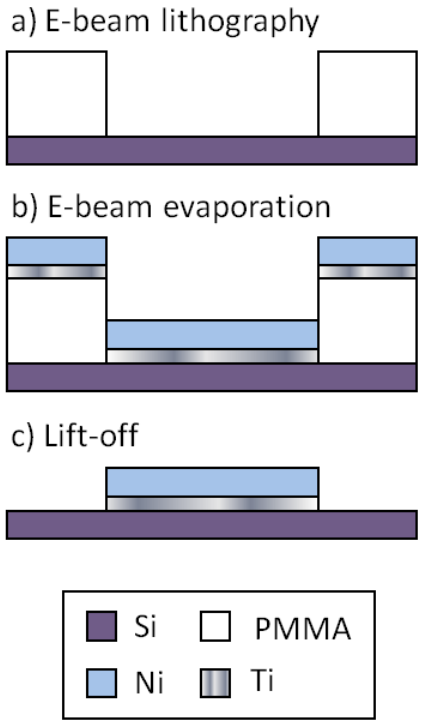

Figure 2-15: Process flow chart of Ni nanostructure fabrication.

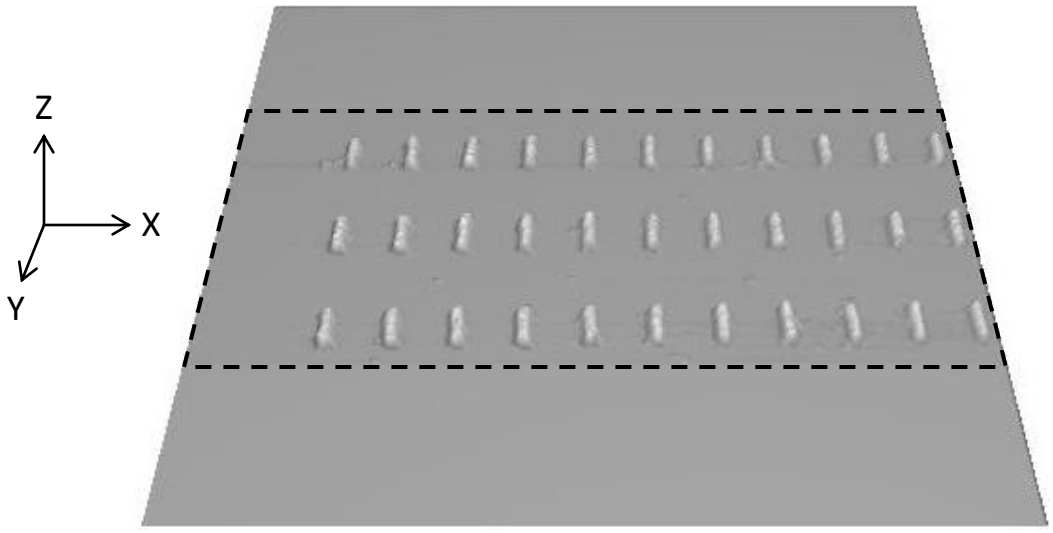

Figure 2-16: Three dimensional AFM topographic image of Ni nanostructure (600 by 100 by 35 nm^3). The normal direction of sample surface is along the Z-axis. The box area size shown by dashed lines is 5 μm by 10 μm.

2.2.4 Experiment and Discussion

The magnetic domain images of fabricated Ni nanostructures were captured using the Bruker Dimension 5000 MFM. A standard MFM probe (Bruker MESP) magnetized along the tip axis was used for all imaging. Fig. 2-17 shows the captured MFM images of Ni nanostructures with three different geometries. In Fig. 2-17a, single domain and multi-domain were both observed in the Ni nanostructure with a dimension of 300 by 150 by 35 nm^3. The single domain in the MFM images is represented by one bright and one dark region in each nanostructure (i.e. one dipole per structure). For example, in the boxed zoom-in area of Fig. 2-17a, the domain structure on the right-hand side is a single domain. Fig. 2-17b and Fig. 2-17c show that single domain forms in all the 300 by 100 by 35 nm^3 and 600 by 100 by 35 nm^3 Ni nanostructures. These MFM results suggest that the Ni single domain is induced by increasing the aspect ratio (i.e. the shape anisotropy) of nanostructures.

Fig. 2-17 further shows a comparison between experimental and modeling results (refer to Fig. 2-14). In general, the experimental results match with the modeling results; however, some discrepancies can still be found. For example, for the 300 by 100 by 35 nm^3 Ni nanostructures (see Fig. 2-17b), the modeling shows a result of multi-domain while MFM results show only single domain. In fact, the modeling result suggests that with the same aspect ratio (i.e. L:W:T = 60:20:7), the single domain only forms in a smaller structure with a size of 224.67 by 74.89 by 26.21 nm^3. However, the modeling also shows that a 320 by 80 by 35 nm^3 Ni nanostructure should be a single domain (i.e. different aspect ratio but with dimensions close to 300 by 100 by 35 nm^3). Therefore, the discrepancy between modeling and experimental results in Fig. 2-17 is believed to be caused by either the dimensional errors introduced in the fabrication process or the errors introduced in the Kittel's theory due to simplifications. Overall speaking, results shown in Fig. 2-17 suggest that even though some assumptions were used in the Kittel's theory to calculate the critical dimensions of single domain, this theory is still worth referencing when the single domain nanostructure is made of Ni.

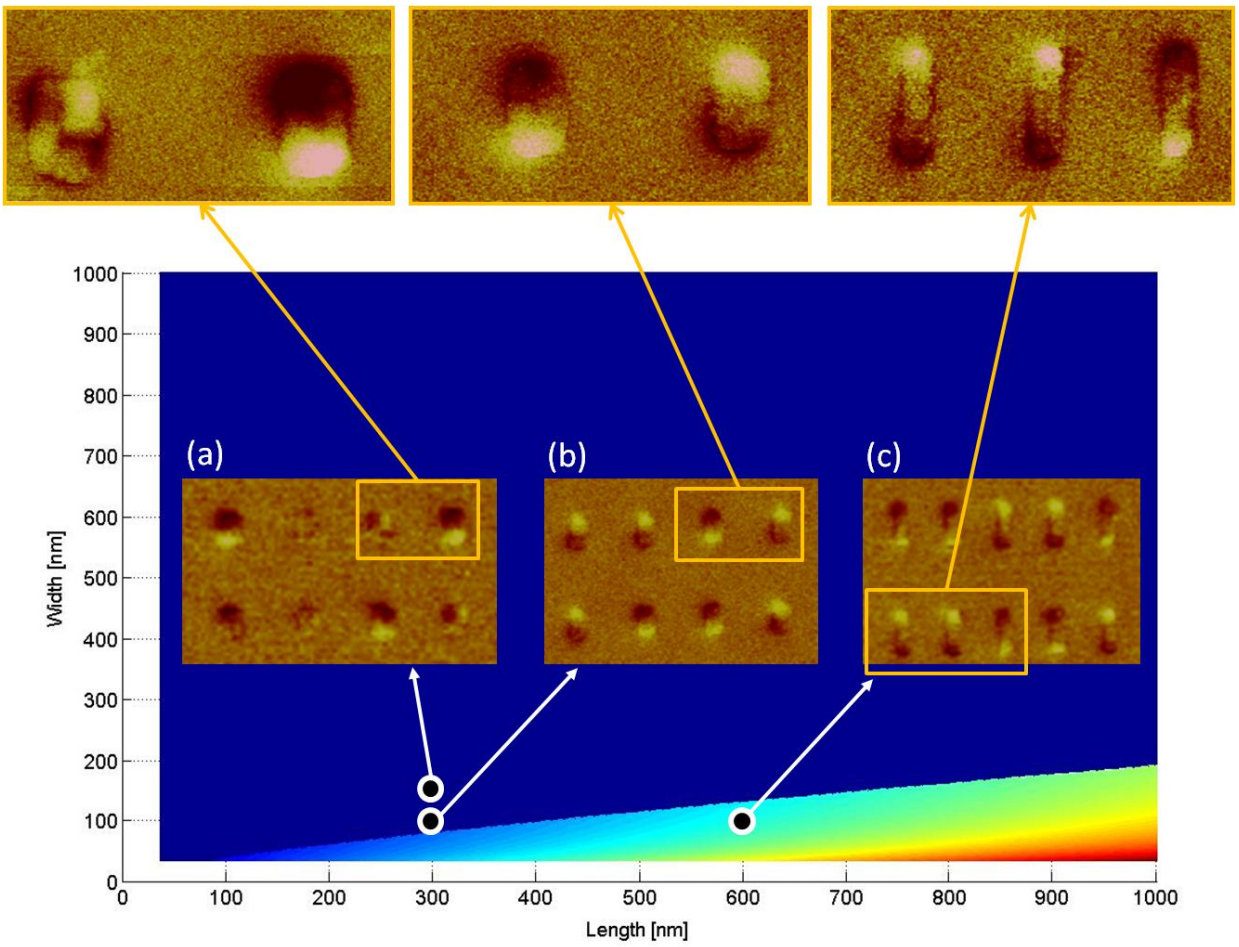

Figure 2-17: Comparison between MFM and modeling results of single domain Ni nanostructures. The single domain in MFM images is represented by one bright and one dark region in each nanostructure (i.e. one dipole per structure; for example, only three single domains are shown in (a)). The dimension of Ni nanostructures: (a) 300 by 150 by 35 nm^3, (b) 300 by 100 by 35 nm^3, and (c) 600 by 100 by 35 nm^3.

2.3 Summary

Significant magnetic domain configuration changes in the Ni thin films and nanostructures have been observed by changing either their strain states or shape anisotropy. For the nanoscale Ni thin films, magnetic domain structure can be electrically manipulated through a strain-mediated converse magnetoelectric effect with PMN-PT. The ability of changing domain configuration is found to be thickness dependent. For the Ni nanostructures, single domains can be induced by fabricating the structures into a geometric shape with higher aspect ratios. The formation of Ni single domain is shown to be predictable even with a simplified theory. The experimental results of both Ni thin films and nanostructures show the feasibility of engineering magnetic anisotropy to control magnetic properties at the nanoscale.

CHAPTER 3

NANOSTRUCTURED GADOLINIUM

In this chapter, the magnetic anisotropy of 25-nm-thick textured Gd thin film and an array of patterned 1400×70×50 nm^3 Gd nanobar structures is studied. Shape anisotropy induced single domain was not observed in either thin film or the nanobars over a temperature regime from 53 K to 273 K. However, the Gd thin film exhibited a magnetocrystalline anisotropy induced spin-reorientation due to the hcp (002) texture. This result is different from that reported for epitaxial Gd thin film with similar thickness. A shift of Curie temperature T_c relative to bulk Gd was also found for this thin film. In addition, experimental results suggest significant oxidation occurs along with the formation of fcc crystal structure in the Gd nanobars. The observed crystalline change in the nanobar is related to the stacking fault caused by local oxidation induced stresses which does not occur in the textured thin film. The experimental findings and their relationship to single domain are discussed.

3.1 Background

Magnetic 3d transition and 4f rare earth elements are being studied for use in various applications including magentocaloric refrigeration [34] and thermomagnetic generation [35-37]. The recent clean energy demands have encouraged researchers to focus on improving the magneto-thermal properties of these elements and their alloys. As discussed in the previous chapter, the single domain nanostructures are a useful approach to enhance the magnetic properties of ferromagnetic materials. However, while the single domain in 3d ferromagnetic

elements (Co, Ni, and Fe) has been extensively studied [27], reports of single domain in 4f elements are relatively absent in the literature [38]. Therefore, more work is required to better understand the magnetic properties of 4f elements in the nanoscale.

Among all the 4f elements, gadolinium (Gd) has received substantial attention due to its unique large magnetic moment and Curie point (T_c = 287~294 K) [39] near room temperature. For example, Gd has been proposed for use as an ambient thermomagnetic energy harvesting [35, 40-41] and magnetocaloric refrigeration [34] concepts. Several studies have reported the fabrication and characterization of Gd epitaxial thin films [42-45], multilayers [46-47], nanocrystalline structures [48-50], and nanoparticles [38, 51-53] suggesting the magnetic properties change dramatically in the small scale. One of the first studies on single domain Gd was conducted by Chizhov et al. [38] in 1982. Based on X-ray diffraction (XRD) and electron microscopy analysis results, they reported that a crystallographic phase transformation occurs when Gd particles approach 20-400 nm in size. The increased surface to volume ratio was suggested to change the crystal structure from hexagonal close-packed (hcp) to face-centered cubic (fcc) (i.e. fcc Gd non-magnetic). This conclusion was subsequently questioned by Singh and Curzon [54], where they attributed Chizhov's characterization results to material contaminations (e.g. oxidation and hydrogenation). However, recent reports support the structural phase transformation observed in Gd particles ~10 nm [51-52], but other reports show ~40 nm Gd nanoparticles are hcp crystal structure [53]. These controversial findings have left a considerable uncertainty about the magnetic properties of Gd in the nanoscale.

3.2 Fabrication

3.2.1 Thin Film

25-nm-thick Gd thin film was deposited on a p-type (001) Si wafer using an ultra high vacuum (UHV) sputtering system. After pumping down to ~5×10^{-8} Torr, DC sputtering was carried out in an Ar atmosphere under a gas pressure of 10^{-3} Torr with a flow rate of 20 sccm. Using 99.9% pure Gd target, 25-nm-thick thin film was sputtered at 30W. The deposition rate is 1 Å/s. This was followed by the in-situ deposition of a 20-nm-thick capping Pt layer to prevent oxidation of Gd thin film [55]. After the deposition, the sample was processed with a focused ion beam (FIB) in the FEI Nova 600 scanning electron microscope (SEM) to check the thin film thickness. The SEM image of thin film cross-section is shown in Fig. 3-1.

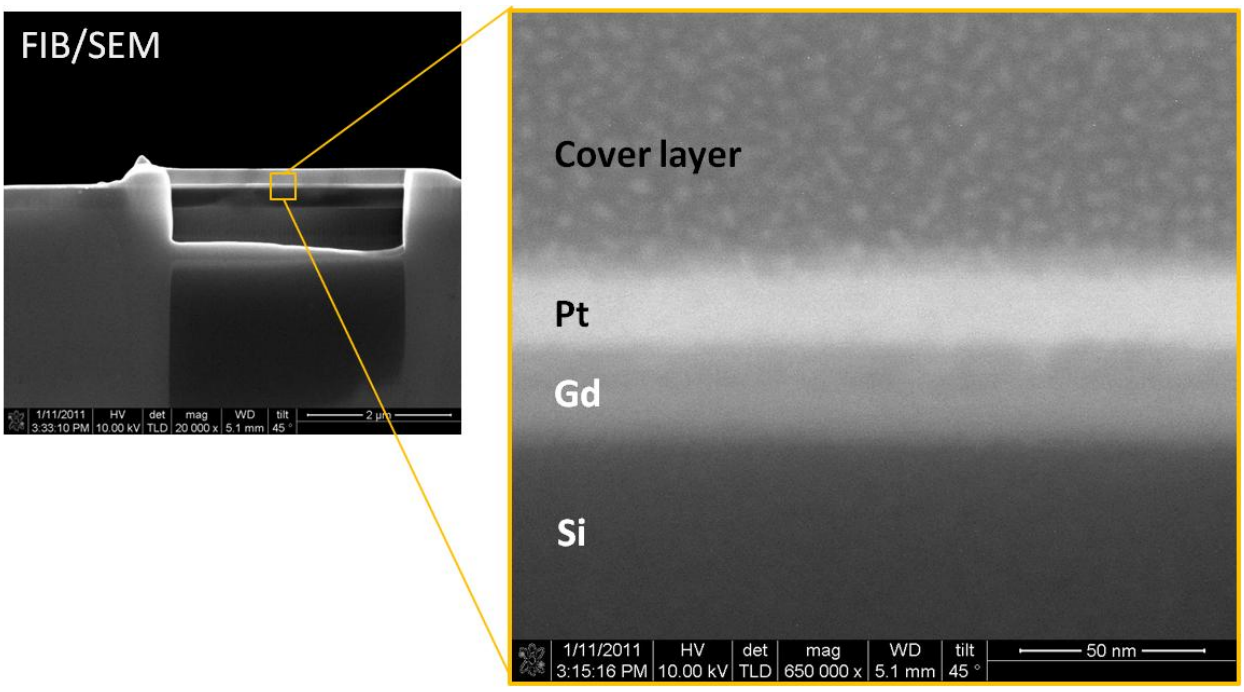

Figure 3-1: Cross-sectional SEM images of 25-nm-thick Gd thin film. For the FIB processing purpose, the cover layer was deposited on top of the sample surface in the FIB milling area.

3.2.2 Nanostructure

Gd nanobars were fabricated on top of a p-type (001) Si wafer using E-beam lithography, E-beam evaporation, and a lift-off process. PMMA 495K A4 resist was first deposited on the wafer. The PMMA resist was exposed using a Vistec EBPG5000+ E-beam lithography system to form an array of similar nanobars. The patterned resist was developed with a MIBK/IPA solvent. This was followed by E-beam evaporating 50-nm-thick 99.9% pure Gd in a vacuum better than 5×10^{-7} Torr. A 10-nm-thick capping Pt layer was also deposited in-situ without breaking the vacuum. Finally, the PMMA sacrificial layer was removed using acetone producing an array of Gd nanobar structures. The process flow is similar to the one shown in Fig. 2-15.

Fig. 3-2 shows the SEM images of the fabricated Gd nanobars. All the nanobars were patterned in an area of ~ 5×5 mm^2. For the purpose of inducing a strong shape anisotropy to form a single domain in Gd nanobar, the nanobar dimensions were chosen based on the Kittel's theory [31] as discussed in Chap. 2. As shown in Fig. 3-2, the nanobar structure has a high aspect ratio of L/W ≅ 20 (i.e. ~1400 nm × 70 nm), where the length L is defined as the easy axis. Based on the results of dipole field calculation [26], the nanobars were sufficiently spaced to prevent magnetic interaction. The total number of nanobars was chosen to produce a magnetic moment measurable (~10^{-6} emu) in the SQUID (superconducting quantum interface device) magnetometer.

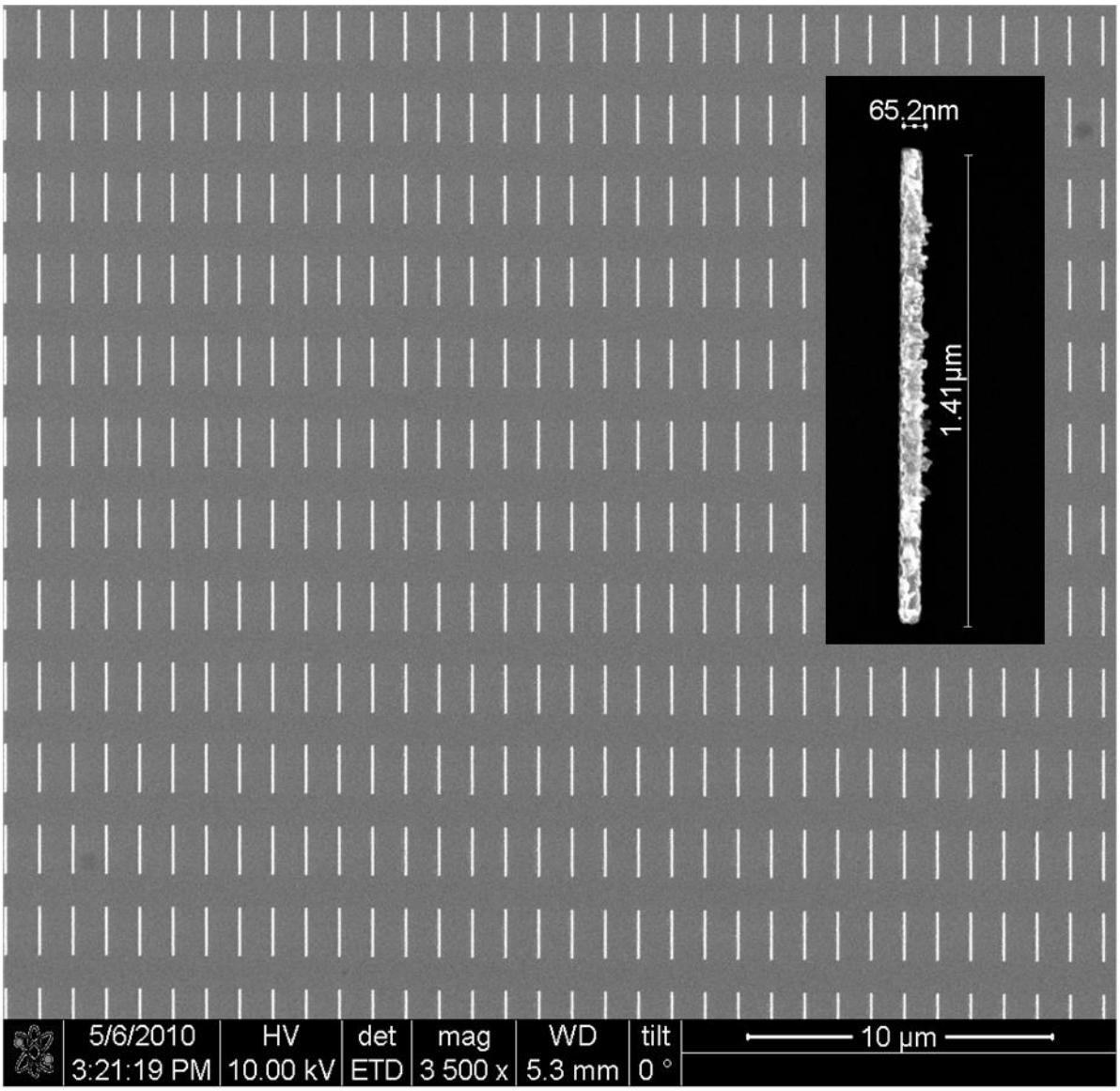

Figure 3-2: SEM images of Gd nanobars. The inset shows the actual dimensions of one nanobar.

3.3 Characterization

The magnetic moments of both thin film and nanobar array were measured using a Quantum Design MPMS SQUID magnetometer. All the magnetic data presented in this study were measured along the in-plane direction of thin film and the longitudinal direction of nanobars (i.e. parallel to the easy direction). Zero-field-cooled and field-cooled (ZFC-FC) measurements were conducted on Gd thin film by first heating to the paramagnetic state at 350 K and cooling down to 10 K under a zero applied field (i.e. ZFC). At 10 K, a field of 50 Oe was applied and the magnetic moment was measured in 10 K increments up to 350 K. This was followed by the FC moment measurement as the sample was cooled back down to 10 K under 50 Oe. Isothermal magnetization curves of thin film were also measured in the temperature range of 53 ~ 303 K at applied fields up to 50 kOe and the data were further was used to construct the Arrott plot [56] to evaluate T_c. Isothermal magnetization curves of Gd nanobar were measured in the temperature range of 53 ~ 253 K at applied fields up to 10 kOe.

Magnetic force microscopy (MFM) measurements were conducted with a Bruker Dimension Icon atomic force microscope (AFM). A standard MFM probe (Nanosensors PPP-MFMR) magnetized along the tip axis was used. The vender reports that the probe has a coercivity of ~300 Oe and a remanence magnetization of ~300 emu/cm^3. A sample stage capable of varying temperature from 238 to 523 K was used to observe the domain configuration of Gd thin film and nanobars. The sample chamber was purged with nitrogen to prevent condensation during measurements. Prior to capturing MFM images, the stage temperature was held constant for five minutes. MFM images were captured in 10 K interval starting from 253 to 293 K. A control test was conducted by repeating the imaging procedure using a non-magnetic AFM probe to confirm the MFM measurements.

The crystal structure of Gd thin film and nanobar was characterized using XRD and transmission electron microscopy (TEM) respectively. XRD characterization was performed using the Cu Kα radiation in a PANalytical X'Pert pro. TEM characterization was carried out in a FEI Titan operated at 300kV. TEM samples were prepared using a FEI Nova 600 dual-beam SEM/FIB (scanning electron microscope/focused ion beam) system. Fast Fourier transform (FFT) patterns were used to analyze the high resolution TEM (HRTEM) images. The oxidation content in different regions of Gd nanobars was measured using an energy dispersive X-ray spectrometer (EDS) attached on Titan.

3.4 Results and Discussion

3.4.1 Thin Film

Fig. 3-3 shows the XRD pattern of the sputtered Gd thin film and bare Si substrate. The peaks at $2\theta = 30.89°$ and $39.72°$ correspond to Gd (002) and Pt (111) respectively. The strong peak at $2\theta = 30.89°$ indicates a preferred orientation of <002> direction (i.e. the c-axis of hcp; equivalent to <0001> direction) normal to the substrate plane. This result is similar to that observed previously in textured Gd thin films sputtered on either Si or glass substrate [57-58].

Fig. 3-4 shows the measured ZFC-FC curves for the textured Gd thin film. For the FC curve, a typical monotonically increasing magnetic moment is observed as the temperature is decreased. However, for the ZFC curve, an anomalous and prominent hump is observed. The hump has a maximum moment at a temperature of ~240 K. For similar measurements made on this thin film in the out-of-plane direction or for the polycrystalline bulk Gd sample (neither shown in the figure), the hump is absent. A similar "hump" is found in temperature dependent magnetocrystalline anisotropy measurements for single crystal Gd [59-60] as shown in the inset

of Fig. 3-4. In this inset, the change of angle θ between the easy axis and the c-axis is plotted as a function of temperature. In the temperature range between 165~225 K, the easy axis is perpendicular to the c-axis while outside this temperature range, the c-axis becomes the preferred easy direction (where $\theta < 90°$ is a.k.a. the canted spin arrangement [61]), i.e. spin-reorientation. The ZFC experimental hump measured on the textured Gd thin film shown in Fig. 3-4 is thus caused by the spin-reorientation associated with the temperature dependent magnetocrystalline anisotropy of Gd. Fig. 3-4 shows that the spin-reorientation starts at ~180 K and reverses at ~240 K different from that of the bulk Gd (i.e. the inset of Fig. 3-4). However, it is worth of noting that the temperature dependent magnetocrystalline anisotropies measured for bulk Gd vary in different publications [59-60, 62-64]. This observation may reflect that magnetocrystalline anisotropy is sensitive to the measurement technique as well as material conditions; for example, grain boundaries or thin film stresses.

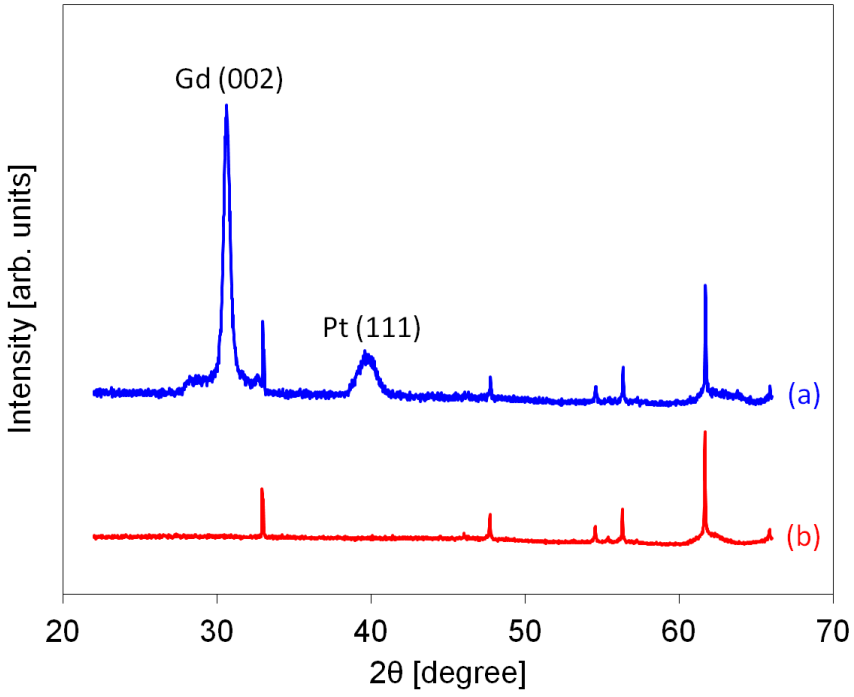

Figure 3-3: XRD patterns of (a) 25-nm-thick Gd thin film sputtered on Si substrate and (b) Si substrate.

It is important to point out that previous studies on 25-nm-thick epitaxial Gd thin film did not exhibit spin-reorientation [43-44], a result contradicting the findings presented in Fig. 3-4. Berger et al. [44] attributed the absence of spin-reorientation in epitaxial thin films to the strong in-plane shape anisotropy. However, the textured thin film reported in this study contains a large number of grain boundaries different from the epitaxial thin films reported by Berger et al. A study [50] has shown that the grain boundaries of Gd act as "defects" capable of disordering the magnetization uniformity in the nanoscale. The reported spin-misalignment length, a measure of the characteristic length of spin inhomogeneity [50], is ~5 nm for Gd with a grain size of 21±6 nm (i.e. similar to the thickness of textured Gd thin film). Therefore, the grain boundary defects are hypothesized to break up the long range spin order producing spin-reorientation in the 25-nm-thick textured Gd thin film observed in Fig. 3-4 but absent in epitaxial thin film.

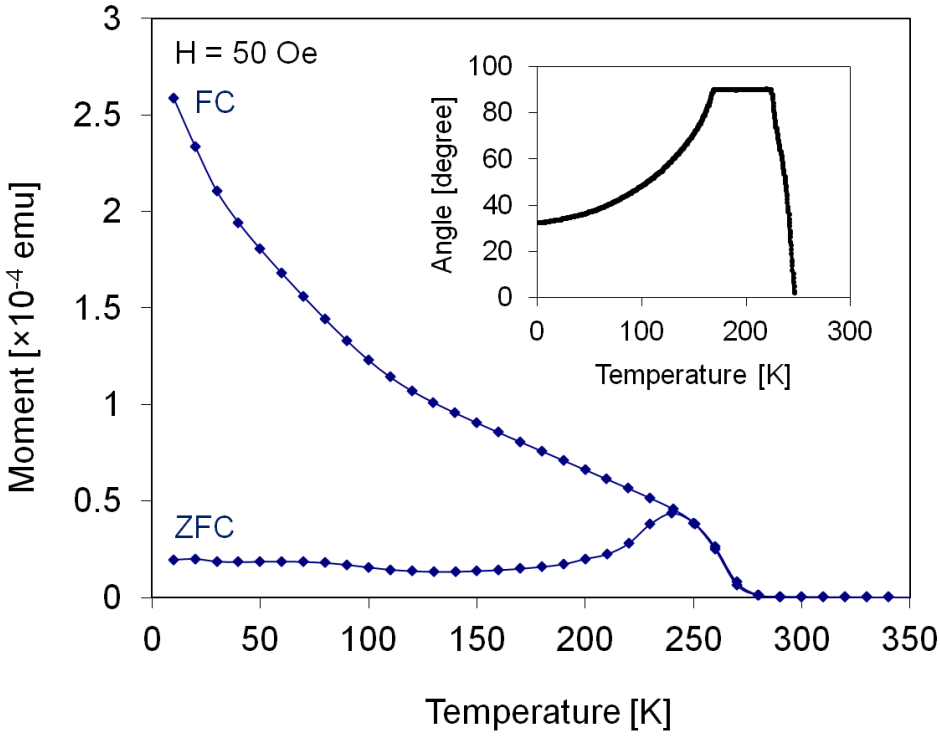

Figure 3-4: ZFC-FC curves of 25-nm-thick sputtered Gd thin film. The inset shows the angle between easy direction and c-axis as a function of temperature adopted from Graham [59].

Fig. 3-5 shows the isothermal magnetization curves of the textured Gd thin film. It was found that the saturation magnetization (M_s) measured at lower temperatures are similar to the values previously reported in the literature (e.g. see [39], M_s > 1800 emu/cm^3 at 50 kOe); however, this is not true for the values measured in the neighborhood of T_c. In addition, the magnetization changes as a function of applied field become more linear when the temperature reaches 283K, which is an indication of paramagnetic phase (i.e. susceptibility, χ = M/H, is a constant). These observation leads to a conclusion that T_c shifts to a lower temperature range (T_c = 287~294 K in typical [39]). This conclusion will be examined and discussed in the following paragraph using the Arrott plot.

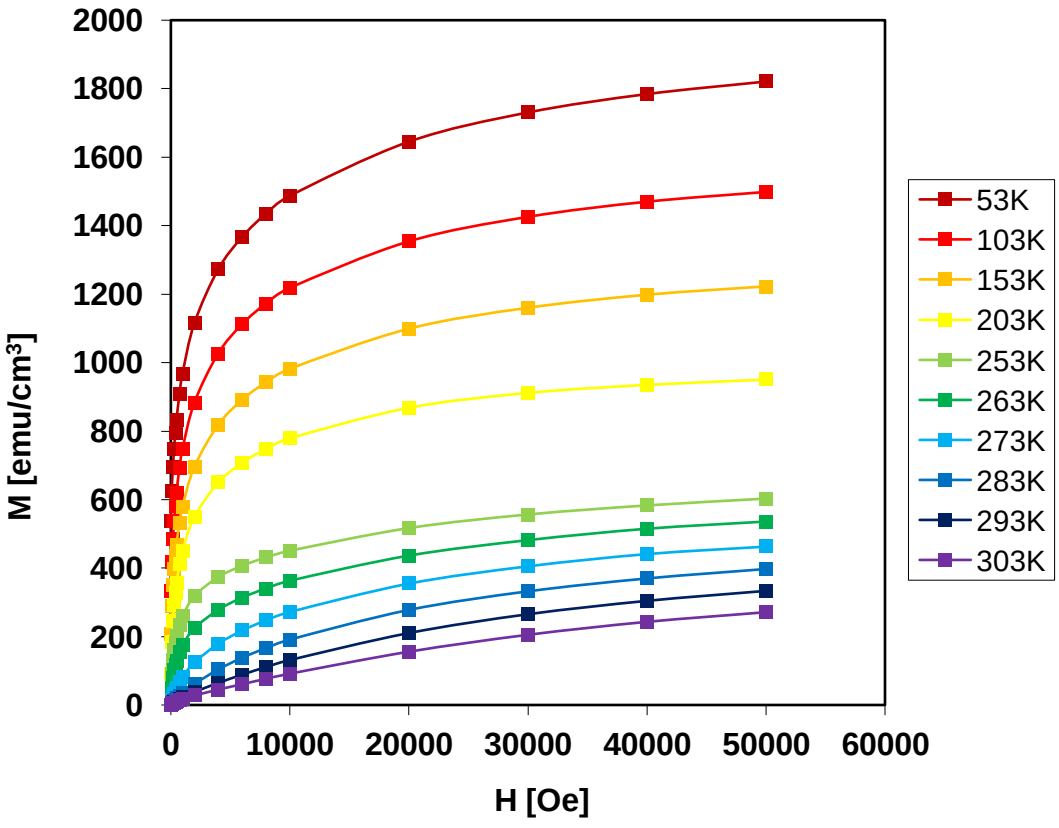

Figure 3-5: Isothermal magnetization curves of 25-nm-thick Gd thin film.

Fig. 3-6 shows the Arrott plot consisting of M^2 verse H/M values obtained from isothermal magnetization data on the textured Gd thin film (where M is the magnetic moment and H is the magnetic field). The curves are generated from measurements conducted at five different temperatures. T_c can be determined by extraploting the saturation slopes and finding the curve which intersects with the origin. The Arrott plot in Fig. 3-6 shows that the T_c of this Gd thin film is approximately 278 K, which represents a ~15 K shift below the T_c of bulk Gd measured from the E-beam evaporation source material. In the literature, T_c shifts were also observed on epitaxial [45] and sputtered [57] Gd thin film. Here, the observed T_c change in the sample is attributed to the internal thin film stress introduced during the UHV sputtering process.

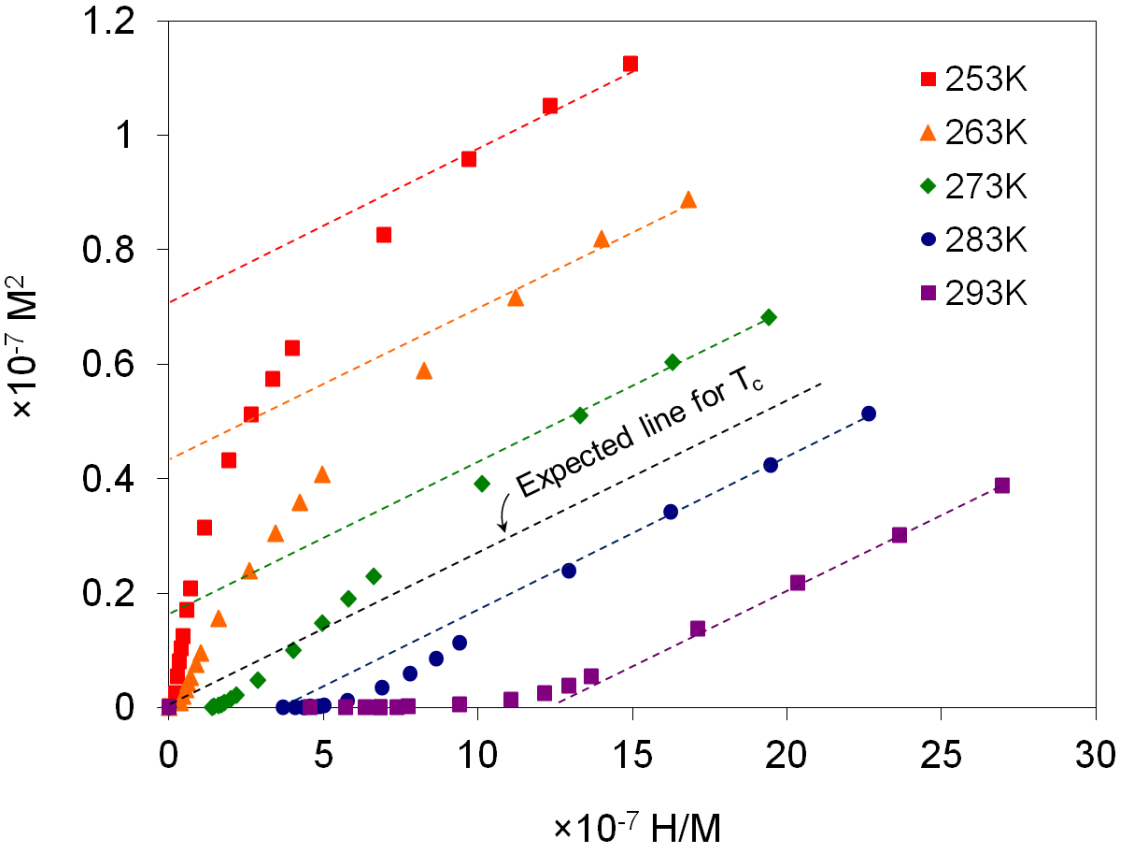

Figure 3-6: Arrott plot for 25-nm-thick Gd thin film.

Fig. 3-7 shows the AFM and MFM images of the textured Gd thin film at various temperatures from 253 to 293 K. In Fig. 3-7, each AFM image corresponds to the surface area of thin film where the MFM images were captured. The AFM images suggest that the contrasts shown in MFM images are not related to the surface topography of thin film. Since the MFM probe was magnetized along the tip axis and the tip was placed normal to the thin film surface during the imaging process, the observation of domains in the temperature range of 253-273 K agrees with our spin-reorientation findings, where the easy axis tends to align parallel to the c-axis (i.e. normal to the thin film surface) at temperatures above 240 K. In addition, the MFM images weaken considerably as the temperature increases from 273 to 283 K supporting the T_c determined from the Arrott plot as shown in Fig. 3-6.

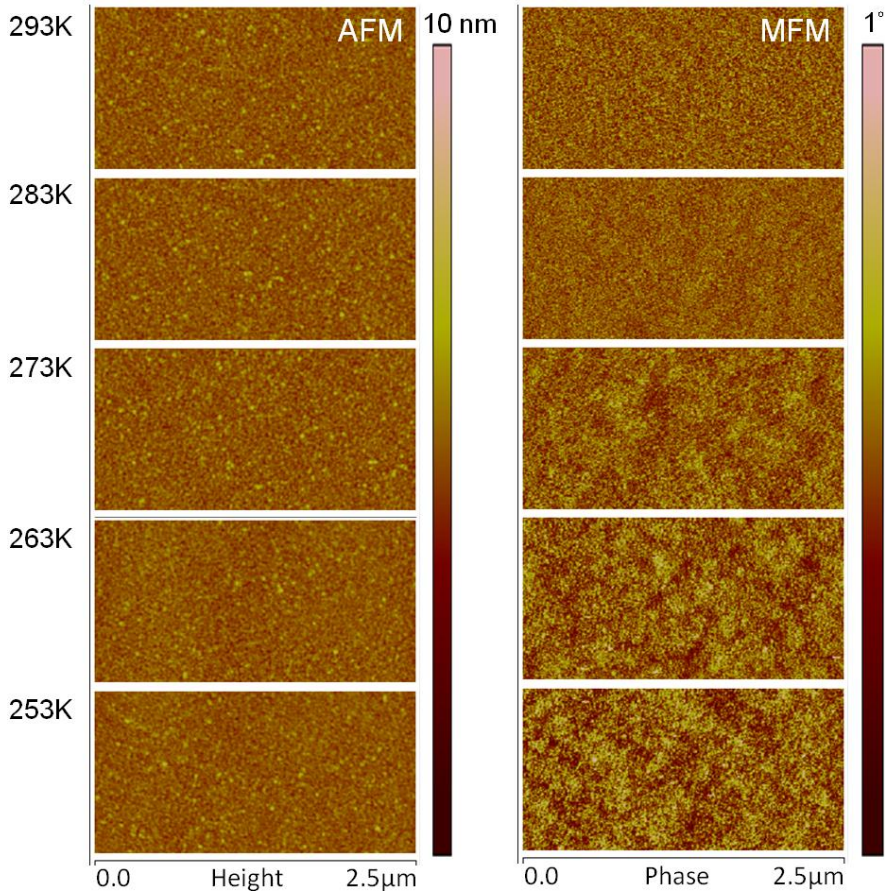

Figure 3-7: AFM and MFM images of 25-nm-thick Gd thin film.

3.4.2 Nanostructure

The isothermal magnetization curves measured for the Gd nanobar array are shown in Fig. 3-8 with a magnified view presented in the inset. Fig. 3-8 suggests that the Gd nanobars are saturated at an applied field of ~4000 Oe. The remanence and coercivity of the nanobars increases as the temperature decreases as can be seen in the inset of Fig. 3-8. At 53 K, the largest remanent magnetization of Gd nanobar measured is still less than 50% of saturation magnetization indicating an absence of single domain even though a strong shape anisotropy is present. Furthermore, the saturation magnetization (unit: emu/cm^3) of the Gd nanobars is substantially smaller than either thin film or bulk at any temperature measured. For example, the saturation magnetization of the textured Gd thin film (used in this study) measured at 53 K is larger than 1800 emu/cm^3 (see Fig. 3-5) while it is ~460 emu/cm^3 for the Gd nanobars as shown in Fig. 3-8. This result suggests that a significant portion of Gd nanobar structure is not ferromagnetic.

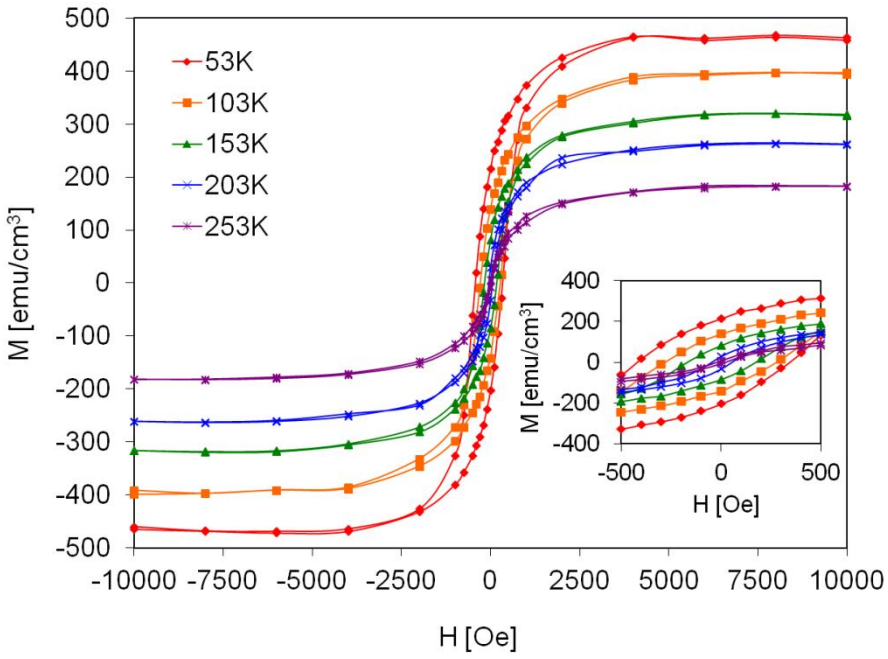

Figure 3-8: Isothermal magnetization curves of Gd nanobar array. Inset shows the remanences and coercive fields. The diamagnetic Si slope is subtracted.

TEM analysis was used to better understand the chemical and structural properties of the Gd nanobar. The TEM images of a Gd nanobar are shown in Fig. 3-9. The cross-sectional TEM image in Fig. 3-9a shows a volume loss of ~15% on the lateral sides of nanobar, which results in a trapezoidal shape of cross-section rather than the assumed rectangular cross-section (note that this volume loss was not included in magnetization calculation). EDS analysis of the nanobar also reveals that the weight percentage of oxygen on the lateral sides of nanobar is ~11%. Since the lateral sides were not capped with Pt, an oxidation layer is believed to have formed and peeled off [51] as evidenced by the debris shown by the arrow sign in Fig. 3-9a. These experimental results on Gd nanobar suggest that unless a durable passive layer exists, surface oxidation represents a potential problem to Gd nanostructure (~70 nm). Note that the volume loss caused by the trapezoid shape and oxidation is still insufficient to account for the ~75% reduction observed in the saturation magnetization as shown in Fig. 3-8.

The Gd nanobar diffraction pattern is shown in Fig. 3-9b. Since the TEM aperture size is larger than the cross-section of nanobar structure, the diffraction patterns of Si substrate, Pt capping layer, and the Pt alloy deposited during the TEM sample preparation process are also present in Fig. 3-9b (see arrow and circles). Based on this mixed diffraction pattern, identification of the Gd crystal structure was inconclusive [65]. This is due to the polycrystallinity of Gd nanobar as well as the presence of other crystal structures (i.e. Gd_2O_3 and fcc Gd). To resolve this problem, HRTEM images of the middle portion of the Gd nanobars were analyzed using FFT. The HRTEM images along with the indexed FFT pattern are shown in Fig. 3-9c~f. The measured d-spacing values along with the JCPDS-ICDD powder diffraction data are presented in Table 3-1. With errors less than 1%, both Gd hcp and Gd fcc structures were identified. Although not shown, the crystal structure of Gd_2O_3 could also be identified (with

errors smaller than 1% for multiple d-spacing values compared). It was determined that less than 50% of the crystal structure at the inner portions of the Gd nanobar corresponds to the ferromagnetic hcp structure. The reduction in hcp structure combined with the change in cross-section dimensions as well as oxidation accounts for the low saturation magnetization measured for Gd nanobars presented in Fig. 3-8.

Table 3-1: Miller indices and d-spacing of Gd

a. Crystal system: Cubic (fcc)

hkl	*d-spacing [nm] (FFT)	d-spacing [nm] **(#01-072-2223)	Error (%)
111	0.317	0.3181	0.346
200	0.276	0.2755	0.181
220	0.1939	0.1948	0.462
222	0.1606	0.1591	0.943
331	0.1242	0.1232	0.812

b. Crystal system: Hexagonal (hcp)

hkl	*d-spacing [nm] (FFT)	d-spacing [nm] **(#03-065-0372)	Error (%)
100	0.3148	0.3155	0.222
110	0.1815	0.1822	0.384
200	0.1564	0.1577	0.824

*Average measured value

**Ref. no. in JCPDS-ICDD powder diffraction file

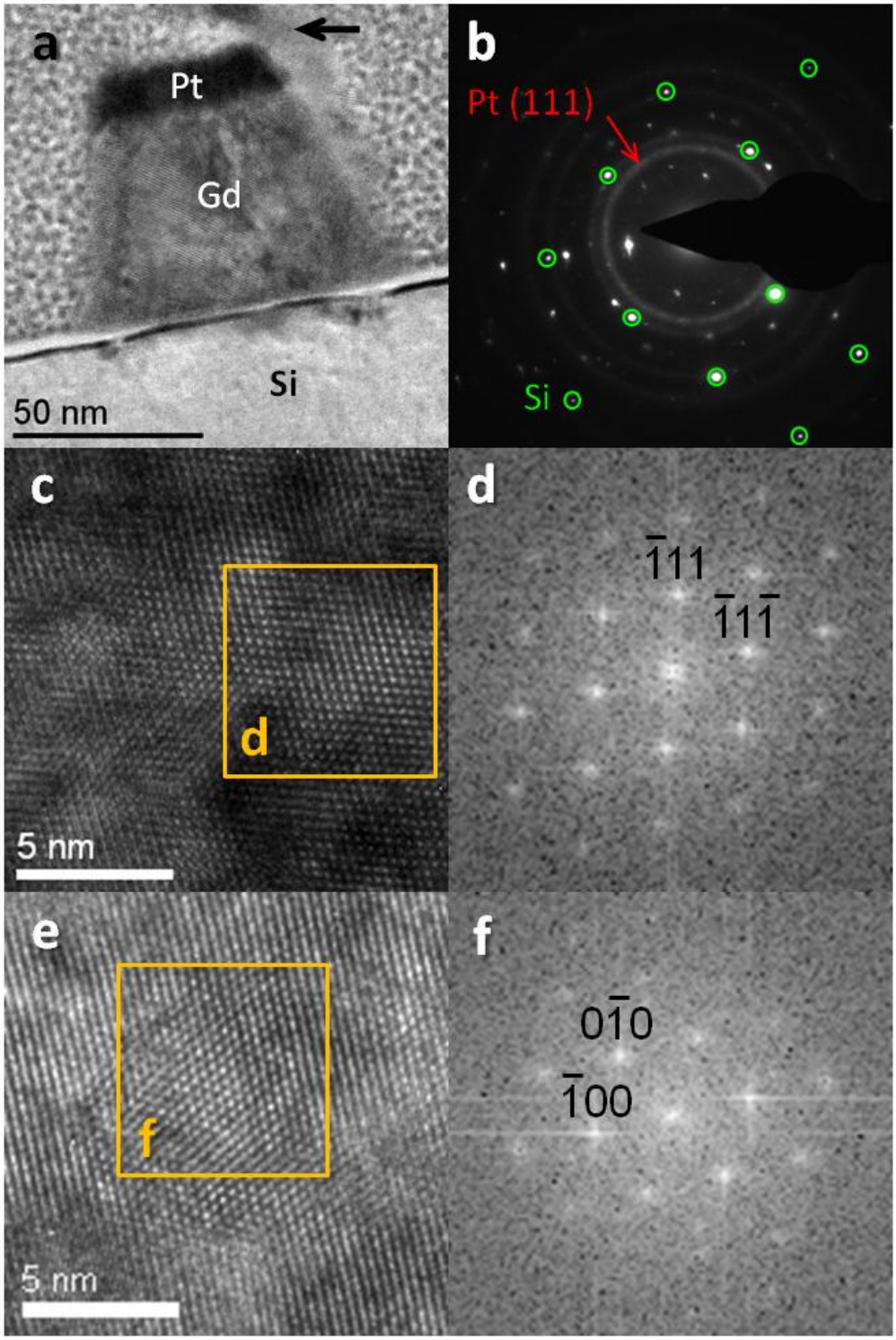

Figure 3-9: (a) TEM image of Gd nanobar cross-section (arrow indicates the possible peeled-off material); (b) Diffraction pattern of Gd nanobar cross-section; (c) HRTEM image of Gd nanobar; (d) Selected area FFT image (fcc, zone axis: [110]); (e) HRTEM image of Gd nanobar; (f) Selected area FFT image (hcp, zone axis: [002]).

Previous studies showed that a size-induced structural phase transformation from hcp to fcc occurs in Gd nanoparticles with a size ~ 10 nm [51-52]. However, since the fabricated Gd nanobar is relatively long (i.e. microns), it may be inappropriate to simply attribute the crystallinity change to physical size. Since a previous study has shown that Gd has a low stacking fault energy [66] and a high degree of stacking faults has been reported in nanocrystalline Gd thin film [67], it is speculated that stacking faults maybe responsible for the observed crystallinity change (i.e. fcc structure) reported in this paper. The stacking faults may arise due to large non-uniform stresses developed across the cross-section of Gd nanobar produced by the observed oxidation on the lateral surfaces. Note that a similar oxidation effect may occur around the edges of the textured Gd thin film; however, the oxidation region is negligible when compared to the thin film volume. For Gd nanostructures, since the Gd fcc phase is paramagnetic [52] and randomly occupies a significant portion of the total volume, it also leads to a substantial disruption in ferromagnetic exchange interaction contributing to the absence of single domain formation in the Gd nanobar. These results suggest that if the nanobars could be prevented from oxidation, a single domain may result.

3.5 Summary

An experimental observation of spin-reorientation in 25-nm-thick textured Gd thin film is reported in this chapter. The spin-reorientation is a typical phenomenon found in bulk Gd single crystal but not in epitaxial Gd thin film. The spin-reorientation in textured Gd thin film is related to grain boundary induced spin-disorder in the nanoscale. In addition, a reduction of T_c is also found in the textured Gd thin film. This finding agrees with the results reported previously on UHV or sputtered Gd thin film. The reduction of saturation magnetization along with the

absence of the shape anisotropy induced single domain in Gd nanobar was attributed to oxidation as well as the crystallinity change from hcp to fcc caused by stacking fault in the nanoscale. The results for both thin film and nanobar show that the crystallinity of Gd has a substantial impact on the magnetic anisotropy of Gd nanostructures.

CHAPTER 4

APPLICATION: THERMOMAGNETIC ENERGY HARVESTING

Chapter 4 presents an example of improving thermomangetic energy harvesting performance by using ferromagnetic single domain elements (i.e. by engineering the magnetic anisotropy). In this chapter, the theory of thermomagnetic generation is reviewed and an efficiency analysis using experimentally measured magneto-thermal properties of 3d transitional and 4f rare earth ferromagnetic elements is presented. For the typical thermomagnetic generation, theoretical results suggest that 55% of Carnot efficiency is possible; however, experimental data indicates values smaller than 25% of Carnot efficiency unless large magnetic field, e.g. $H_{app} \sim 80$ kOe, is applied. Analytical results present in this chapter show that for smaller magnetic fields representative of NdFeB permanent magnets (e.g. $H_{app} = 3$ kOe), the largest efficiencies are obtained for operating ferromagnetic materials over a smaller temperature difference ($\Delta T = 5$ K). Furthermore, single crystal materials are found to have superior efficiencies as do elements that undergo an order-to-order phase transition. Both of these later results relate to increased magnetization changes over a given ΔT. These results are subsequently used to postulate that a single domain structure will produce larger efficiencies due to the higher magnetization present over a wide range of magnetic fields when compared to multi-domain materials. Calculations for a Gd single domain suggest efficiencies on the order of 30% are possible representing a threefold increase from multi-domain Gd at relatively small magnetic fields.

4.1 Background

While thermal energy is one of the most ubiquitous forms of waste energy available, a thermal energy harvesting system with high efficiency does not currently exist. Over the last century, there has been a great deal of research conducted on thermoelectric devices, such as the Seebeck effect [68]. Many of these efforts focused on increasing the thermoelectric figure of merit to improve efficiency; however, the maximum relative efficiency (i.e. the percent of Carnot efficiency) reported [68] is in the range of 10-20%. Another approach to convert thermal energy into electrical energy is thermomagnetic generation, but this area has received comparatively little attention. Thermomagnetic devices convert thermal energy into magnetic energy and subsequently into electrical energy. The first analytic study on thermomagnetic generation proposed by Brillouin and Iskenderian [69] in 1948 suggest a maximum relative efficiencies of 55% (i.e. three to five times higher than thermoelectric generation); however, there is a lack of experimental evidence to directly support or contradict this analysis nor have there been sufficient efforts to explore alternative thermomagentic concepts.

The concept of thermomagnetic generation (see Fig. 4-1) involves a ferromagnetic material thermally cycled about its Curie temperature (T_c) inside a magnetic circuit. Temperature oscillations about T_c produces a time variant magnetic flux (i.e. function of temperature), which drives an electrical currents when operating within a solenoid. In the 1950's [37, 70], conventional ferromagnetic materials like cobalt (Co), iron (Fe), nickel (Ni) and their alloys were considered for thermomagnetic generation, but due to the lack of sufficiently strong magnets at this time, the efficiency level reported was very low. The relatively large T_c for these conventional ferromagnetic materials also prevented additional studies from moving forward. In 1959, studies on gadolinium (Gd) with a T_c near room temperature was proposed by Elliot [35].

Again, the limited availability of strong magnets restricted the power output. In 1965, a room temperature T_c manganese-copper ferrite was studied by Murakami [71], but the efficiency of this material was not reported. In 1967, an analytical model using resonating magnetic field was proposed by Rosengsweig [72] with calculations suggesting that a large magnetic field is required to obtain high efficiencies.

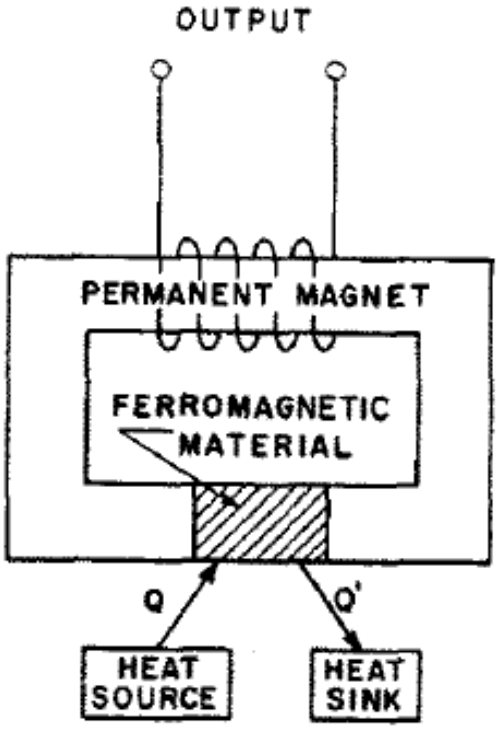

Figure 4-1: Concept of a thermomagnetic generator [73]. A ferro-to-paramagnetic phase change across T_c in a ferromagnetic material produces a time variant magnetic flux which further induces an electrical current output.

After two decades of dormancy, Kriol and Mills [73] studied regenerative thermomagnetic cycles using Fe , Gd, and $Ho_{69}Fe_{31}$ (T_c at high, ambient, and cryogenic temperature respectively) and analytically calculated efficiencies 75% of Carnot in 1984. The concept of regeneration was subsequently studied by Solomon [36, 74] using a superconducting solenoid in 1988 and 1991. In Solomon's design, the composition of $Y_2(Fe_xCo_{1-x})_{17}$ alloy could be

varied to permit thermomagnetic energy harvesting over a wider temperature span using cascading structures (i.e. regenerative cycles). In 2007, Ujihara et al. [40] fabricated and tested a thermomagnetic energy harvesting device focused on small (millimeter) scale structures using piezoelectric elements to convert the magnetic energy into electrical energy rather than solenoids (see Fig. 4-2). Here, Ujihara's focus was not on increasing efficiency, but on increasing the oscillation frequency about T_c to increase power.

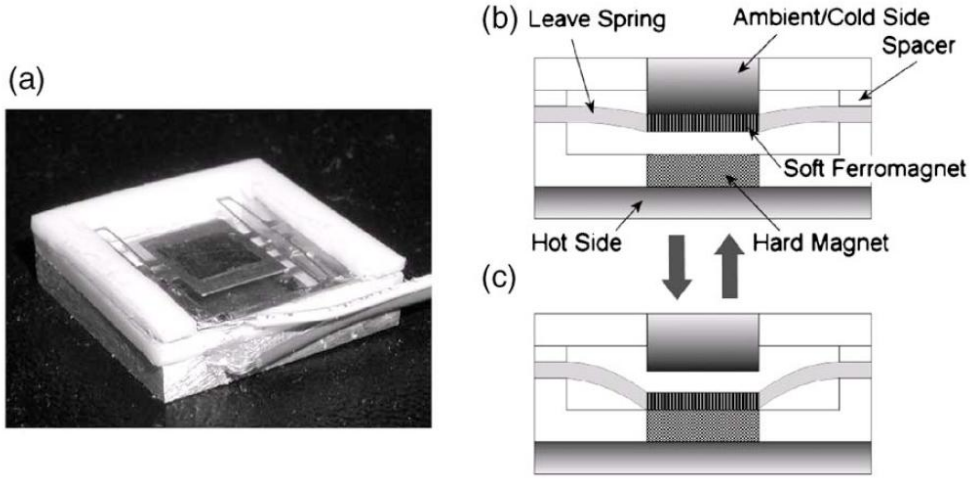

Figure 4-2: Thermomagnetic energy harvesting device using piezoelectric elements to convert magnetic energy into electrical energy [40]: (a) Actual device, (b) Cross-section during cooling, and (c) Cross-section during heating. Leave spring is the piezoelectric element.

The above papers represent a summary of studies conducted in the area of thermomagnetic generation. One related area is pyromagnetic generation [75-76] to potentially convert thermal to electrical energy. The pyromagnetic effect represents the change of magnetization as a function of temperature at $T < T_c$. In general, pyromagnetic energy harvesting efficiency is substantially smaller than the thermomagnetic systems previously described. There are also other studies in related areas such as thermomagnetic engine [77], magnetothermal engine [78], Curie wheel [79], and magnetic power generation with fluids [80] which typically

use the thermal to magnetic energy conversion for propulsion concepts which are similar in context.

While analytical reports of 55% to 75% of Carnot efficiency have been suggested in the literature, experimental data supporting this is still absent. In this chapter, a theoretical model is reviewed for calculating thermomagnetic generation efficiency with an exclusive focus on the thermal to magnetic energy conversion. The analytical portion is followed by an evaluation of the efficiencies of a number of ferromagnetic elements. The performance of ferromagnetic elements in terms of thermomagnetic efficiency is compared and discussed with results indicating that they are significantly below theoretical predictions of 55%. Finally, a ferromagnetic single domain approach which will increase the thermomagnetic conversion efficiencies closer to those reported analytically is suggested.

4.2 Thermomagnetic Cycle

An idealized thermomagnetic cycle is illustrated in Fig. 4-3 along with a plot of magnetization as a function of magnetic field (M-H plot) for two different temperatures (i.e. T_{cold} and T_{hot}). The four illustrations shown in Fig. 4-3 contain a magnetic flux source "magnet" to create the magnetic field, a "cold" heat sink, a "hot" heat source, and a material which is either ferromagnetic at $T = T_{cold}$ or non-ferromagnetic at $T = T_{hot}$. The processes shown in Fig. 4-3 can be described as follows: Initially at point 1, the temperature of the material is above T_c (at T_{hot}) and is thus non-ferromagnetic. By bringing the material into thermal contact with a cold reservoir, the temperature drops to T_{cold} ($T_{cold} < T_c$) and the ferromagnetic material becomes ferromagnetic at point 2. During this process, the material is subjected to a magnetic field which increases the magnetization of the material to point 3 as shown in the M-H plot. At this same

time, the material is brought into thermal contact with the hot reservoir, and therefore, the temperature again increases to T_{hot} at point 4 and the material becomes non-ferromagnetic returning to the cold side (point 1) and thus completing the cycle.

When a material is magnetized and demagnetized as illustrated in Fig. 4-3, the maximum available energy can be calculated by using the area method [26]. The same principal is used to analyze a thermomagnetic cycle here, but the difference is that the magnetization and demagnetization process in a thermomagnetic cycle involves an additional heat exchange process. In a thermomagnetic cycle, the net magnetic energy available, W_{out}, from a ferromagnetic material is defined [74] by the area enclosed (i.e. the bounded area 1234 in Fig. 4-3) and is mathematically expressed as (in cgs unit: erg/cm^3):

$$W_{out} = -\frac{1}{4\pi}\oint_{cycle} HdB = -\frac{1}{4\pi}\oint_{cycle}(HdH + 4\pi HdM(T,H)) \quad (1)$$

where B is magnetic induction, H is magnetic field, and M is magnetization. Since the integral of the HdH term is zero in a complete cycle, Equation 1 reduces to:

$$W_{out} = -\oint_{cycle} HdM(T,H) \quad (2)$$

By following the first law of thermodynamics (i.e. energy conservation), the heat input in a thermomagnetic cycle is defined [74] as follows:

$$Q_{in} = Q_{out} + W_{out} = \rho\int_{T_{cold}}^{T_{hot}} C_p(T)dT + T\int dS_m + W_{out} \cong \rho\int_{T_{cold}}^{T_{hot}} C_p(T)dT \quad (3)$$

where ρ is the density, C_p is the specific heat for the material, S_m is the magnetic entropy. For relatively small H, the integral of C_p term is much larger than the other two terms and thus the equation can be further simplified as shown in Equation 3 (see discussion in results section). The absolute efficiency (i.e. the device efficiency), η_{abs}, in one cycle is then defined as the ratio of the energy produced (i.e. the net magnetic energy available) to the heat input into the system [69, 74]:

$$\eta_{abs} = \frac{|W_{out}|}{Q_{in}} = \frac{\oint_{cycle} HdM(T,H)}{\rho\int_{T_{cold}}^{T_{hot}} C_p(T)dT + T\int dS_m + \oint_{cycle} HdM(T,H)} \cong \frac{\oint_{cycle} HdM(T,H)}{\rho\int_{T_{cold}}^{T_{hot}} C_p(T)dT} \quad (4)$$

η_{abs} can be compared to the efficiency of a Carnot cycle (η_{Carnot}) operating between the same two temperatures where η_{Carnot} represents the maximum efficiency of any heat engine and is a function of only T_{hot} and T_{cold}. The relative efficiency (% of Carnot), η_{rel}, may now be defined as

$$\eta_{rel} = \frac{\eta_{abs}}{1-\frac{T_{cold}}{T_{hot}}} = \frac{\eta_{abs}}{\frac{\Delta T}{T_{hot}}} = \frac{\eta_{abs}}{\eta_{Carnot}} \quad (5)$$

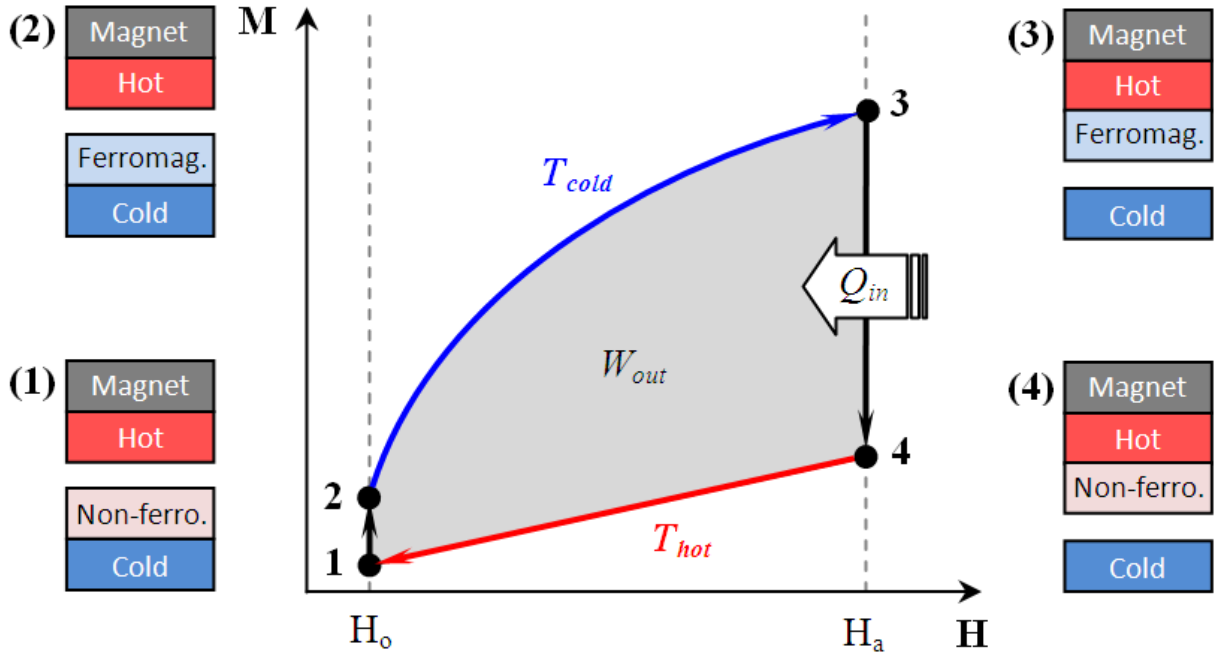

Figure 4-3: Isothermal magnetization curves and thermomagnetic cycle. The magnetic state of ferromagnetic material and the heat transfer processes with two thermal reservoirs are shown in schematic diagrams.

4.3 Analysis

The analysis presented in the previous section can be used along with experimental data available in the literature to determine relative efficiency η_{rel} for a wide range of ferromagnetic materials to assess the efficiency of thermomagnetic generation compared to other approaches. Consider an example, wherein polycrystalline Gd is the working body. Fig. 4-4 shows the M-H plot for a ~1 mm^3 polycrystalline Gd sample (99.9% purity from Kurt J. Lesker Company). The isothermal magnetization curves shown in Fig. 4-4 were measured at six different temperatures using SQUID (Superconducting Quantum Interference Device from Quantum Design). As discussed in the previous chapter, reported T_c values for Gd range from 287-295 K (varied in publications) [39] and is dependent on experimental technique and the definition used (i.e. rather than variations with material characteristics). By using the Arrott plot [56] technique, T_c was found to be approximately 288K for this polycrystalline Gd sample.

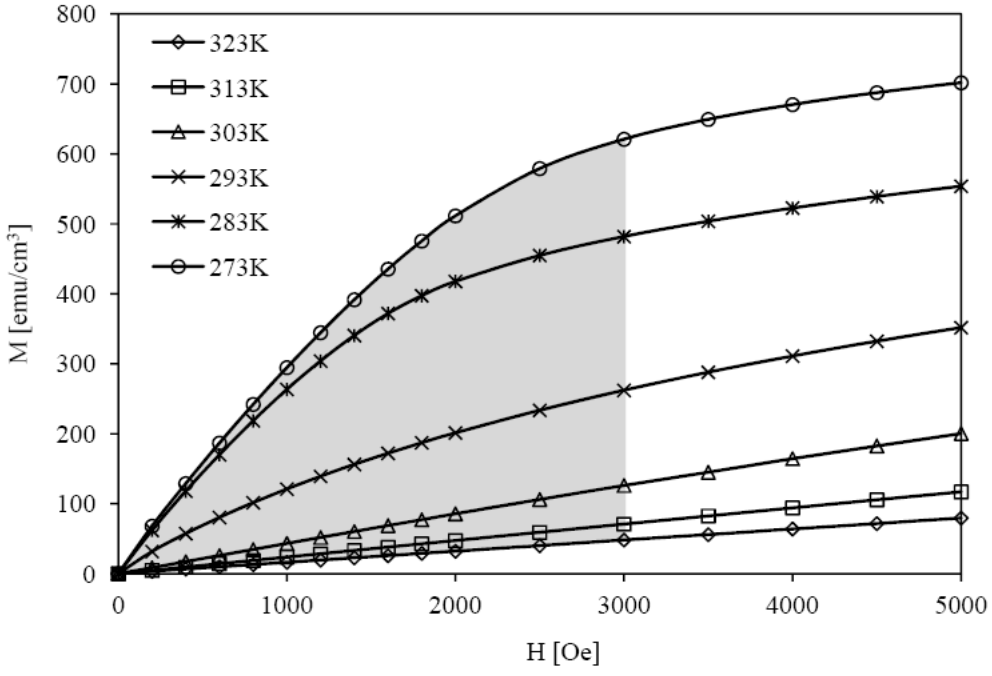

Figure 4-4: Isothermal magnetization curves of polycrystalline Gd. The gray area represents the net available magnetic energy (W_{out}) in a thermomagnetic cycle defined by Equation 2 (for T_{cold} = 273 K, ΔT = 50 K, and H_{app} = 3000 Oe).

Calculations of Gd's thermomagnetic efficiencies are illustrated for a temperature difference of $\Delta T = 50$ K, with $T_{cold} = 273$ K (i.e. $T_{hot} = 323$ K). The applied magnetic field (H_{app}) chosen for this calculation is 3000 Oe which is comparable to the field level of an NdFeB permanent magnet at its surface. This field level is relatively small and thus the approximation present in Equation 4 is used for the calculation (with errors < 1%). As shown in Fig. 4-4, when Gd is at $T_{cold} = 273$ K, with the applied field $H_{app} = 3000$ Oe, the magnetization $M_{cold} = 620$ Oe. As the Gd is heated to $T_{hot} = 323$ K the magnetization at the same H_{app} drops to $M_{hot} = 48$ Oe. Using Equation 2 and integrating around the thermomagnetic cycle, the net magnetic energy (W_{out}) per unit volume for this cycle is 1.06×10^{6} erg/cm^3. The heat input (Q_{in}) required in this cycle can be calculated using a C_p-T plot. Fig. 4-5 shows a C_p-T plot of the polycrystalline Gd used in this study and measured with DSC (Differential Scanning Calorimeter from PerkinElmer). C_p is known to be a function of temperature and it behaves abnormally near the temperature where the magnetic phase transformation occurs (i.e. a maximum value of C_p appears in the vicinity of T_c). By integrating $C_p(T)$ over the temperature span from $T_{cold} = 273$ K to $T_{hot} = 323$ K as defined by Equation 3, Q_{in} is found to be 1.09×10^{9} erg/cm^3. Therefore, for this particular thermomagnetic cycle, the absolute efficiency is $\eta_{abs} = 0.097\%$ which corresponds to a relative efficiency of $\eta_{rel} = 0.63\%$ when compared to the Carnot limit. This process illustrates how the efficiencies of a wide range of materials may be calculated.

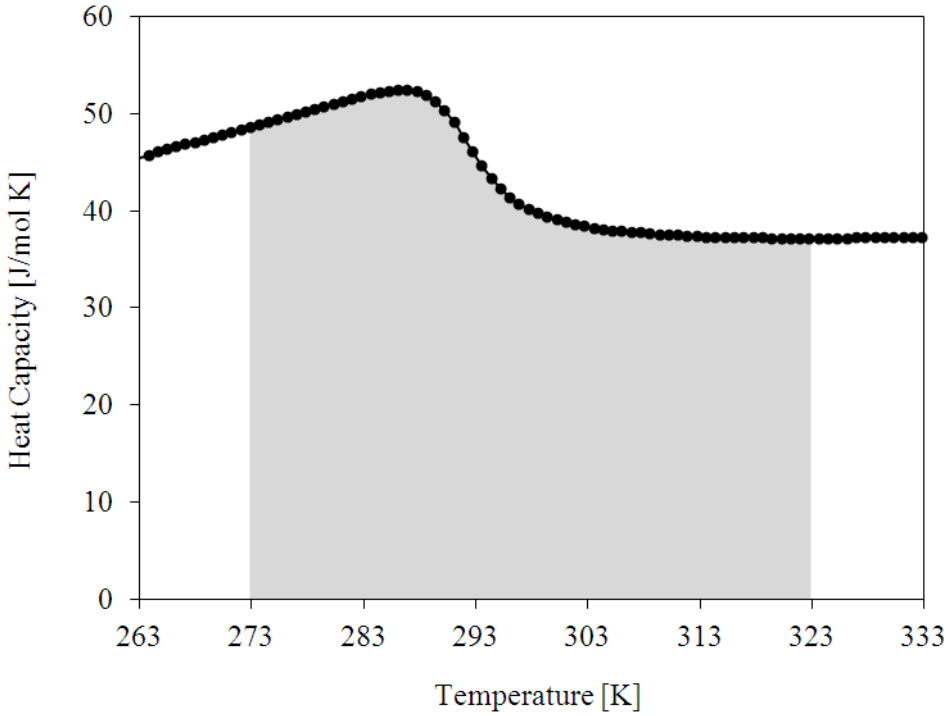

Figure 4-5: Heat capacity of polycrystalline Gd as a function of temperature. The gray area represents the heat input (Q_{in}) in a thermomagnetic cycle defined by Equation 3 (for T_{cold} = 273 K and ΔT = 50 K).

The relative efficiency η_{rel} can also be calculated for larger values of H_{app} (e.g. generated by superconducting coils [36, 74]). However, the efficiency at high magnetic fields requires inclusion of magnetic entropy S_m and W_{out} terms into Q_{in} (see Equation 3). Fig. 4-6 shows a plot of η_{rel} (see Equation 5) calculated without the approximation as well as the three components in Q_{in} (i.e. the integral of $T dS_m$ and $C_p dT$, and W_{out}) as a function of applied magnetic field for a thermomagnetic cycle of T_{cold} = 290 K and ΔT = 10 K. In Fig. 4-6, the data points for H_{app} = 20, 50, and 80 kOe are obtained from Solomon [74] while the data points for H_{app} = 3 kOe are calculated based on the results presented in Fig. 4-4 and Fig. 4-5. Fig. 4-6 shows that η_{rel} increases substantially from a low value of 4.7% to 53.5% as H_{app} increases. This clearly indicates that larger magnetic fields produce higher efficiencies as suggested in the literature [36, 72, 74]. Fig. 4-6 also shows that the S_m component as well as W_{out} is negligible in Q_{in} at lower

magnetic fields (i.e. H_{app} < 20 kOe). In this study, a relatively low magnetic field, H_{app} = 3 kOe, was chosen to compare materials based on available hard magnetic materials (i.e. H_{app} = 3 kOe is approximately the maximum available). However, it should be noted that larger efficiencies are possible by applying larger H_{app}, but producing large H_{app} could also degrade efficiencies because a magnetic source typically requires power.

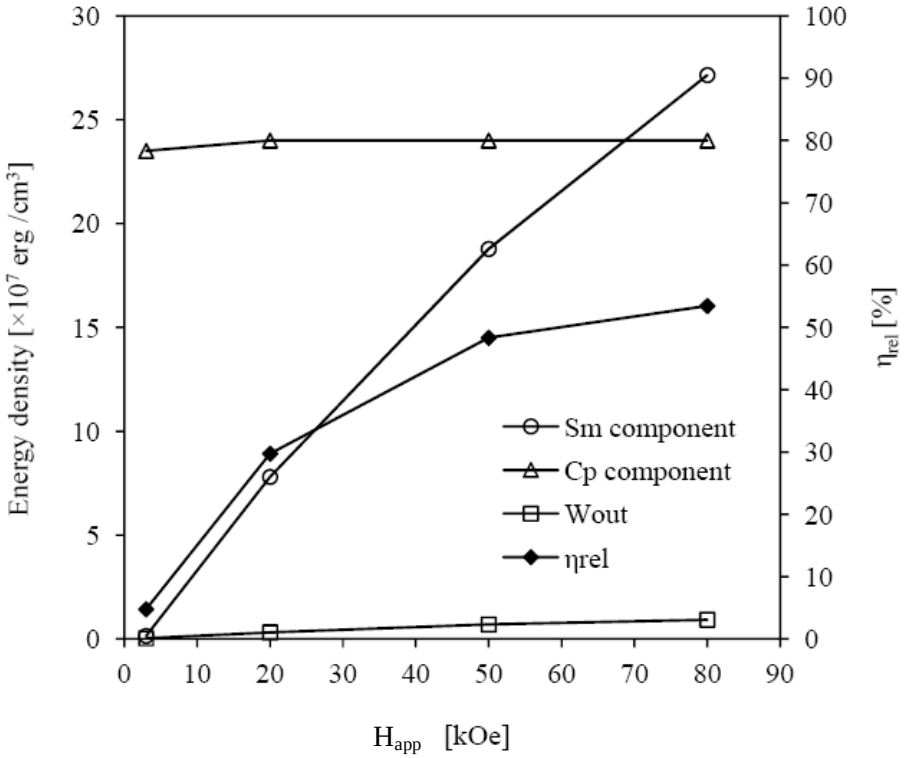

Figure 4-6: Heat input components at various applied fields.

Efficiencies can now be calculated for Gd operating at different temperature ranges and some results are shown in Fig. 4-7. Fig. 4-7 shows the variation of η_{rel} as a function of ΔT calculated for six different T_{cold} (i.e. 273, 278, 283, 288, 293, and 298 K). The results show that a large ΔT reduces η_{rel}, regardless of T_{cold}, and thus, the highest η_{rel} is found for the smallest ΔT. Therefore, minimizing the thermal excursion generally maximizes the efficiency for the

thermomagnetic energy harvesting. For a $\Delta T = 5$ K, the highest efficiency is for $T_{cold} = 288$ K rather than one of the extreme temperatures (i.e. 273 or 298 K). The reason for this optimum is that the magnetization changes the most dramatically at 288 K for the given $\Delta T = 5$ K. That is, for colder termperatures ($T_{cold} < 288$ K), the material is ferromagnetic and the change in magnetization for a $\Delta T = 5$ K is relatively small which provides a relatively small work output. Likewise for higher temperatures ($T_{cold} > 288$ K), the material is paramagnetic and once again the magnetization change as well as the output work for $\Delta T = 5$ K is small. This result can also be explained by the temperature dependence of spontaneous magnetization predicted by Weiss theory using Brillouin function [26] where the sharpest change of magnetization happens at the temperature closer to T_c (i.e. the slope $\Delta M/\Delta T \rightarrow \infty$ at T_c) and thus the largest work output per ΔT should be near T_c.

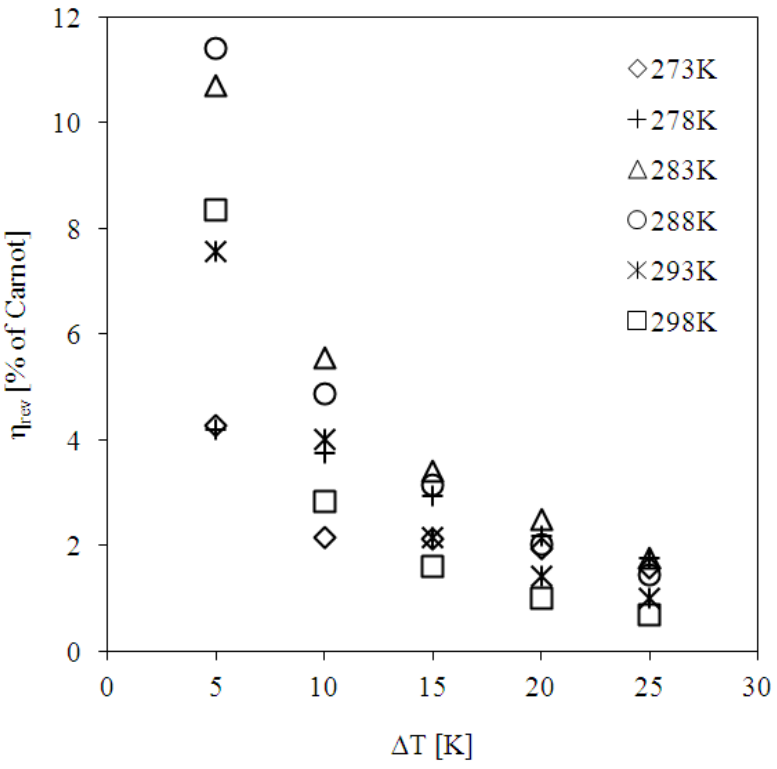

Figure 4-7: Relative efficiency of a thermomagnetic generator using polycrystalline Gd (H_{app} = 3000 Oe). The temperature of each entry represents T_{cold}.

Based on the results shown in Fig. 4-7, η_{rel} for a wide range of ferromagnetic materials are further evaluated. Table 4-1 shows η_{rel} as well as the corresponding η_{Carnot} calculated for eight ferromagnetic elements (Co, Fe, Ni, Gd, Tb, Dy, Ho, and Er) in a thermomagnetic cycle based on $\Delta T = 5$ and $H_{app} = 3000$ Oe as described previously. These elements are arranged in the table from the highest to lowest T_c. For each element, we compared the efficiencies considering two cases either $T_{cold} = T_c$ or $T_{cold} = T_c - \Delta T$, and presented the case having larger η_{rel}. The fifth column reflects which case is presented. Among the elements analyzed, Co, Fe, and Ni are 3d transitional elements (which have incomplete 3d electron shells) and the remainder are rare earth elements (which have incomplete 4f electron shells) [61]. Furthermore, Gd is the only element which has a T_c in the range of room temperature. All of the elements studied are ferromagnetic below T_c, but not all of them are paramagnetic above T_c. Here, Tb, Dy, Ho, and Er have ferro-to-antiferromagnetic phase transition across T_c as shown in the third column.

In Table 4-1, all the data used including T_c, M_{cold}, and the peak C_p values were obtained from experimental data reported in the literature (except for Gd shown in Fig. 4-4 and Fig. 4-5). For elements with experimental data available, the η_{rel} was calculated for both single and polycrystalline structures. For single crystal materials, the isothermal magnetization curves were measured along the easy axis of the material. In general, for both single and polycrystalline cases, interpolations were used to obtain isothermal magnetization curves for the different temperatures used in the efficiency calculations. Any error introduced due to interpolation should not significantly alter the calculated η_{rel}. However, significant discrepancies were found to exist in the isothermal magnetization curves of single crystal Er measured along the easy axis. Feron (see Coqblin [81]) showed that single crystal Er can be fully saturated at fields as small as ~1 kOe at 20 K while Gama and Foglio [82] showed that 15 kOe is required to saturate single crystal Er at

the same temperature. In Table 4-1, two sets of η_{rel} for single crystal Er are presented based on both of these experimental data [81-82]. As for polycrystalline Er, the M-H data are more consistent [83-84]; however, only limited isothermal magnetization data are available in the literature..

Table 4-1: Magneto-thermal properties and efficiencies of ferromagnetic materials

Elements	T_c [K]	Magnetic phase transition	Crystal Structures	M_{cold}[b] [emu/cm^3] (T_{cold} [K], H_{app} [Oe])	Max.[c] C_p [J/mol.K]	η_{Carnot} [%]	η_{rel}[a] [%]	Ref.
Co	1394	F-P[e]	Poly	139 (1389, 3000[d])	54.2	0.36	2	[85-86]
Fe	1044	F-P	Poly	288 (1039, 3000[d])	72.5	0.49	3.4	[87-88]
Ni	630	F-P	Poly	76 (630, 3000)	42.5	0.79	3.4	[87, 89]
Gd	288	F-P	Poly	375 (288, 3000)	52.4	1.71	11.4	[39]
	294		Single	422 (294, 3000)	59	1.67	20.5	
Tb	221	F-A[f]	Poly	1176 (221, 3000)	148	2.21	17.5	[90-92]
			Single	1180 (221, 3000)			18.1	
Dy	89	F-A	Poly	1028 (89, 3000)	70.8	5.32	7.5	[93-95]
			Single	2540 (89, 3000)			23.5	
Ho	20	F-A	Poly	1594 (15, 3000)	16.5	25	16.2	[96-98]
			Single	2816 (15, 3000)			57	
Er	20	F-A	Poly	678 (20, 3000)	20.8	20	3.5[g]	[81-84, 99]
			Single	2430 (20, 3000)			65.1[h]	

a. H_{app} = 3 kOe and ΔT = 5 are assumed for all the calculations. Optimistic isothermal magnetization data were chosen from interpolation.
b. For single crystal, only the magnetizations along the easy axis were considered.
c. $C_p(T)$ anomaly appeared in the vicinity of T_c
d. M_{cold} at 3000Oe was calculated from linear interpolation.
e. Ferromagnetic to paramagnetic transition at T_c
f. Ferromagnetic to antiferromagnetic transition at T_c
g. Calculated based on interpolation using limited isothermal magnetization data for polycrystalline Er.
h. η_{rel} = 3.4% if using the isothermal magnetization data shown by Gama and Foglio [82].

Additional comments concerning the construction of Table 4-1 are warranted. First, for Q_{in} calculations, the same C_p-T plot was used for both single and polycrystalline structures. It was previously reported [39] that the C_p as a function of temperature shows insignificant

differences between single and polycrystalline structures. Second, the η_{Carnot} of each element is also displayed in the table as well. The increase of η_{Carnot} observed in the table as T_c decreases corresponds to the definition of η_{Carnot} (see Equation 5), which suggests that the total thermal efficiency of a thermomagnetic device is superior in cryogenic environments, a comment that is true for all heat engines. Third and finally, the calculations for W_{out} in this study neglected magnetic hysteresis effects. Only the H increasing section of the isothermal magnetization curves were used (i.e. as contrasted with H decreasing). In general, hysteresis may arise in the rare earth elements (e.g. see Rhodes [96]) which have a ferro-to-antiferromagnetic phase transition. However, if this hysteresis is accounted for in calculations, it may result in a net increase in η_{rel} due to the increased W_{out} produced by a larger remanence (M_r) in H decreasing curves as compared to H increasing curves. Therefore, the data presented in Table 4-1 for rare earth elements (Dy, Er, Ho, and Tb) may be a conservative estimate of efficiency.

4.4 Discussion

As can be seen in Table 4-1, 3d elements generally have a lower η_{rel} then rare earth elements. Our results show that polycrystalline Co, Fe, and Ni (and maybe Er) have a $\eta_{rel} < 5\%$ while polycrystalline Gd, Tb, Dy, and Ho have more than twice that value (η_{rel} = 7.5-17.5%). While not shown in the table, the 3d elements can also achieve similar efficiencies as the rare earth elements if the magnetic field is increased. For example, if Fe is operated with H_{app} = 5 kOe, an increase of η_{rel} = 10% is reached; while for Co, an applied field of 7 kOe produces an increased η_{rel} = 11%. These results, which correspond to the results shown in Fig. 4-6, help explain the obstacles reported in the early development of thermomagnetic generation in the 1950s. That is, researchers could not find magnets capable of generating sufficient fields to

saturate the ferromagnetic materials and thus could not produce high power outputs. However, one thing worth noting is that increases of η_{rel} as H_{app} increases may be limited for materials that have an antiferromagnetic state above T_c (e.g. rare earth elements). This is because these materials are typically saturated at relatively small magnetic fields in the antiferromagnetic state as compared to materials in the paramagnetic state. The saturation in the antiferromagnetic state also saturates W_{out}, and therefore, maximizes η_{rel} at lower H_{app} values.

Additionally, single crystalline elements typically have a higher η_{rel} than polycrystalline elements for the same thermomagnetic cycle. For example, η_{rel} of polycrystalline Gd is 11.4% while for single crystal it is 20.5%. This observation is a result of a larger magnetization value (i.e. a higher susceptibility) for a single crystalline ferromagnetic material, when the field is applied along the easy axis, as compared to a polycrystal at the same applied field. The larger magnetization value present in single crystalline materials is attributed to magnetocrystalline anisotropy which reduces the energy barrier when a magnetic field is applied in the easy direction, and therefore, the spins can be aligned more easily along this direction. In a thermomagnetic cycle, increasing M_{cold} directly increases W_{out} (i.e. the bounded area in the M-H plot), and thus increases efficiency for single crystal materials aligned along their easy axis.

As noted previously, the rare earth elements (Gd, Dy, Ho, and Tb) produce substantially higher η_{rel} for the chosen thermomagnetic cycle compared with 3d elements (note that Er is an outlier as mentioned before). Here, Dy, Ho, and Tb transform from a ferromagnetic to antiferromagnetic phase at T_c and this transition is an order-to-order phase transformation. In sharp contrast, the 3d elements undergo an order-to-disorder phase transformation (i.e. ferromagnetic to paramagnetic). The increased efficiency in order-to-order transition suggested by Table 4-1 is partially due to the lower T_c of rare earth elements producing a larger M_{cold} when

compared to the M_{cold} of 3d elements. However, an important additional distinction for order-to-order transitions is that the change in magnetization (M_{cold}/M_{hot}) is much larger than order-to-disorder transitions. For example, for the thermomagnetic cycle used in this study, it was observed that the magnetization of Gd (order-to-disorder phase transformation) decreased by ~36% from T_{cold} to T_{hot}; whereas rare earth elements with order-to-order phase transformation decreased by ~60% for the same ΔT. Therefore, one explanation for the increased η_{rel} in order-to-order phase transformations is that a relatively larger amount of magnetic energy is lost to entropy during the transition to a disordered state as compared to an ordered state. In fact, one paper by Ohkoshi and Kobayashi [100] suggested a similar order-to-order transition but one which relied on spin-reorientation as the mechanism for thermomagnetic generation in 1977. In their work, the thermal dependence of the magnetocrystalline anisotropy constants was used to change the spontaneous magnetization from one crystal axis to another and thus produce a net change of magnetization along one crystal axis. However, a discussion on the relative merits of this approach in the thermomagnetic energy harvesting efficiency was absent in their study.

The results in Table 4-1 also suggest that it is difficult to achieve η_{rel} ~ 55% as predicted in theory [69]. While such findings may seem discouraging, potential solutions are possible. Since both single crystals and order-to-order transitions show relatively higher η_{rel}, it is inferred that the thermomagnetic energy harvesting efficiency can be improved by eliminating "randomness". Here, the randomness is defined by either structural or magnetic disorder in ferromagnetic materials. Consider an example of a single domain, where all the spins are aligned in one direction (i.e. a well ordered magnetic state). Fig. 4-8 shows the illustration of an isothermal magnetization curve representative of single domain Gd as well as actual magnetization curves of polycryalline Gd measured at 283 and 288 K with SQUID. From a

macroscopic view, the single domain is a completely uniform magnetization state achieved by eliminating domain walls (i.e. eliminating randomness). Therefore, it also has nearly 100% remanence at zero applied field, such that $M_{cold} \rightarrow M_s$ at any field, where M_s is spontaneous or saturation magnetization. The theoretical M_s of Gd at 283 K calculated using Brillouin function is assumed to be the magnetization of single domain Gd at zero applied field, and the magnetization of single domain Gd at 5 kOe is assumed to be the same as polycrystalline Gd. In Fig. 4-8, the W_{out} of single domain Gd is calculated to be 6.92×10^5 erg/cm^3 while in contrast the W_{out} of polycrystalline Gd is 2.42×10^5 erg/cm^3. For this case, η_{rel} = 30.4% is calculated for single domain Gd, which is nearly three times larger than polycrystalline η_{rel} = 10.6%, and begins approaching the values previously calculated from theory.

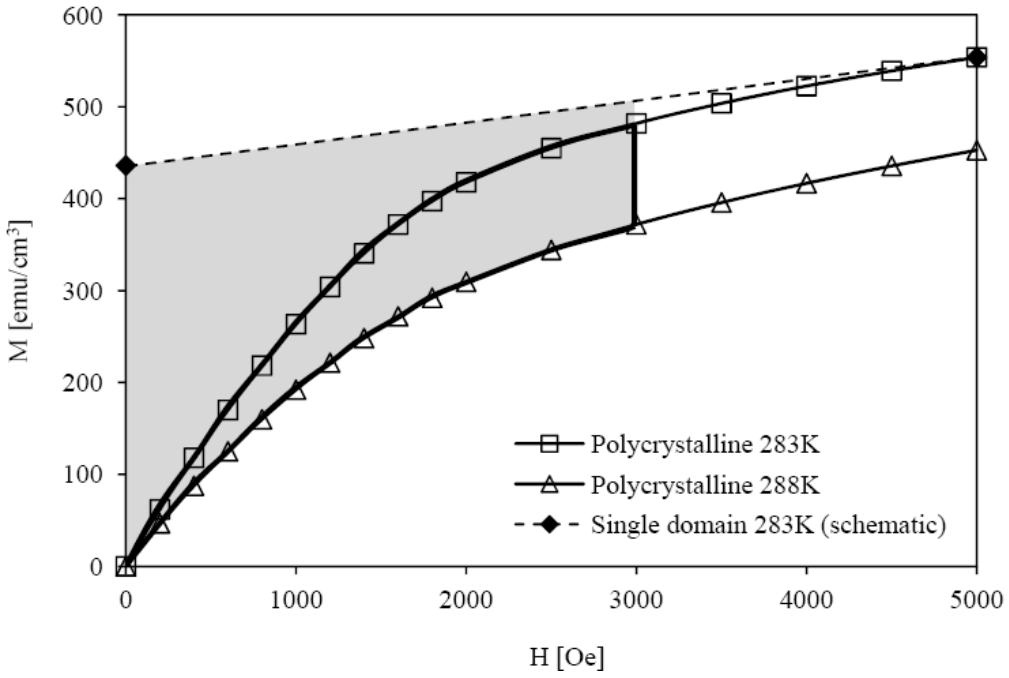

Figure 4-8: Isothermal magnetization curves of polycrystalline and single domain Gd. The gray area represents the W_{out} in a thermomagnetic cycle for a single domain Gd (for T_{cold} = 283 K, ΔT = 5 K, and H_{app} = 3000 Oe). The area bounded by bold curves represents the W_{out} for polycrystalline Gd in the same cycle

4-5 Summary

In this chapter, an efficiency analysis on eight ferromagnetic elements for thermomagnetic energy harvesting using a magnetic field of 3 kOe representative of NdFeB permanent magnets is conducted. Results show that the theoretical maximum efficiency of a thermomagnetic generation is difficult to achieve using conventional approaches associated with ferromagnetic materials. While larger magnetic fields increase η_{rel}, further power consumption is required to generate these larger magnetic fields and this may be an issue. In general, superior efficiencies are observed when a more uniform magnetization state is present, such as single crystals or order-to-order phase transitions, as compared to more random structures such as polycrystalline or order-to-disorder phase transitions. It is further suggested that by eliminating domain walls, the spin configuration can reach a more ordered state, especially at small magnetic field ($H_{app} \sim 0$), while still retaining fairly high magnetization values. This suggests that the η_{rel} of single domains produce substantially higher efficiencies as compared to multi-domain structures.

CHAPTER 5

CONCLUSION AND OUTLOOK

In this work, physics underlying and issues associated with magnetic anisotropy change in ferromagnetic materials at nanoscale were studied with both experimental and analytical methods. Discussions have focused on magnetic anisotropy change of 3d transition (Ni) and 4f rare earth (Gd) elements which were fabricated into nanostructures. A potential application in thermomagnetic energy harvesting using a magnetic anisotropy engineered (i.e. single domain) ferromagnetic element has also been proposed. Important results and findings are summarized in the following.

In the first half of Chapter 2, experimental results of significant out-of-plane magnetization changes represented by an elimination of stripe domain pattern in a 60-nm-thick thin film Ni/PMN-PT (001) heterostructure is shown. The stripe domain elimination process is electrically controllable and reversible when remnant strain is absent. The observed domain structure change is attributed to the transition from Bloch wall to Néel wall and the broadening of the Bloch wall resulted from the negative magnetostriction of Ni thin film. An in-plane "easy" axis and "crack-like" domain structures emerge when the remnant strain exists. The crack-like domain structure represented by a local out-of-plane stray field is attributed to Bloch walls pinned by ferroelectric domain texturing. Similar electrically controlled stripe domain pattern change cannot be found in 100-nm-thick Ni thin films, i.e. this process is thickness dependent. In the second half of Chapter 2, the Kittel's theory is introduced to calculate the critical dimension of Ni single domain. A good match between analytical model and MFM experimental data is

shown. Results of both thin films and nanostructures show the feasibility of engineering magnetic anisotropy to control magnetic properties at nanoscale.

Chapter 3 evaluates the magnetic response of 25-nm-thick Gd thin film and 1400×70×50 nm^3 Gd nanobar structures. Neither the thin film nor the nanobars exhibited single domain behavior at temperatures down to 53 K. The Gd thin film exhibited a magnetocrystalline anisotropy induced spin-reorientation due to a hexagonal close-packed (002) texture, something different from that previously reported on epitaxial Gd thin film. The discrepancy is due to grain boundary induced spin-disorder in the nanosacle. The Gd nanobars had a saturation magnetization 75% smaller than the thin film or bulk and is attributed to oxidation as well as the crystallographic changes from hexagonal close-packed to face-centered cubic caused by stress induced stacking faults. These experimental results for both thin film and nanobar show that the crystallinity has a substantial impact to the magnetic anisotropy of Gd nanostructures as well as the formation of single domain structures.

In Chapter 4, an application of engineering magnetic anisotropy which improves the efficiency of thermomagnetic generation is introduced. The theory of thermomagnetic generation is reviewed and an efficiency analysis using experimentally measured magneto-thermal properties of 3d transition and 4f rare earth ferromagnetic elements is presented. While theoretical results suggest that 55% of Carnot efficiency is possible, experimental data indicates values smaller than 25% of Carnot efficiency unless large magnetic field (e.g. H_{app} ~ 80 kOe) is applied. For smaller magnetic fields representative of NdFeB permanent magnets (e.g. H_{app} = 3 kOe), the largest efficiencies are obtained for operating ferromagnetic materials over a smaller temperature difference (ΔT = 5 K). Furthermore, single crystal materials are found to have superior efficiencies as do elements that undergo an order-to-order phase transition. Both of

these later results relate to increased magnetization changes over a given ΔT. These results are subsequently used to postulate that a single domain structure will produce larger efficiencies due to the higher magnetization present over a wide range of magnetic fields when compared to multi-domain materials. Calculations for a Gd single domain suggest efficiencies on the order of 30% are possible representing a threefold increase from multi-domain Gd at relatively small magnetic fields.

In general, this work reports promising results of engineering magnetic anisotropy at nanoscale, which is not only of scientific interests but also for the sake of practical applications. One of the future works for multiferroic Ni/PMN-PT heterostructures could be a direct observation of the coupling effect between ferroelectric and ferromagnetic domains. The explanations based on the MFM observations are more speculative because there is still a lack of information regarding the domain structure within the thin film along its thickness direction. A Lorentz force TEM experiment may help to observe the domain structure change in the thickness direction. In addition, a 60-nm-thick Ni nanobar structure is maybe of interests for magnetic anisotropy control since the magnetostriction of Ni nanostructures at this thickness may provide a route for the electrical control of single domain formation.

The fabrication of single domain Gd nanostructure is still challenging not only due to the reactive nature of Gd but also because of potential crystal structure transformation at nanoscale. To avoid oxidation and its associated problems in a lift-off process of Gd nanobar fabrication, a sputtering process may be an alternative way (to replace E-beam evaporation) to deposit Gd. Due to the fact that Gd is “unstable” at nanoscale, Gd nanostructures may not be a good candidate for single domain application in thermomagnetic generation. For the sake of using single domain ferromagnetic materials to robustly harvest thermal energy in the room temperature range, one

approach is maybe using a ferromagnetic compound (i.e. Y_2Fe_{17}) which also has a Curie point in the neighborhood of room temperature. However, a fabrication process of a nanostructured single domain compound still needs further investigation and development. On the other hand, the application of spin-reorientation currently receives only little attention in the field of thermal energy harvesting. Since the spin-reorientation represents an easy direction rotation of 90 degree between two orthogonal axes in a well-defined magnetic ordered state, it may infer a thermomagnetic energy conversion with high efficiency worth further studies.

Appendix A

MATLAB CODE FOR MODELING CRITICAL DIMENSIONS

```
%% Calculate the critical dimension of single domain prism in a wide range
based on the Kittel's theory
%% Rule: a>b>c (length>width>thickness)

%% Main program
clear all
close all
clc

c = 35; % Enter a thickness [nm]
a = c+2:1:1000; % length range [nm]
SigmaW = 0.9; % Ni domain wall energy
Ms = 485; % saturation magnetization of Ni

for i = 1:length(a)
    b = c+1:2:a(i)-1; % width range
    for j = 1:length(b)
        for k = 1:length(c)
            b_a(j,i,k) = b(j)/a(i); % b/a
            c_a(j,i,k) = c(k)/a(i); % c/a

            % demag factor from Aharoni's paper %
            N(j,i,k) = demag_factor_Aharoni(a(i),b(j),c(k));

            % critical width from Kittel %
            Wc(j,i,k) = (2*SigmaW/(4*pi*N(j,i,k)*Ms^2))*10^7;

            Lc(j,i,k) = Wc(j,i,k)/b_a(j,i,k); % calculate Lc with b/a
            Tc(j,i,k) = Lc(j,i,k)*c_a(j,i,k); % calculate Tc with c/a

            Wcb(j,i,k) = Wc(j,i,k); % record all original Wc data in Wcb
            Lcb(j,i,k) = Lc(j,i,k); % record all original Lc data in Lcb
            Tcb(j,i,k) = Tc(j,i,k); % record all original Tc data in Tcb

            if (Wcb(j,i,k)<b(j))
                Wcb(j,i,k) = 0; % find Wc boundary of single domain
            end

            if (Lcb(j,i,k)<a(i))
                Lcb(j,i,k) = 0; % find Lc boundary of single domain
            end

            if (Tc(j,i,k)<c(k))
                Tcb(j,i,k) = 0;
                Wcb(j,i,k) = 0;
                Lcb(j,i,k) = 0;
```

```
            end
        end
    end
end

% Plot Wc boundary as a function of length and width %
% Better to use X-Y view %
mesh(a,b,Tc(:,:,1));
xlabel ('Length [nm]'); ylabel ('Width [nm]'); zlabel ('Tc [nm]');


%% Subroutine (programmed by Alex Bur)

function [Nm] = demag_factor_Aharoni(a,b,c)

a1=a;
%b1=b;
c1=c;

a=c1;
c=a1;

% Nm is calculated in SI unit -> N1 + N2 + N3 = 4pi %
% To calculate Nm in CGS, just multiply the calculated value by 4pi %

term1 = (b*b - c*c)/(2*b*c) * log((sqrt(a*a + b*b + c*c) - a)/(sqrt(a*a + b*b
+ c*c) + a));

term2 = (a*a - c*c)/(2*a*c) * log((sqrt(a*a + b*b + c*c) - b)/(sqrt(a*a + b*b
+ c*c) + b));

term3 = b/(2*c) * log((sqrt(a*a + b*b) + a)/(sqrt(a*a + b*b) - a));

term4 = a/(2*c) * log((sqrt(a*a + b*b) + b)/(sqrt(a*a + b*b) - b));

term5 = c/(2*a) * log((sqrt(b*b + c*c) - b)/(sqrt(b*b + c*c) + b));

term6 = c/(2*b) * log((sqrt(a*a + c*c) - a)/(sqrt(a*a + c*c) + a));

term7 = 2*atan(a*b/(c*sqrt(a*a + b*b + c*c)));

term8 = (a*a*a + b*b*b - 2*c*c*c)/(3*a*b*c);

term9 = (a*a + b*b - 2*c*c)/(3*a*b*c)* sqrt(a*a + b*b + c*c);

term10= c/(a*b)*(sqrt(a*a + c*c) + sqrt(b*b + c*c));

term11= ((a*a + b*b)^(3/2) + (b*b + c*c)^(3/2) + (c*c + a*a)^(3/2)) /
(3*a*b*c);

% Calculate the final value %
Nm = (term1 + term2 + term3 + term4 + term5 + term6 + term7 + term8 + term9 +
term10 - term11)/pi;
```

Appendix B

NANOSTRUCTURE FABRICATION USING FOCUSED ION BEAM MILLING

The Nova 600 dual-beam SEM/FIB system was used as a test bed for the fabrication of Gd nanostructures. In the fabrication process shown in Fig. 2-15, a resist layer has to be deposited prior to the E-beam evaporation of thin film, so that the resist works as a sacrificial layer to be removed in the lift-off process to fabricate nanostructures. In the FIB milling process, since the focused Ga ion beam is able to mill out materials at very specific locations decided by users, the FIB milling makes it possible to fabricate nanostructures directly out of a thin film without using a resist layer. Fig. B-1 illustrates a FIB milling process of Gd nanostructures on a Si substrate. Prior to the milling, a 25-nm-thick Gd thin film and a 20-nm-thick Pt capping layer were deposited onto the surface of Si substrate. In Fig B-1, Ga ions are focused to mill the sample surface at specific regions, and therefore, the un-milled regions become the final structures fabricated.

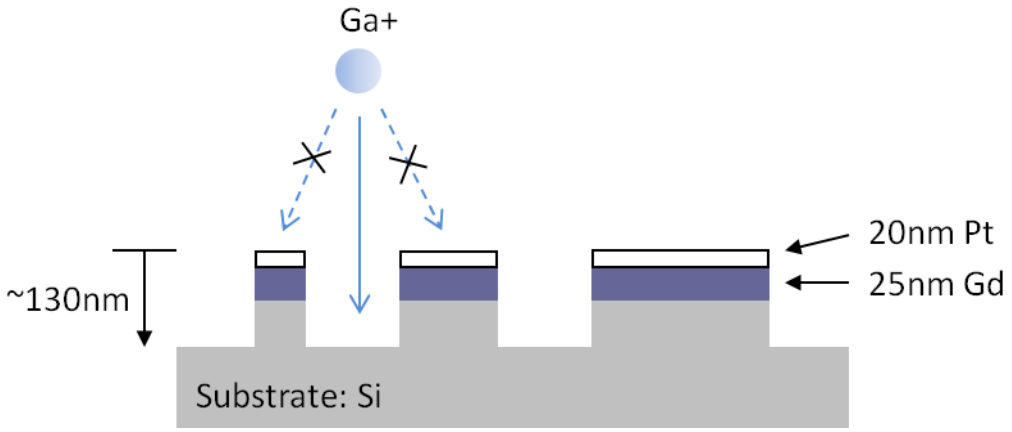

Figure B-1: Cross-sectional illustration of Gd nanostructures fabrication using the FIB milling process.

Fig. B-2a shows a pattern of nanostructures with five different geometries, and this pattern is used in an actual FIB milling process. In Fig. B-2a, the rectangles with a gray color represent the regions which are not milled with FIB (i.e. the nanostructures fabricated). After a couple of trial and error tests for finding the ideal processing parameters (e.g. current), the final structures fabricated were captured with SEM and is shown in Fig. B-2b. The actual dimensions of nanostructures are marked in the SEM image. Fig. B-2b shows that the FIB milling process has a good dimension control at submicron range.

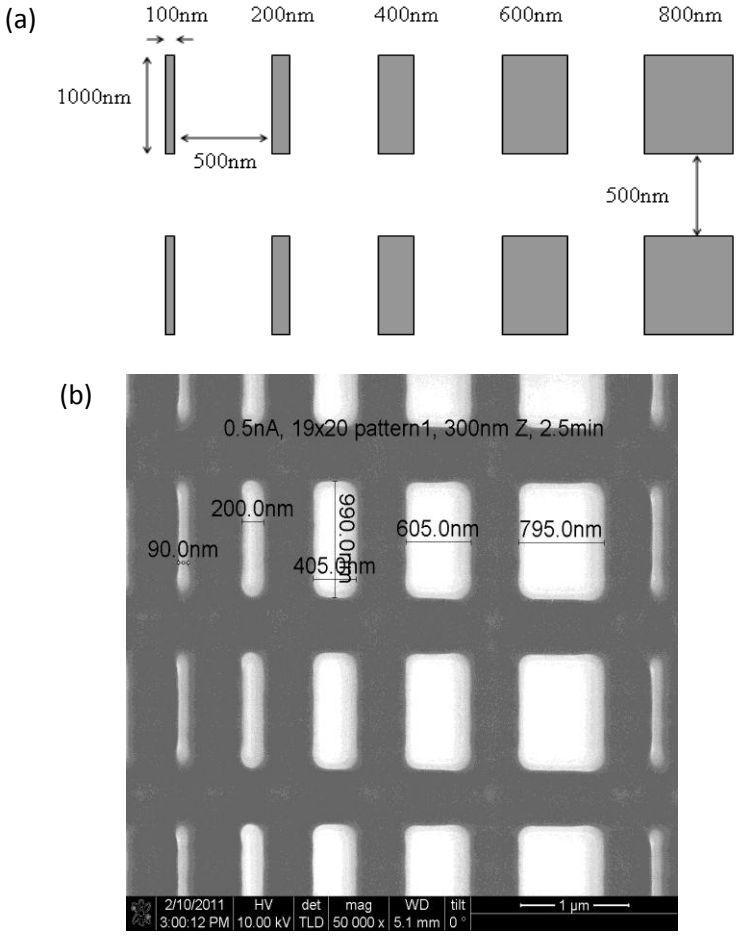

Figure B-2: (a) Pattern of nanostructures with five different geometries, and (b) SEM image of the actual pattern of Gd nanostructures fabricated using FIB.

The Gd nanostructures shown in Fig. B-2 are further analyzed in a AFM (Bruker Dimension Icon) using tapping mode (see Fig. B-3). As shown in Fig. B-3a and Fig. B-3b, three nanostructures with smaller dimensions shown in the SEM images are scanned and captured as an AFM image, and therefore, a complete topographic profile of the FIB fabricated nanostructures is obtained. By analyzing the AFM data, the sectional height information is shown in Fig. B-3c. Fig. B-3c shows that the three nanostructures have different heights (i.e. structure thickness), and from left to right, the structure thicknesses are 84.378, 112.038, and 133.691 nm respectively. Due to the fact that the FIB scans over the sample surface during milling, the thickness difference in Fig. B-3c is basically an indication of material loss on top of the smaller nanostructures. Assume that there is zero material loss on the widest nanostructure in Fig. B-3c, the thickness reduction on the narrowest nanostructure in Fig. B-3c is 133.691 - 84.379 = 49.313 nm. Since the total thickness of the Gd and Pt layers deposited is 45 nm (< 49.313 nm), it is speculated that all the deposited materials on the narrowest nanostructure are lost.

The speculative material loss is verified using the X-ray mapping analysis in an FEI Nova 230 SEM. Fig. B-4 shows the SEM image along with the corresponding mapping image of Gd element. The SEM image in Fig. B-4a shows again that the nanostructures has been fabricated with FIB as the design pattern shown in Fig. B-2a; however, the X-ray mapping image in Fig. B-4b reveals that not all Gd remained on top of the nanostructure surfaces. The yellow circle in Fig. B-4 points out that Gd element cannot be detected at the locations of the narrowest nanostructures (with a width of 90 nm as shown in Fig. B-2b). This result corresponds to the data shown in Fig. B-3c where the narrowest nanostructures have a reduced height of more than 45 nm, i.e. a total loss of Gd (and Pt).

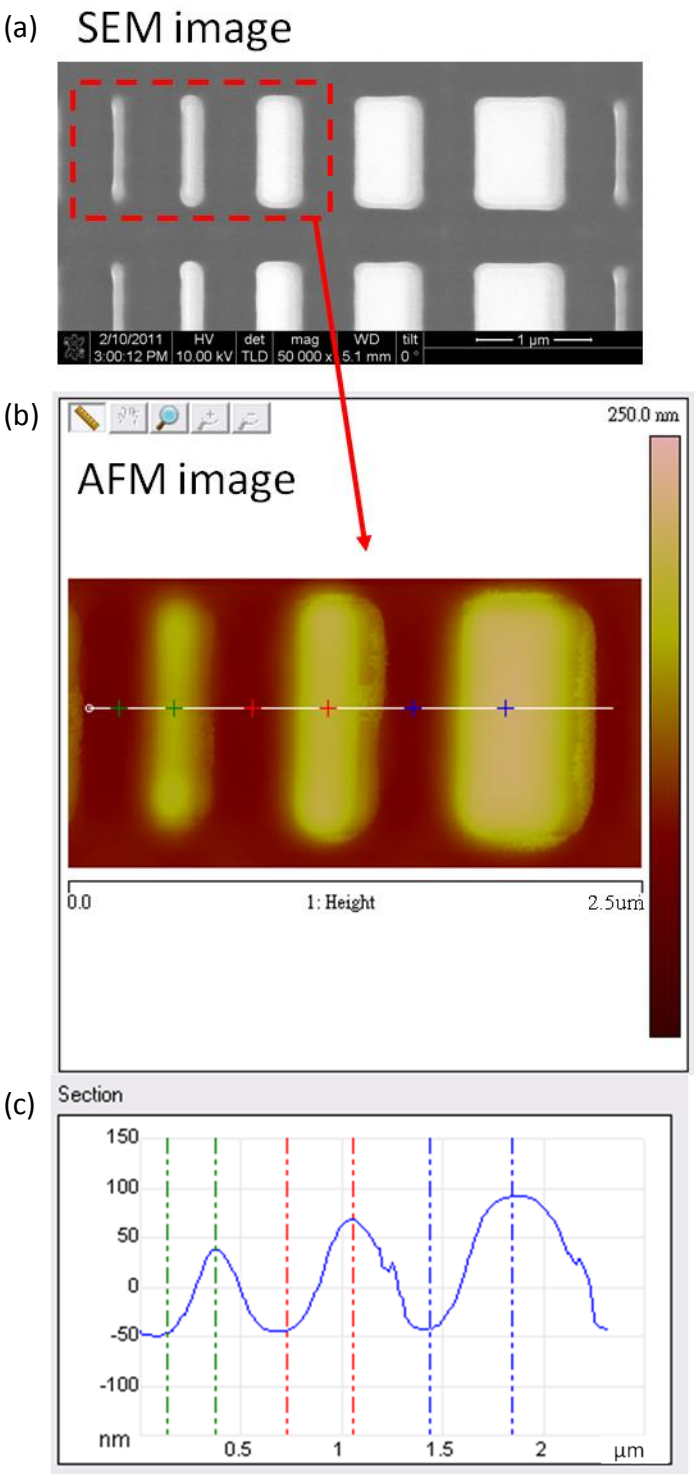

Figure B-3: (a) SEM image of FIB milled Gd nanostructures, (b) AFM image of the FIB milled Gd nanostructures shown in the red dash box in (a), and (c) Sectional topographic profile of the FIB milled Gd nanostructures shown in (b). The positions of green, red, and blue dash lines shown in (c) correspond to the position of the cross marks shown in (b) with the same color.

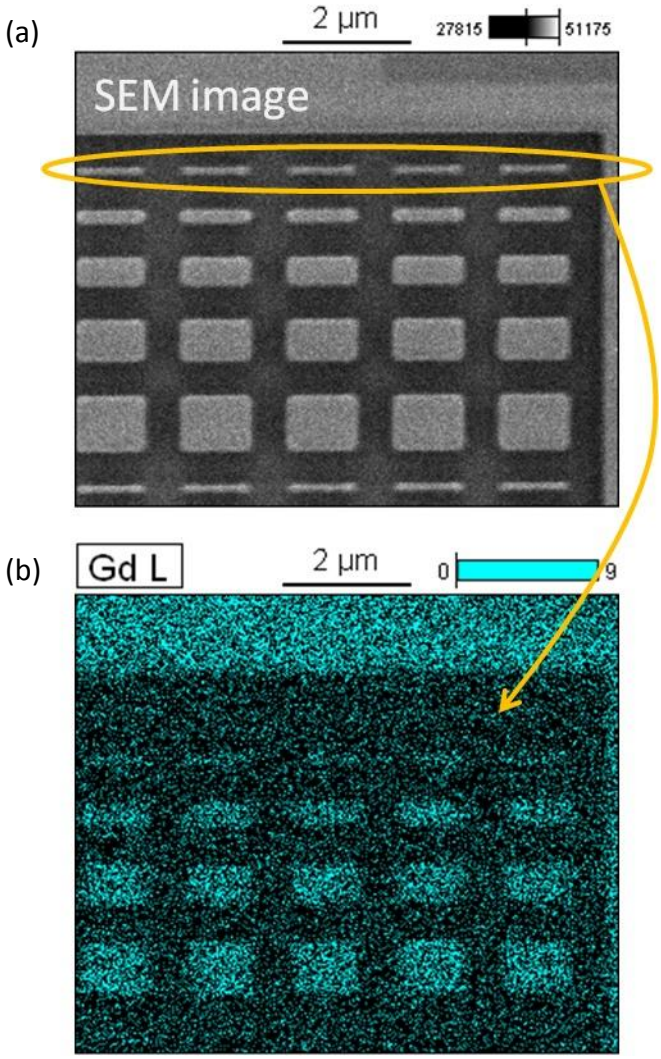

Figure B-4: (a) SEM image of FIB milled Gd nanostructures, and (b) X-ray mapping image of Gd elements.

References

[1] S. N. Piramanayagam, "Perpendicular recording media for hard disk drives," *Journal of Applied Physics,* vol. 102, pp. 011301-22, 2007.

[2] G. Bochi, *et al.*, "Evidence for strong surface magnetoelastic anisotropy in epitaxial Cu/Ni/Cu(001) sandwiches," *Physical Review B,* vol. 53, pp. R1729-R1732, 1996.

[3] H. J. Hug, *et al.*, "Magnetic domain structure in ultrathin Cu/Ni/Cu/Si(001) films (invited)," *Journal of Applied Physics,* vol. 79, pp. 5609-5614, 1996.

[4] S. Hameed, *et al.*, "Analysis of disordered stripe magnetic domains in strained epitaxial Ni(001) films," *Physical Review B,* vol. 64, p. 184406, 2001.

[5] M. A. Marioni, *et al.*, "Remanence due to wall magnetization and counterintuitive magnetometry data in 200-nm films of Ni," *Physical Review Letters,* vol. 97, p. 027201, 2006.

[6] T.-K. Chung, *et al.*, "Reversible magnetic domain-wall motion under an electric field in a magnetoelectric thin film," *Applied Physics Letters,* vol. 92, pp. 112509-3, 2008.

[7] M. Fiebig, "Revival of the magnetoelectric effect," *Journal of Physics D: Applied Physics,* vol. 38, 2005.

[8] W. Eerenstein, *et al.*, "Multiferroic and magnetoelectric materials," *Nature,* vol. 442, pp. 759-765, 2006.

[9] C.-W. Nan, *et al.*, "Multiferroic magnetoelectric composites: Historical perspective, status, and future directions," *Journal of Applied Physics,* vol. 103, pp. 031101-35, 2008.

[10] J. Ma, *et al.*, "Recent progress in multiferroic magnetoelectric composites: from bulk to thin films," *Advanced Materials,* vol. 23, pp. 1062-1087, 2011.

[11] T. Wu, *et al.*, "Electrical and mechanical manipulation of ferromagnetic properties in polycrystalline nickel thin film," *Magnetics Letters, IEEE,* vol. 2, p. 6000104, 2011.

[12] T. Wu, *et al.*, "Electric-poling-induced magnetic anisotropy and electric-field-induced magnetization reorientation in magnetoelectric Ni/(011) $[Pb(Mn_{1/3}Nb_{2/3})O_3]_{(1-x)}$-$[PbTiO_3]_x$ heterostructure," *Journal of Applied Physics,* vol. 109, pp. 07D732-3, 2011.

[13] S. Geprags, *et al.*, "Electric field controlled manipulation of the magnetization in Ni/$BaTiO_3$ hybrid structures," *Applied Physics Letters,* vol. 96, pp. 142509-3, 2010.

[14] A. Brandlmaier, *et al.*, "Nonvolatile, reversible electric-field controlled switching of remanent magnetization in multifunctional ferromagnetic/ferroelectric hybrids," *Journal of Applied Physics,* vol. 110, pp. 043913-5, 2011.

[15] T. H. E. Lahtinen, *et al.*, "Pattern transfer and electric-field-induced magnetic domain formation in multiferroic heterostructures," *Advanced Materials,* vol. 23, pp. 3187-3191, 2011.

[16] J. J. Yang, *et al.*, "Electric field manipulation of magnetization at room temperature in multiferroic $CoFe_2O_4$/$Pb(Mg_{1/3}Nb_{2/3})_{0.7}Ti_{0.3}O_3$ heterostructures," *Applied Physics Letters,* vol. 94, pp. 212504-3, 2009.

[17] S. Sahoo, *et al.*, "Ferroelectric control of magnetism in $BaTiO_3$/Fe heterostructures via interface strain coupling," *Physical Review B,* vol. 76, p. 092108, 2007.

[18] M. Liu, *et al.*, "Giant electric field tuning of magnetic properties in multiferroic ferrite/ferroelectric heterostructures," *Advanced Functional Materials,* vol. 19, pp. 1826-1831, 2009.

[19] J. Lou, *et al.*, "Giant electric field tuning of magnetism in novel multiferroic FeGaB/Lead zinc niobate–lead titanate (PZN-PT) heterostructures," *Advanced Materials,* vol. 21, pp. 4711-4715, 2009.
[20] B. Zhang, *et al.*, "Electric-field effect on magnetic properties of FePt/PZN-PT heterostructures," *Magnetics, IEEE Transactions on,* vol. 47, pp. 4402-4404, 2011.
[21] C. Thiele, *et al.*, "Influence of strain on the magnetization and magnetoelectric effect in $La_{0.7}A_{0.3}MnO_3$/PMN-PT(001) (A=Sr,Ca)," *Physical Review B,* vol. 75, p. 054408, 2007.
[22] J.-M. Hu and C. W. Nan, "Electric-field-induced magnetic easy-axis reorientation in ferromagnetic/ferroelectric layered heterostructures," *Physical Review B,* vol. 80, p. 224416, 2009.
[23] N. A. Pertsev, "Giant magnetoelectric effect via strain-induced spin reorientation transitions in ferromagnetic films," *Physical Review B,* vol. 78, p. 212102, 2008.
[24] T. Wu, *et al.*, "Electrical tuning of metastable dielectric constant of ferroelectric single crystals for low-power electronics," *Applied Physics Letters,* vol. 99, pp. 182903-3, 2011.
[25] R. C. O'Handley, *Modern magnetic materials: principles and applications*. New York: John Wiley & Sons., 2000.
[26] B. D. Cullity and C. D. Graham, *Introduction to Magnetic Materials*, 2nd ed.: Wiley-IEEE Press, 2008.
[27] J. J. Martin, *et al.*, "Ordered magnetic nanostructures: fabrication and properties," *Journal of Magnetism and Magnetic Materials,* vol. 256, pp. 449-501, 2003.
[28] S. Y. Chou, "Patterned magnetic nanostructures and quantized magnetic disks," *Proceedings of the IEEE,* vol. 85, pp. 652-671, 1997.
[29] S. Evoy, *et al.*, "Thickness dependent binary behavior of elongated single-domain cobalt nanostructures," *Journal of Applied Physics,* vol. 87, pp. 404-409, 2000.
[30] J. F. Smyth, *et al.*, "Hysteresis in lithographic arrays of permalloy particles: Experiment and theory (invited)," *Journal of Applied Physics,* vol. 69, pp. 5262-5266, 1991.
[31] C. Kittel, "Theory of the structure of ferromagnetic domains in films and small particles," *Physical Review,* vol. 70, pp. 965-971, 1946.
[32] A. Aharoni, "Demagnetizing factors for rectangular ferromagnetic prisms," *Journal of Applied Physics,* vol. 83, pp. 3432-3434, 1998.
[33] J. A. Osborn, "Demagnetizing factors of the general ellipsoid," *Physical Review,* vol. 67, pp. 351-357, 1945.
[34] A. M. Tishin and Y. I. Spichkin, *The magnetocaloric effect and its applications*: Institute of Physics Publishing, 2003.
[35] J. F. Elliott, "Thermomagnetic generator," *Journal of Applied Physics,* vol. 30, pp. 1774-1777, 1959.
[36] D. Solomon, "Design of a thermomagnetic generator," *Energy Conversion and Management,* vol. 31, pp. 157-173, 1991.
[37] G. W. Roderback, "Thermomagnetic generator," *United States Atomic Energy Commission Report,* vol. NAA-SR-264, 1953.
[38] P. Chizhov, A. N. Kostigov, and V. I. Petinov, "Structure and magnetic properties of rare earth small particles," *Solid State Communications,* vol. 42, pp. 323-326, 1982.
[39] S. Y. Dan'kov, *et al.*, "Magnetic phase transitions and the magnetothermal properties of gadolinium," *Physical Review B,* vol. 57, pp. 3478-3490, 1998.
[40] M. Ujihara, *et al.*, "Thermal energy harvesting device using ferromagnetic materials," *Applied Physics Letters,* vol. 91, p. 093508, 2007.

[41] K. E. Bulgrin, *et al.*, "A coupled thermal and mechanical model of a thermal energy harvesting device," presented at the ASME 2009 International Mechanical Engineering Congress & Exposition, Lake Buena Vista, Florida, USA, 2009.
[42] U. Paschen, *et al.*, "Magnetic properties of thin epitaxial Gd films on Nb," *Zeitschrift für Physik B Condensed Matter,* vol. 90, pp. 289-296, 1993.
[43] A. Berger, *et al.*, "Magnetic reorientation transition of Gd(0001)/W(110) films," *Physical Review B,* vol. 52, p. 1078, 1995.
[44] A. Berger, *et al.*, "Magnetic reorientation transition in epitaxial Gd-films," *Journal of Magnetism and Magnetic Materials,* vol. 137, pp. L1-L5, 1994.
[45] U. Stetter, *et al.*, "Critical behavior of strained epitaxial Gd films: In situ ac-susceptibility measurements in UHV," *Physical Review B,* vol. 45, p. 503, 1992.
[46] J. S. Jiang and C. L. Chien, "Magnetization and finite size effects in Gd/W multilayers," *Journal of Applied Physics,* vol. 79, pp. 5615-5617, 1996.
[47] A. Heys and P. E. Donovan, "Magnetisation measurements on gadolinium/tungsten multilayers," *Journal of Magnetism and Magnetic Materials,* vol. 126, pp. 326-328, 1993.
[48] D. Michels, *et al.*, "Grain-size-dependent Curie transition in nanocrystalline Gd: the influence of interface stress," *Journal of Magnetism and Magnetic Materials,* vol. 250, pp. 203-211, 2002.
[49] M. Yue, *et al.*, "Preparation, microstructure, and magnetic properties of bulk nanocrystalline Gd metal," *Applied Physics Letters,* vol. 89, p. 232504, 2006.
[50] F. Döbrich, *et al.*, "Grain-boundary-induced spin disorder in nanocrystalline gadolinium," *Journal of Physics: Condensed Matter,* vol. 21, p. 156003, 2009.
[51] I. Aruna, *et al.*, "Stability and hydrogenation of "bare" gadolinium nanoparticles," *Advanced Functional Materials,* vol. 15, pp. 131-137, 2005.
[52] X. G. Liu, *et al.*, "Microstructure and magnetic properties of graphite-coated Gd nanocapsules," *Applied Physics Letters,* vol. 94, p. 103104, 2009.
[53] N. Lu, *et al.*, "Microstructure and fundamental properties of nanostructured gadolinium (Gd)," *Materials Letters,* vol. 63, pp. 1089-1092, 2009.
[54] O. Singh and A. Curzon, "On the structure and magnetic properties of rare-earth small particles," *Solid State Communications,* vol. 44, pp. 1121-1122, 1982.
[55] R. Thompson, M. Eizenberg, and K. N. Tu, "Schottky contacts of Gd-Pt and Gd-V alloys on n-Si and p-Si," *Journal of Applied Physics,* vol. 52, pp. 6763-6768, 1981.
[56] A. Arrott, "Criterion for ferromagnetism from observations of magnetic isotherms," *Physical Review,* vol. 108, p. 1394, 1957.
[57] O. Nakamura, *et al.*, "Annealing temperature dependence of T_c of thin-film Gd grown on glass substrate," *Journal of Applied Physics,* vol. 64, 1988.
[58] A. Nissim, *et al.*, "Effect of substrate bias voltage on the properties of magnetron-sputtered gadolinium layers," *Surface and Coatings Technology,* vol. 201, 2007.
[59] C. D. Graham, "Magnetocrystalline anisotropy of gadolinium," *Journal of the Physical Society of Japan,* vol. 17, 1962.
[60] W. D. Corner, *et al.*, "The magnetocrystalline anisotropy of gadolinium," *Proceedings of the Physical Society,* vol. 80, p. 927, 1962.
[61] S. Chikazumi, *Physics of Ferromagnetism*: Oxford, 1997.
[62] F. Milstein and L. B. Robinson, "Direction of easy magnetization in gadolinium," *Physical Review,* vol. 177, p. 904, 1969.

[63] K. Tajima, "Magnetocrystalline anisotropy of rare earth impurities doped in gadolinium. I. Heavy rare earth," *Journal of the Physical Society of Japan,* vol. 31, 1971.
[64] Y. I. Spichkin, *et al.*, "Elastic properties of a high purity gadolinium single crystal," *Journal of Magnetism and Magnetic Materials,* vol. 204, pp. 5-10, 1999.
[65] B. M. S. Bist and O. N. Srivastava, "A new fcc gadolinium phase ans its oxidation," *Journal of Less-Common Metals,* vol. 33, 1973.
[66] R. K. Gupta and T. R. Anantharaman, "An X-ray diffraction study of deformation in h.c.p. rare-earth metals," *Journal of the Less-Common Metals,* vol. 25, 1971.
[67] E. Shalaan, *et al.*, "In-situ X-ray diffraction studies of hydrogenated nanocrystalline gadolinium films," *Journal of Materials Science,* vol. 41, pp. 7454-7458, 2006.
[68] D. M. Rowe, *Thermoelectrics handbook: marco to nano*: CRC press, 2006.
[69] L. Brillouin and H. Iskenderian, "Thermomagnetic generator," *Electrical Communication,* vol. 25, pp. 300–311, 1948.
[70] H. Stauss, "Efficiency of thermomagnetic generator," *Journal of Applied Physics,* vol. 30, p. 1622, 1959.
[71] K. Murakami, "The characteristics of ferrite cores with low Curie temperature and their application," *IEEE Transactions on Magnetics,* vol. 1, pp. 96-100, 1965.
[72] R. E. Rosensweig, "Theory of an improved thermomagnetic generator," presented at the Proceeding of IEEEs, 1967.
[73] L. Kirol and J. Mills, "Numerical analysis of thermomagnetic generators," *Journal of Applied Physics,* vol. 56, pp. 824-828, 1984.
[74] D. Solomon, "Improving the performance of a thermomagnetic generator by cycling the magnetic field," *Journal of Applied Physics,* vol. 63, pp. 915-921, 1988.
[75] N. Tesla, "Pyromagneto-electricgenerator," US Patent 428,057, 1890.
[76] T. A. Edison, "Pyromagnetic generator," US Patent 476,983, 1892.
[77] D. Solomon, "Thermomagnetic mechanical heat engines," *Journal of Applied Physics,* vol. 65, 1989.
[78] K. Andreevskii, *et al.*, "Investigation of the thermodynamic and physical characteristics of a thermomagnetic engine with a gadolinium working element," *Technical Physics,* vol. 43, pp. 1115-1118, 1998.
[79] P. W. Egolf, *et al.*, "Magnetic power conversion with machines containing full or porous wheel heat exchangers," *Journal of Magnetism and Magnetic Materials,* vol. 321, 2009.
[80] A. Kitanovski, *et al.*, "Applications of magneitc power production and its assessment," ed: Annual report, Swiss Federal Office of Energy, 2008.
[81] B. Coqblin, *The electronic structure of rare-earth metals and alloys: the magnetic heavy rare-earths*. London: Academic Press, 1977.
[82] S. Gama and M. E. Fóglio, "Magnetization of erbium in the ordered and paramagnetic phases," *Physical Review B,* vol. 37, pp. 2123-2132, 1988.
[83] R. W. Green, *et al.*, "Magnetization and electrical resistivity of erbium single crystals," *Physical Review,* vol. 122, p. 827, 1961.
[84] J. F. Elliott, *et al.*, "Magnetic properties of erbium metal," *Physical Review,* vol. 100, p. 1595, 1955.
[85] H. P. Myers and W. Sucksmith, "The spontaneous magnetization of cobalt," *Proceedings of the Royal Society A,* vol. 207, pp. 427-446, 1951.
[86] W. Bendick and W. Pepperhoff, "Thermally excited states in cobalt and cobalt alloys," *Journal of Physics F: Metal Physics,* vol. 9, pp. 2185-2194, 1979.

[87] J. Crangle and G. M. Goodman, "The magnetization of pure iron and nickel," *Proceedings of the Royal Society A,* vol. 321, pp. 477-491, 1971.
[88] L. W. Shacklette, "Specific heat and resistivity of iron near its Curie point," *Physical Review B,* vol. 9, p. 3789, 1974.
[89] H. P. J. Wijn, "1.1.2.13 Specific heat, resistivity," in *Group III Condensed Matter*, ed: SpringerMaterials - The Landolt-Börnstein Database
[90] W. C. Thoburn, *et al.*, "Magnetic properties of terbium metal," *Physical Review,* vol. 112, p. 56, 1958.
[91] D. E. Hegland, *et al.*, "Magnetization and electrical resistivity of terbium single crystals," *Physical Review,* vol. 131, p. 158, 1963.
[92] K. D. Jayasuriya, *et al.*, "The critical specific heat of terbium," *Journal of Physics F: Metal Physics,* vol. 14, p. 1725, 1984.
[93] J. F. Elliott, *et al.*, "Some magnetic properties of Dy metal," *Physical Review,* vol. 94, p. 1143, 1954.
[94] K. D. Jayasuriya, *et al.*, "Magnetic transitions in dysprosium: A specific-heat study," *Physical Review B,* vol. 31, p. 6032, 1985.
[95] E. P. Wohlfarth, *Ferromagnetic Materials* vol. 1: North-Holland Publishing, 1980.
[96] B. L. Rhodes, *et al.*, "Magnetic properties of holmium and thulium metals," *Physical Review,* vol. 109, p. 1547, 1958.
[97] D. L. Strandburg, *et al.*, "Electrical and magnetic properties of holmium single crystals," *Physical Review,* vol. 127, p. 2046, 1962.
[98] A. M. Stewart and S. J. Collocott, "The specific heat of samarium and holmium in the range 2-32 K," *Journal of Physics: Condensed Matter,* vol. 1, p. 677, 1989.
[99] R. E. Skochdopole, *et al.*, "Heat capacity of erbium from 15 to 320 K," *The Journal of Chemical Physics,* vol. 23, pp. 2258-2263, 1955.
[100] M. Ohkoshi and H. Kobayashi, "Rotational-type spin reorientation in $Nd_{1-x}Dy_xCo_5$ and its application to thermomagnetic generator," *IEEE Transactions on Magnetics,* vol. MAG-13, pp. 1158-1160, 1977.